Reconciling High-resolution Strain Rate of Continental China from GNSS Data with the Spherical Spline Interpolation

Zhengfeng Zhang[1], Huai Zhang[2], and Yaolin Shi[1]

[1]University of Chinese Academy of Science
[2]University of Chinese Academy of Sciences

December 10, 2023

Abstract

In this work, we propose a new generation of high-resolution strain rate model of present-day continental China from up-to-date GNSS observation data of 3571 stations. To reconcile the sparsely distributed GNSS (Global Navigation Satellite System) velocity data into an integrated vastly regional spherical coordinate frame, a novel interpolation method, namely the spherical spline method, is introduced as well. It can simultaneously calculate the strain rate with an ideal order of continuity while preserving the discontinuity from tectonically active major fault zones or deforming blocks. We take advantage of a set of inspection standards to assess the validity and resolution of our proposed model. The spherical spline method is deliberately examined and justified to fit the GNSS velocity data to illustrate inspection standards. Moreover, we construct a spherical harmony model for the resolution test. By the test criteria, the spherical spline method can reproduce the velocity and strain rate field at substantial order, suggesting that our method has high applicability and resolution in estimating strain rate in active tectonic regions or even global models. Finally, using the spherical spline method, we used measured GNSS velocity data to calculate the strain rate field in continental China. We also analyze the correlation between the seismic mechanism and the strain rate field of earthquakes, exhibiting that our proposed high-resolution strain rate model has great potential in explaining the deformation or evolution models of continental China.

Reconciling High-resolution Strain Rate of Continental China from GNSS Data with the Spherical Spline Interpolation

Zhengfeng Zhang[1], Huai Zhang[1,2,3] and Yaolin Shi[1]

[1]Key Laboratory of Computational Geodynamics of Chinese Academy of Sciences, College of Earth and Planetary Science, University of Chinese Academy of Sciences, Beijing 100049, China.

[2]Southern Marine Science and Engineering Guangdong Laboratory (Zhuhai), Zhuhai 519080, China.

[3]Beijing Yanshan Earth Critical Zone National Research Station, University of Chinese Academy of Sciences, Beijing 101408, China.

Corresponding author: Huai Zhang (hzhang@ucas.ac.cn)

Key Points:

- The multiple-scale spherical spline and detection model based on the latest GNSS data of continental China is proposed
- Revised high-resolution strain rate reveals new deformation features in continental China and local regions
- High-resolution strain rates exhibit excellent correlation with seismic activities and their focal mechanisms along major fault zones

Abstract

In this work, we propose a new generation of high-resolution strain rate model of present-day continental China from up-to-date GNSS observation data of 3571 stations. To reconcile the sparsely distributed GNSS (Global Navigation Satellite System) velocity data into an integrated vastly regional spherical coordinate frame, a novel interpolation method, namely the spherical spline method, is introduced as well. It can simultaneously calculate the strain rate with an ideal order of continuity while preserving the discontinuity from tectonically active major fault zones or deforming blocks. We take advantage of a set of inspection standards to assess the validity and resolution of our proposed model. The spherical spline method is deliberately examined and justified to fit the GNSS velocity data to illustrate inspection standards. Moreover, we construct a spherical harmony model for the resolution test. By the test criteria, the spherical spline method can reproduce the velocity and strain rate field at substantial order, suggesting that our method has high applicability and resolution in estimating strain rate in active tectonic regions or even global models. Finally, using the spherical spline method, we used measured GNSS velocity data to calculate the strain rate field in continental China. We also analyze the correlation between the seismic mechanism and the strain rate field of earthquakes, exhibiting that our proposed high-resolution strain rate model has great potential in explaining the deformation or evolution models of continental China.

Plain Language Summary

Continental China is characterized by Cenozoic active tectonics and intensive earthquakes widely distributed along major fault zones. Therefore, a high-resolution rate model based on the latest GNSS observation is of great importance in explaining such phenomena. This work introduces a novel multiscale spherical spline method that can adapt to discrete data at medium and high latitudes to remove the distortions caused by the conventional method in the Cartesian coordinate system. The rigid-body rotation and spherical harmonic checkerboard detection are utilized to validate the feasibility and resolution of the approach. GNSS data are collected from the most recent studies to estimate the high-resolution strain rate of continental China. Meanwhile, we analyze the correlation between strain rate and focal mechanisms and interpret the deformation and seismicity in continental China.

1 Introduction

Using GNSS velocity data estimating strain rate field has been studied for a long time (Hori et al., 2001; Savage et al., 2001; Shen et al., 2001). Even though the researchers use roughly the same data set, the results are not entirely consistent (Jiang & Liu, 2010; Rui & Stamps, 2019; Wang & Shen, 2020; Wu et al., 2009), which is mainly relative to their method. According to the distinction of using coordinates, estimating strain rate fields using GPS velocity data can be divided into Cartesian and spherical. Delaunay triangulation is always used in the Cartesian coordinate system because Delaunay triangulation in the sphere involves a highly complex algorithm and is time-consuming. This method has the advantage of being less computationally intensive but is error-sensitive and does not guarantee first-order continuity of the strain rate. As a common geostatistical method, Kriging interpolation can also fit strain rates using GNSS data (Zhu & Shi, 2011).

Nevertheless, Kriging interpolation does not consider the overall spatial correlation of the estimated values enough. It also requires high-quality data, and GNSS data are susceptible to various environmental factors and cannot meet the requirements. Numerous Cartesian coordinate methods always adopt the first-order Taylor series of the velocity field (Okazaki et al., 2021; Savage et al., 2001), then construct and solve the equations system to obtain strain rate. However, this practice is equivalent to linear interpolation, which decreases detail when GNSS stations are spares. Therefore, this method suits station-dense areas and large-scale surface deformation analysis. Some Cartesian coordinate methods can accurately fit the velocity values (Xiong et al., 2021), but because GNSS velocity data have large errors, over-fitting may cause distortions in the estimation results. Least-squares collocation and multi-surface function can be implemented in the Cartesian and spherical coordinate systems (Rui & Stamps, 2019; Shen et al., 2015; Wang & Shen, 2020; Wu et al., 2009). These two methods also do not guarantee the first-order smoothness of the strain rate. The higher-order continuity of the strain rate is critical for the equation of strain compatibility in the continuum mechanics, limiting the application of these methods. The Spherical wavelet and spherical harmonics are pure spherical coordinate algorithms. Moreover, spherical wavelet and spherical harmonics as pure spherical coordinate methods are like trigonometric functions, which might smooth out much detail of strain rate when GPS or GNSS stations are dense (Su et al., 2016; Wu et al., 2009). These methods will not be able to help analyze small-scale deformation and seismic mechanisms.

Continental China is a geologically active region with frequent earthquakes. Many researchers use GNSS velocity data and strain rate to study its continued deformation, active tectonics, and seismic activity. The Qinghai-Tibet Plateau region is one of the most tectonically active regions in the world, and its continuous deformation and its tectonic implications have always been of concern (Chen et al., 2004; Devachandra et al., 2014; Gan et al., 2007; Liang et al., 2013; Wang et al., 2017; Zhang et al., 2004). Due to the Qinghai-Tibetan plateau's implication, its surroundings are seismically active. Shen et al. (2009) and Qi et al. (2011) used GPS velocity data from the Longmen Mountain area to study active tectonics and seismic hazards in this area. Zhao et al. (2018) studied the tectonic influence and seismic mechanism of the 2017 Jiuzhaigou earthquake. (Shen et al., 2001) analyzed the deformation characteristic of the fault system in the western Tibetan Plateau. (Qu et al., 2018) studied the creeping nature of the crust in the Weihe Basin. In addition to the local region, the continuous deformation and seismicity of the Chinese mainland as a whole are also hot spots for researchers (Liu et al., 2007; Rui & Stamps, 2019; Wang et al., 2011; Wang & Shen, 2020; Wei et al., 2014; Xiong et al., 2021; Yu et al., 2019; Zheng et al., 2017). The continental China region straddles the mid and low latitudes. It is in a particular area of the Asia-European plate where active tectonics and seismic hazards are widely distributed. The compression of the Indian plate located at low latitudes also dramatically impacts the mid-latitude and eastern region of continental China. Therefore, it is necessary to develop a high spatial resolution and latitude-adaptation method to further study continental China’s strain rate field, seismic activity, and seismic mechanism. The multi-scale spherical spline method can automatically adapt to the inhomogeneous characteristics of the station distribution. Furthermore, it can ensure the smoothness of the strain rate as well as the discontinuous strain rate near the significant active tectonics. At the same time, the spherical spline method can ensure the second-order continuity of the velocity field, which can provide continuous boundary conditions for numerical simulations such as finite elements.

Solving an ill-posed equation is necessary to obtain the velocity or strain rate in the meshed grid regardless of the method used. Because of this problem's ill-posed nature, it can have multiple solutions or no solution. Using a smoothing tool can obtain a relatively reasonable solution but also introduces errors (Gan et al., 2007; Ge et al., 2013; Shen et al., 1996; Tape et al., 2009; Wu et al., 2011). Assessing effectiveness and resolution is always a significant issue for solving inverse problems. Scholars studying geophysical inverse problems realized the importance of method uncertainty and resolution in determining the solution (Backus, 1967, 1968, 1970; Franklin, 1970; Wiggins, 1972). Calculating strain rate using GPS or GNSS velocity is a typical ill-posed problem.

Many researchers currently use synthetic models to test their methods, but these models all have drawbacks. Some synthetic models can only be adapted to the distribution of stations in a specific study area and tectonic structures (Tape et al., 2009). Other methods are to fit a particular function and judge the merit of the method by the goodness of fit (Tape et al., 2009; Wu et al., 2011). However, the general function shows different values in the specific range, so these tests do not give a resolution of the different areas of the method, and the degree of fit is not easy to observe directly. Many scholars use statistical techniques to determine the accumulation of errors due to smoothings, such as calculating the variance or standard deviation (Jiang et al., 2014; Masson et al., 2014; Tape et al., 2009; Wu et al., 2009; Zhu & Shi, 2011). Nevertheless, the statistical parameters can only represent the overall error situation and do not provide good error discrimination for local areas. Therefore, building a universal set of standards to judge the uncertainty of calculating strain rate by using GNSS velocity data is essential.

The Cartesian coordinate methods still use geometric equations based on Cartesian coordinates to calculate strain rates. When researchers estimate the strain rate using Cartesian geometric equations in the sphere, the error can be ignored in low-latitude areas but can not be neglected in high-latitude study areas. It is also a problem with the Cartesian coordinate methods, so they are suitable for low-latitude areas but not high-latitude areas. In this paper, we use a rigid body rotation model to verify the superiority of the spherical coordinate method. Checkerboard test in seismic tomography is widely appreciated in geophysical inverse problem resolution tests (Day et al., 2001; Glahn et al., 1993; Graeber et al., 2002; Rawlinson et al., 2014; Walck & Clayton, 1987). The model consists of a regular grid of alternating positive and negative values, which can also be extended to three dimensions. The advantage of the checkerboard test is that it can detect the resolution and uncertainty of seismic wave inversion results visually and quickly. Because GNSS stations are limited and there are few sampling points in local areas, we imitate the checkerboard test using a spherical harmonic function to check the resolution of the strain rate calculation method. The spherical harmonic function is a continuous function that exhibits a regular lattice of positive and negative values under certain circumstances. We judge the method's merits by observing the degree of recovery of the spherical harmonic function by the inversion method. Using the spherical harmonic test model, we can also conclude that the spherical spline algorithm possesses high resolution.

In this article, we first introduce the spherical spline smoothing algorithm and method of calculating strain rate. Then, using the 3571 station sites of continental China and its surroundings from CMONOC I, CMONOC II, and the other sources, we establish a rotation of the rigid body and spherical harmonics models to examine the spherical spline smoothing algorithm. Finally, we calculate the strain rate field in continental China, analyze the correlation between the strain rate field and the earthquake source mechanism, and discuss the earthquake rate in continental China.

2 Seismic Activity and Tectonics Setting of Continental China

The seismic zone in continental China extends along active faults and orogenic zones and is very active (Wang et al., 2001; Yin, 2010). Figure 1 shows recent earthquake events and a significant tectonic setting in mainland China following Li et al. (2012), Xu et al. (2017), Yang et al. (2014), and Zhang (2013). The plate tectonics of continental China is complex. In general, it is divided into two major domains, east and west (i.e., Wang et al., 2011; Zheng et al., 2013), based on $105°E$ (i.e., Liu et al., 2007; Rui & Stamps, 2019). Eastern China mainly includes the NCB (Northeast China Block), the NCC (North China Craton), and the SCB (South China Block). Northeast China is part of the Eurasian plate, and the vast Songliao Basin is rich in oil and gas resources. At the same time, the Yilan-Yitong Fault and the Changbai Mountain Range are surrounded by frequent seismic activity. Separated from the Northeast Block by the ZBFZ (Zhangjiakou-Bohai Fault Zone), the NCC consists of the North China Plain, Ordos Block, and the SRZ (Shanxi Rift Zone) (Wang & Shen, 2020; Zheng et al., 2013). Their border zones are all very seismically active areas, and the Tangshan earthquake occurred at the intersection of the ZBFZ and the TLFZ (Tan-Lu Fault Zone). The SCB and the NCC are divided by the Qinling-Dabie Suture Zone. The SCB consists of the Yangzi Craton and the South China Fold Belt separated by the Jiao-Shao Fault (Zheng et al., 2013). This area is relatively stable and with few major earthquakes. Western China consists mainly of the Qinghai-Tibet Plateau and several important basins and blocks (i.e., Tarim, Qaidam, Junggar, and Alashan), which are divided by several large faults and orogen belts (i.e., West and East Kunlun Fault, ATF (Altyn Tagh Fault), Qilian-Haiyuan Fault, and South and North Tian Shan Orogen belt). Because the Qinghai-Tibet Plateau is directly extruded by the northeastern direction of the Indian Plate, its interior and the Himalayan Orogenic Belt at the boundary are highly seismic.

Moreover, the extrusion of the Qinghai-Tibet Plateau to the east collided with the South China block, causing frequent earthquakes in the Xianshuihe-Xiaojiang Fault and the Longmen Shan Fault, which are ones of the world's most active faults and where the Wenchuan earthquake occurred. The North and South Tianshan, orogenic belts above the northern part of the Tibetan Plateau, are also very involved in seismic activity because of the far-field effect of the Indian plate thrusting (Yin & Harrison, 2000). Seismicity in the eastern region is weaker than in the western part of China in terms of magnitude and frequency, and earthquakes in both western and eastern China are mainly concentrated at block boundaries and large active structures.

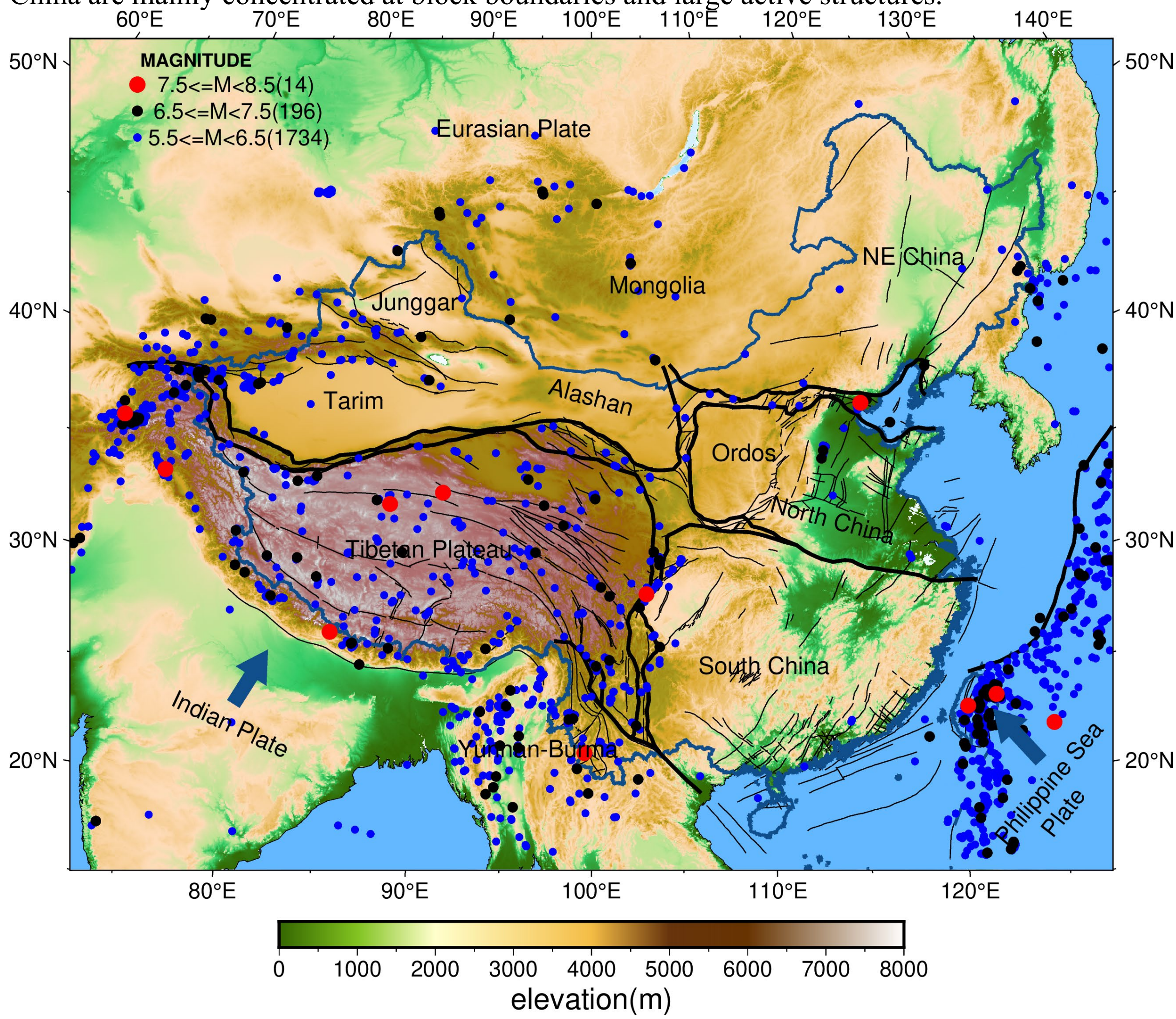

Figure 1. A simple tectonic unit and distribution of earthquake in continental China. The black lines are boundaries of blocks; the deep arrows donate the subduction direction of the Pacific plate

and the Indian Ocean plate; the color dots show seismic hazards with $M \geq 5.5$ from January 1, 1960, to December 31, 2021.

3 Spherical Spline Method

3.1 Gird Meshing and Choosing Scale Factor

Gird meshing in a sphere is always the research focus and previous steps of the interpolation algorithm of discrete data in the spherical surface. This study adopts the method of making spherical surface mesh high-resolution grids with spherical equilateral triangular (Wang & Dahlen, 1995; Wang et al., 1998), which has been used in many studies (Hao et al., 2019; Su et al., 2016; Tape et al., 2009). It is acknowledged that a spherical surface can not be arbitrarily divided into equilateral triangular being like a plane because a maximum of twenty spherical equilateral triangular can be divided on a spherical surface. We link the midpoints of an equilateral triangle to each other, which makes us obtain four equilateral triangles. Then, by repeating this operation, we can get high-resolution grids. We also link the trisection point, which can make us bring mesh of any density cooperating connecting the midpoint. We make a list of relationships with scale factor q (numbers of repeating), numbers of grids (Faces), and spatial support (average angular distance ($\overline{\Delta}$) and side arclength (l)).

Table 1. The relationship between scale factor and spatial scale.

Scale		**Spatial support**	
q	Faces	$\overline{\Delta}$	l
0	20	63.435°	$7053.64km$
1	80	31.718°	$3526.82km$
2	320	15.859°	$1763.41km$
3	1280	7.929°	$881.71.km$
4	5120	3.965°	$440.85km$
5	20480	1.982°	$220.43km$
6	81920	0.991°	$110.21km$
7	327680	0.496°	$55.11km$
8	1310720	0.248°	$27.55km$
9	5242880	0.124°	$13.78km$
10	20971520	0.062°	$6.78km$
11	83886080	0.031°	$3.44km$
12	335544320	0.016°	$1.72km$

We must choose a scale factor for ourselves using the spherical spline algorithm. In this study, we only discuss the scale factor of the station in mainland China and its surrounding regions, and Figure 2 shows the situation of grids meshing for q=12. We have observed that areas with q=9,10 are small, and q=11,12 is none. Finally, we chose q=10 meshing grids in our study. For other situations, the scale factor is selected from 7 to 9 and is not more than 12 (Tape et al., 2009).

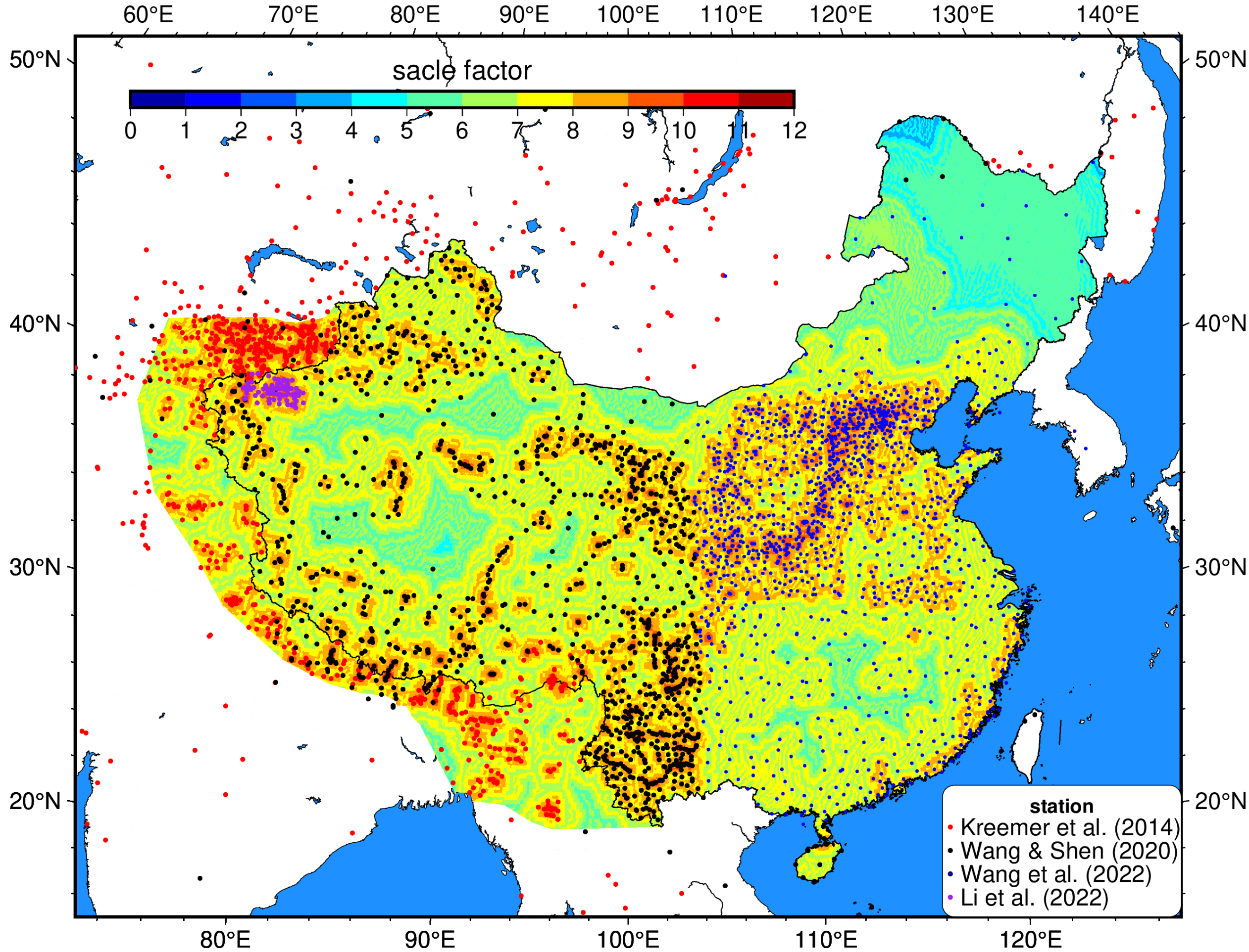

Figure 2. Station of mainland China and example of meshing scale using q=0-12. All station locations are from Wang & Shen (2020), Wang et al. (2022), and Li et al. (2022). The red dots denote GPS stations around continental China combined by Kreemer et al. (2014), which have been used by Wang & Shen (2020) in their research; The black dots represent the GPS station from Wang & Shen (2020); The deep blue dots represent the GPS station from Wang et al. (2022); The purple dots represent the GPS station from Li et al. (2022). Where stations are dense, the meshing of continental China with q=5-12 is available.

3.2 Basis Function of Spherical Spline

We utilize the GNSS station site to define the basic function of the spherical spline (Lancaster & Salakauskas, 1986).

$$f = \begin{cases} \frac{3}{4}\bar{\Delta}^{-3}\Delta^{3} - \frac{6}{4}\bar{\Delta}^{-2}\Delta^{2} + 1, & \Delta \le \bar{\Delta}, \\ -\frac{1}{4}\bar{\Delta}_1^3 + \frac{3}{4}\bar{\Delta}_1^2 - \frac{3}{4}\bar{\Delta}_1 + \frac{1}{4}, & \Delta \le \Delta \le 2\bar{\Delta} \end{cases} \quad (1)$$

where Δ is the angular distance between grid nodes with the station site, $\bar{\Delta} = \frac{\operatorname{acos}\left(\frac{\cos(72°)}{1-\cos(72°)}\right)}{2^q}$ is the angular distance of adjacent grid nodes and $\bar{\Delta}_1 = \frac{\bar{\Delta}-\Delta}{\bar{\Delta}}$. We define θ, φ as codimension and longitude of station sites and θ', φ' *as* codimension and longitude of grid nodes. According to spherical trigonometry, $\Delta = \text{acos}[\cos\theta' \cos\theta + \sin\theta' \sin\theta \cos(\varphi' - \varphi)]$.

Function (2) and function (3) show the basic function of the spherical spline of the first derivative,

$$\begin{cases} \dfrac{\partial f}{\partial \theta} = \dfrac{1}{\bar{\Delta}}\left(\dfrac{9}{4}\bar{\Delta}^{-2}\Delta^2 - 3\bar{\Delta}\Delta\right)\dfrac{\partial \Delta}{\partial \theta} \\ \dfrac{\partial f}{\partial \varphi} = \dfrac{1}{\bar{\Delta}}\left(\dfrac{9}{4}\bar{\Delta}^{-2}\Delta^2 - 3\bar{\Delta}\Delta\right)\dfrac{\partial \Delta'}{\partial \varphi} \end{cases} \qquad 0 \le \Delta \le \bar{\Delta}, \tag{2}$$

$$\begin{cases} \dfrac{\partial f}{\partial \theta} = \dfrac{1}{\bar{\Delta}}\left(-\dfrac{3}{4}\bar{\Delta}_1^2 + \dfrac{3}{2}\bar{\Delta}_1 - \dfrac{3}{4}\right)\dfrac{\partial \Delta}{\partial \theta} \\ \dfrac{\partial f}{\partial \varphi} = \dfrac{1}{\bar{\Delta}}\left(-\dfrac{3}{4}\bar{\Delta}_1^2 + \dfrac{3}{2}\bar{\Delta}_1 - \dfrac{3}{4}\right)\dfrac{\partial \Delta'}{\partial \varphi} \end{cases} \qquad \bar{\Delta} \le \Delta \le \overline{2\Delta}. \tag{3}$$

When station sites and grid nodes are superposition ($\Delta = 0$), we use function (4) as the basic function.

$$f = 1 \qquad \frac{\partial f}{\partial \varphi} = 0 \qquad \frac{\partial f}{\partial \theta} = 0 \tag{4}$$

And when Δ is more than $2\overline{\Delta}$, we use function (5) as the basic function.

$$f = 0 \qquad \frac{\partial f}{\partial \varphi} = 0 \qquad \frac{\partial f}{\partial \theta} = 0 \tag{5}$$

3.3 Decomposition of the Velocity Field in Spherical Spline

The velocity field tangent to the sphere can be resolved as the sum of two vectors (function (6)),

$$v(\theta, \varphi) = v_\lambda(\theta, \varphi)\hat{\theta} + v_\varphi(\theta, \varphi)\hat{\varphi}, \tag{6}$$

where $\hat{\theta}$, $\hat{\varphi}$ are two unit vectors with south-north and east-west directions and θ , φ is codimension and longitudes of station sites. It is acknowledged that any scalar function $g \in L^2(S^2)$ can be written as the product of two vectors,

$$g(x, y) = \sum_{k=1}^{M} m_k g_k(x, y) = g_k^T(x, y)m. \tag{7}$$

Thus, function (6) can be rewritten as

$$v(\theta, \varphi) = \sum_{k=1}^{M} a_k f_k(\theta, \varphi)\,\hat{\theta} + \sum_{k=1}^{M} b_k f_k(\theta, \varphi)\,\hat{\varphi}. \tag{8}$$

Function (8) is discrete by observation sites (θ_i, φ_i), $i = 1, \dots\dots, N$, as

$$\begin{cases} v_\theta^i = \sum_{k=1}^{M} a_k f_k(\theta_i, \varphi_i) + n_\theta^i \\ v_\varphi^i = \sum_{k=1}^{M} b_k f_k(\theta_i, \varphi_i) + n_\varphi^i \end{cases}, \tag{9}$$

where v_θ^i, v_φ^i are the velocity of the solo station whose observation errors are denoted by n_θ^i, n_φ^i. Two equations of function (9) possess the same form; thus, estimation methods of a_k, b_k are also the same. We rewrite function (9) as matrix form,

$$\mathbf{d} = \mathbf{Fm} + \mathbf{n}, \tag{10}$$

where **d** is a column vector composed by v_θ^i or v_φ^i, **F** is a designed matrix composed of a quantity of spherical spline basis function, **m** is a column vector consisting of the model parameter, which is an unknown quantity to be solved, and **n** is a column vector composed of observation error. Function (10) is an ill-posed equation whose solution is not unique. Thus, we obtain model parameter **n** by least-squares functional,

$$G(\mathbf{m}) = \frac{1}{2}(\mathbf{Fm} - \mathbf{d})^T \mathbf{C}_D^{-1}(\mathbf{Fm} - \mathbf{d}) + \frac{1}{2}\lambda^2 \mathbf{m}^\mathbf{T}\mathbf{Sm}, \tag{11}$$

where λ controls the smoothness of the solution. Then we make $\frac{dG(\mathbf{m})}{d\mathbf{m}} = 0$ and get

$$\mathbf{m} = (\mathbf{F}^T \mathbf{C}_\mathbf{D}^{-1}\mathbf{F} + \lambda^2\mathbf{S})^{-1}\mathbf{F}^T\mathbf{C}_\mathbf{D}^{-1}\mathbf{d}, \tag{12}$$

where $\mathbf{C_D}$ is east and north velocity correlation acquired on GPS velocity data files. Moreover, we select λ by ordinary cross-validation (Tape et al., 2009). In this section, we only introduce the fitting of the velocity field, but calculating the velocity gradient method is the same.

3.4 Calculating the Strian Field

Calculating the strain rate in our study looks like a three-dimensional spherical surface. Still, we do not obtain radial derivate of velocity component due to GPS or GNSS station observing only above the earth's surface. So, we do not discuss the radial strain rate on the spherical surface. Then it is related to v_φ, v_θ when calculating strain rate from the velocity field. The horizontal strain rate is the divergence and its transpose of GNSS velocities in the spherical coordinate system as

$$\begin{cases} \dot{\varepsilon}_\theta = \frac{1}{r}\frac{\partial v_\theta}{\partial \theta} \\ \dot{\varepsilon}_\varphi = \frac{1}{r sin\theta}\frac{\partial v_\varphi}{\partial \varphi} + \frac{v_\theta}{r} cot\theta \\ 2\dot{\varepsilon}_{\theta\varphi} = \frac{1}{r sin\theta}\frac{\partial v_\theta}{\partial \varphi} - \frac{v_\varphi}{r} cot\theta + \frac{1}{r}\frac{\partial v_\varphi}{\partial \theta} \\ 2\dot{\omega}_r = \frac{1}{r}\frac{\partial v_\varphi}{\partial \theta} + \frac{v_\varphi}{r} cot\,\theta - \frac{1}{r\sin\theta}\frac{\partial v_\theta}{\partial \varphi} \end{cases}. \tag{13}$$

4 Detection Model

Because of the uneven distribution of stations, it is a significant issue how researchers estimate horizontal strain rates from these stations. Many adopt different methods to integrate and fit the velocity and strain rate fields, but they always obtain different results, even using the same data sets. Thus, judging a method's merits is a crucial assignment.

First, we present a rigid rotation model to illustrate that the spherical coordinate method is more suitable for calculations on the sphere. Generally, when calculating in the low latitude study area and small study area, the Cartesian method's result is almost identical to the spherical coordinate method. However, the Cartesian coordinate method cannot undertake this mission when the studied area is large-wide or high-latitude.

In addition, we present a spherical harmonics model. We use the spherical spline method to fit the spherical harmonic values generated by the latitude and longitude of each station and compare the results with the theoretical spherical harmonic values to determine the precision and resolution by analogy with the checkerboard test of seismic tomography (Bürgmann, 2005; Lanza et al., 2020; Loveless & Meade, 2010; Métois et al., 2012). It can help us visually judge the merits and effectiveness of the method in study areas.

4.1 Rigid Body Rotation

We assume continental China and its surrounding areas are located inside a rigid plate that only orbits a synthetic Euler polar with an angular velocity of $5 \times 10^{-8}\, rad/yr$. Then we calculate the linear velocity component v_θ (south-north direction), v_φ (east-west direction) of every station in our study areas. When a plate as a rigid body revolves, it has no deformation. The normal and shear strain rates are zero relative to the angular velocity. The rotation rate is not zero.

Function (14) is the relationship between v_θ, v_φ with latitude and longitude of the Euler polar.

$$\begin{cases} v_\theta = R\Omega\, sin(\varphi - \varphi') \sin\theta' \\ v_\varphi = R\Omega[\cos\varphi \cos\varphi' \cos\theta \cos\theta' - \cos\theta' \sin\theta + \cos\theta \sin\varphi \sin\varphi' \sin\theta'] \end{cases}. \tag{14}$$

According to functions (13-14), we have the rotation rate

$$\omega_{\theta\varphi} = -\frac{\Omega}{sin\theta}(sin\, sin\varphi' sin\theta' + cos\varphi cos\varphi' sin\theta' + cos\theta cos\theta' sin\theta - cos\varphi cos\varphi' \, cos^2\theta \, sin\theta' - cos^2\theta \, sin\varphi sin\varphi' sin\theta'), \tag{15}$$

where θ, φ denote codimension and latitude of GPS or GNSS stations, θ', φ' denote codimension and latitude of the polar axis, R is the radius of the earth, $6371km$ and Ω is angular velocity. Meanwhile, we also get a normal strain rate, and the shear strain rate is zero, which can illustrate that function (14) is correct. Then we input the velocity of stations into a spherical spline program to obtain fitting velocity and rotation rate compared with the theoretical results of the entire study area.

4.2 Spherical Harmonics

The spherical harmonics function is widely applied in the spherical coordinate system. In geophysical studies, we often take the earth as a research object. Because the earth's shape is approximately a sphere, its physics field possesses a spherical symmetric future. Thus, spherical harmonics are widely used in geodesy, meteorology, spherical finite element, and numerical simulation of geodynamics.

We use function (16) to build our spherical harmonics model,

$$Y_l^m(\theta,\varphi) = \sqrt{\frac{(2l+1)(l-m)!}{4\pi(l+m)!}}\, P_l^m(cos\theta)e^{im\varphi}, \qquad -l \le m \le l, \tag{16}$$

where l, m are the order and degree of spherical harmonics, i is the imaginary unit and $P_l^m(x)$ is Associated Legendre Polynomial and,

$$P_l^m(x) = (-1)^m(1-x^2)^{\frac{m}{2}}\frac{d^m}{dx^m}\big(P_l(x)\big).$$

$P_l(x)$ is Orthogonal Legendre polynomial,

$$P_l(x) = \frac{1}{2^l l!}\frac{d^l}{dx^l}(x^2-1)^l. \tag{17}$$

Due to the future of spherical harmonics, its distribution takes on transversal, longitudinal strips or spherical rectangles (Figure 3) when l, m take different numbers. We use the latitude and longitude of GNSS station sites to calculate spherical harmonics values ($Y_l^m(\theta,\varphi)$) of their site. Then, v_φ denote the real part of the values and v_θ denote the imaginary part of the values, which will be inputted into the spherical spline program to obtain fitting velocity and velocity gradient results. Meanwhile, to show the resolution of the method intuitively, we can calculate the longitudinal and latitudinal half-wavelength of spherical harmonics with l, m selected by us. Function (18) is the equation of calculating half-wavelength (Wieczorek & Meschede, 2018),

$$\begin{cases} \lambda_l = \dfrac{2\pi R}{\sqrt{l(l+1)}}, \\ \lambda_m = \dfrac{2\pi R\cos\theta}{l} \end{cases} \tag{18}$$

where λ_l, λ_m are meridional and zonal half-wavelength, θ is colatitude and R is the earth's radius, $6371km$.

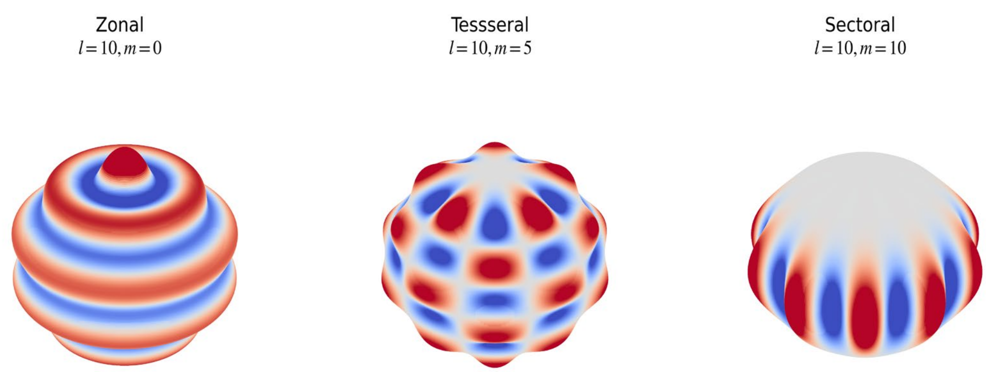

Figure 3. The shape of the strips or lattices produced by the spherical harmonic function on the sphere.

5 Data and Results

In Sections 5 and 6, the stations used by us are from three recent studies (Li et al., 2022; Wang & Shen, 2020; Wang et al., 2022). Wang & Shen (2020) supply complete GPS velocity data for continental China and its surroundings and this dataset has been adopted in many studies (Ge et al., 2022; Li et al., 2021; Pang et al., 2023; She & Fu, 2020; Wang et al., 2022; Zhu et al., 2022). The data set combines the CMONOC I, CMONOC II, and some regional densified stations in continental China, and their observations span from 1991 to 2016. In addition, he has assembled data from several other studies to compensate for the lack of data from surrounding continental China (Kreemer et al., 2014). We then use the North China dataset from Wang et al. (2022) to densify data in Ordos Block and replace the overlapping station portion between this dataset and the dataset from Wang & Shen (2020). The dataset used by Wang et al. (2022) came from Hao et al. (2021), and it multiplied the uncertainty by 3 to make the data fit the noise of the dataset from Wang & Shen (2020), to be able to use the two sets of data together. Finally, we processed the data set from (2022) using the method of Wang et al. (2022) to densify data in North and South TianShan and replace its overlapping parts between Li et al. (2022) and Wang & Shen (2020). Therefore, we finally assembled the data from 3715 stations in and around continental China and removed 144 groups of stations in which the relative error of one of the velocity components exceeded ten percent and the error of the velocity vector magnitude exceeded thirty percent. The 3571 stations we used are labeled in Figure 2.

5.1 Inspection Result of Rigid Body Rotation

Figure 4a shows the artificial linear velocity field (black arrow) of stations revolving around the Euler polar $(90°N, 105°E)$ and theoretical rotation rate (background) correlation with an angular velocity of $5 \times 10^{-8} rad/yr$. Figure 4b shows that the rotation rate calculated by using the spherical spline method is almost identical to the theoretical rotation rate; Figure 4c shows the absolute error of the theoretical and fitting rotation rates. We can observe that the relative error is not more than two thousandths where the difference is largest. In contrast, relative errors in the interior of continental China are mainly under one ten-thousandth. Other strain rate components are calculated by the spherical spline method shown in Figure S1, and their theoretical value is zero. The order of magnitude of the rotation rate is 10^{-8}. Whereas the order of magnitude of strain rate components in Figure S1 is 10^{-11}, and the largest errors are on the boundary. Thus, the result calculated by the spherical spline method can be better.

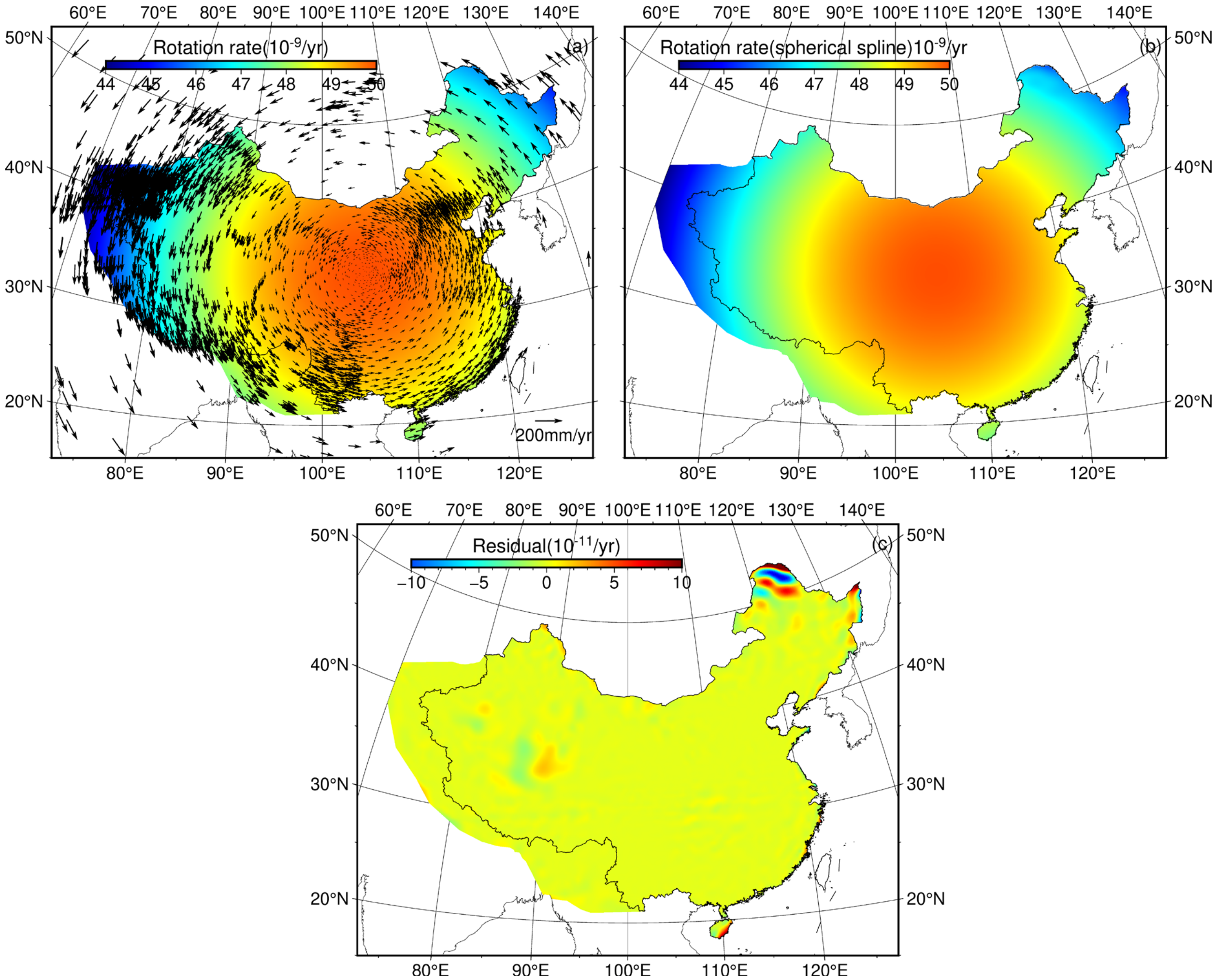

Figure 4. Theoretical result and estimated result of rotation rate. (a) Theoretical result of rotation rate and artificial velocity (black arrow). (b) result of the spherical spline. (c) absolute error (difference between theoretical results and estimated results).

Figure 5a shows the linear velocity field (black arrow) of stations revolving around the Euler polar $(35°N, 105°E)$ and theoretical rotation rate (background) with an angular velocity of $5 \times 10^{-8} rad/yr$; Figure 5b shows that the rotation rate calculated using the spherical spline method is almost identical to the theoretical rotation rate; Figure 5c shows the absolute error of the theoretical and fitting rotation rate. The result showed similar characteristics to Figure 4. Other strain rate components with zero theoretical results are shown in Figure S2, which also indicates similar futures to Figure S1.

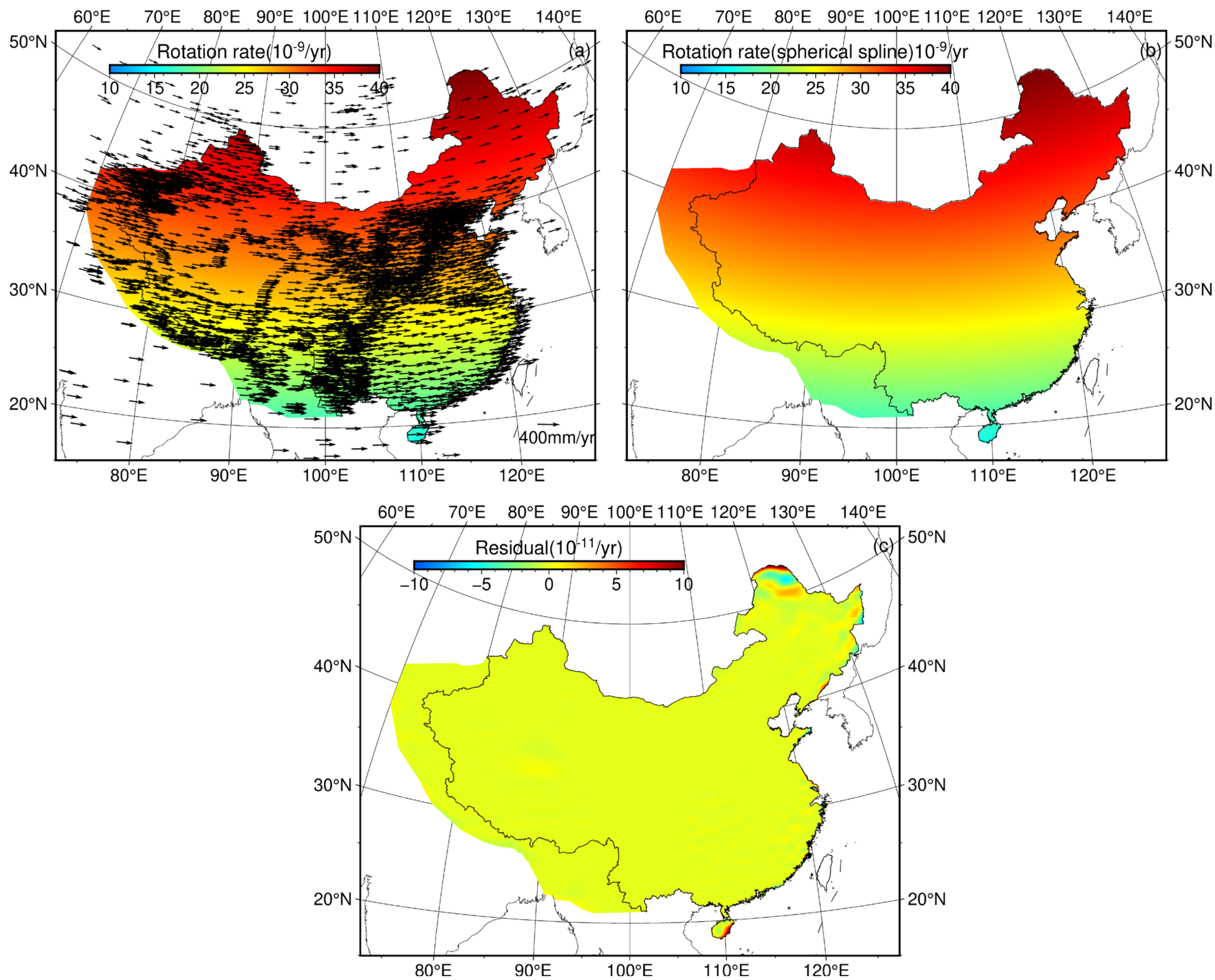

Figure 5. Theoretical result and estimated result of rotation rate. (a) Theoretical result of rotation rate and synthetic velocity (black arrow). (b) result of the spherical spline. (c) absolute error (difference between theoretical results and estimated results).

5.2 Inspection Result of Spherical Harmonics

Figure 6 shows the detection result of velocity. Figure 6a and 6c, respectively, show synthetic gridding v_θ and v_φ, which are imaginary parts and real parts of spherical harmonics with $l = 64, m = 32$. According to function (22), we can obtain that south-north direction half-wavelength λ_l is about $620km$, earth-west direction half-wavelength λ_m is about $567km$ at $25°N$ and earth-west direction half-wavelength λ_m is about $402km$ at $50°N$. Figure 5b and 6d, respectively. They exhibit a relationship between the fitting result of spherical spline and station density. We can observe that where stations are density and uniform, fitting results by spherical spline and theoretical v_θ, v_φ are consistent, and where there are no stations ($32°N$ to $37°N$, $81°E$ to $92°E$), the grids of spherical harmonics are blurred, but the shape is still visible.

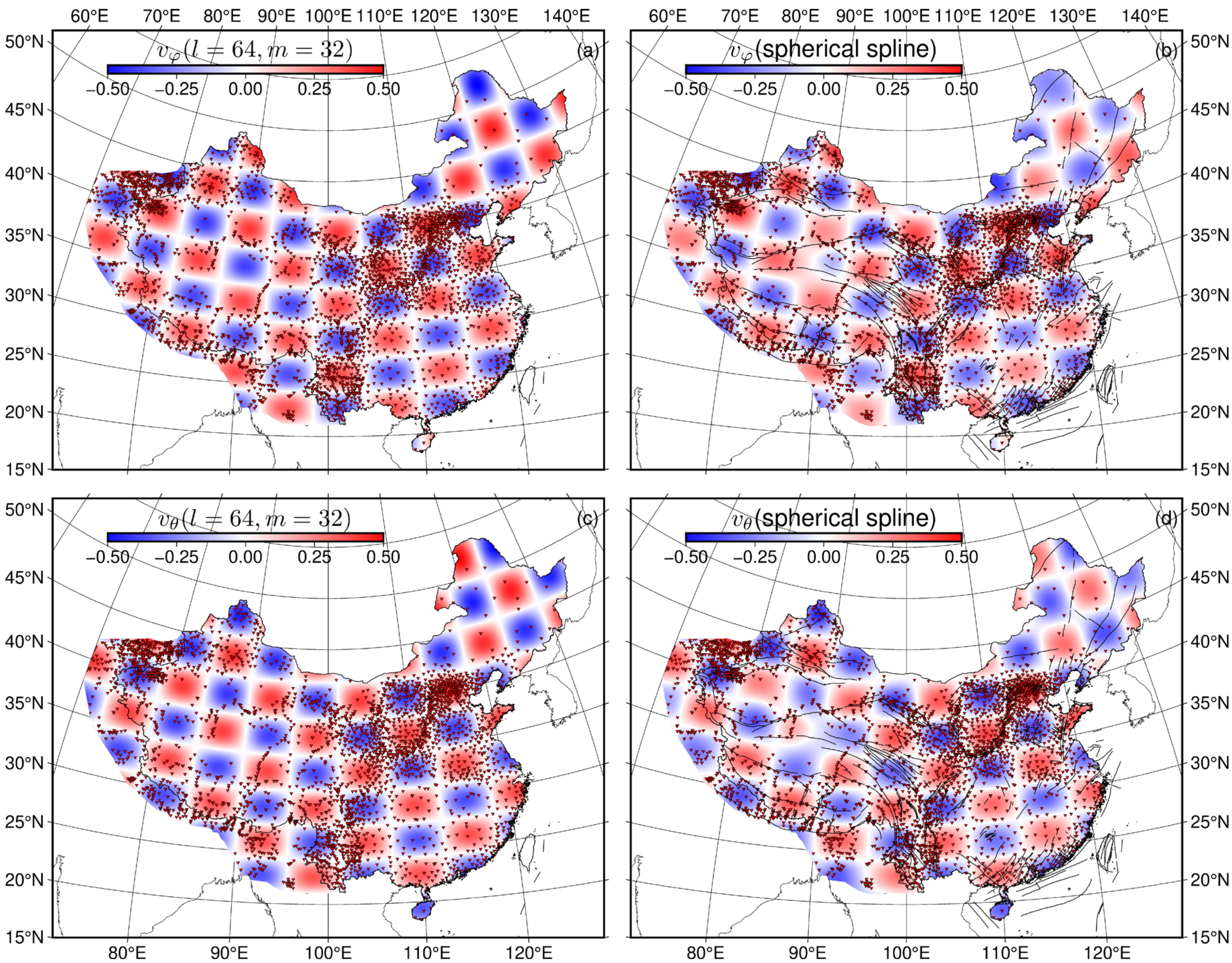

Figure 6. The spherical harmonics with $l = 64, m = 32$ and fitting results of the spherical spline. (a) v_φ calculated by spherical harmonics. (b) v_φ fitted by spherical spline. (c) v_θ calculated by spherical harmonics. (d) v_θ fitted by spherical spline. The rad inverted triangles are all stations of continental China and the surroundings from Figure 1, and the black lines on the background donate significant activity tectonics of continental China (same as Figure 6-9 and Figure S3-S8).

Figure 7 shows the detection result of the velocity gradient. Figure 7a and 7c, respectively. They illustrate synthetic gridding $\frac{dv_\varphi}{d\theta}, \frac{dv_\theta}{d\theta}$, which are south-north derivatives of the imaginary part and the real part of spherical harmonics with $l = 64, m = 32$. The result showed similar characteristics where stations are density and uniform, fitting the result by spherical spline and theoretical $\frac{dv_\varphi}{d\theta}, \frac{dv_\theta}{d\theta}$ are consistent, and where there are no stations ($32°N$ to $37°N$, $81°E$ to $92°E$), the grids of spherical harmonics are blurred, but the shape is still visible in Figure 7.

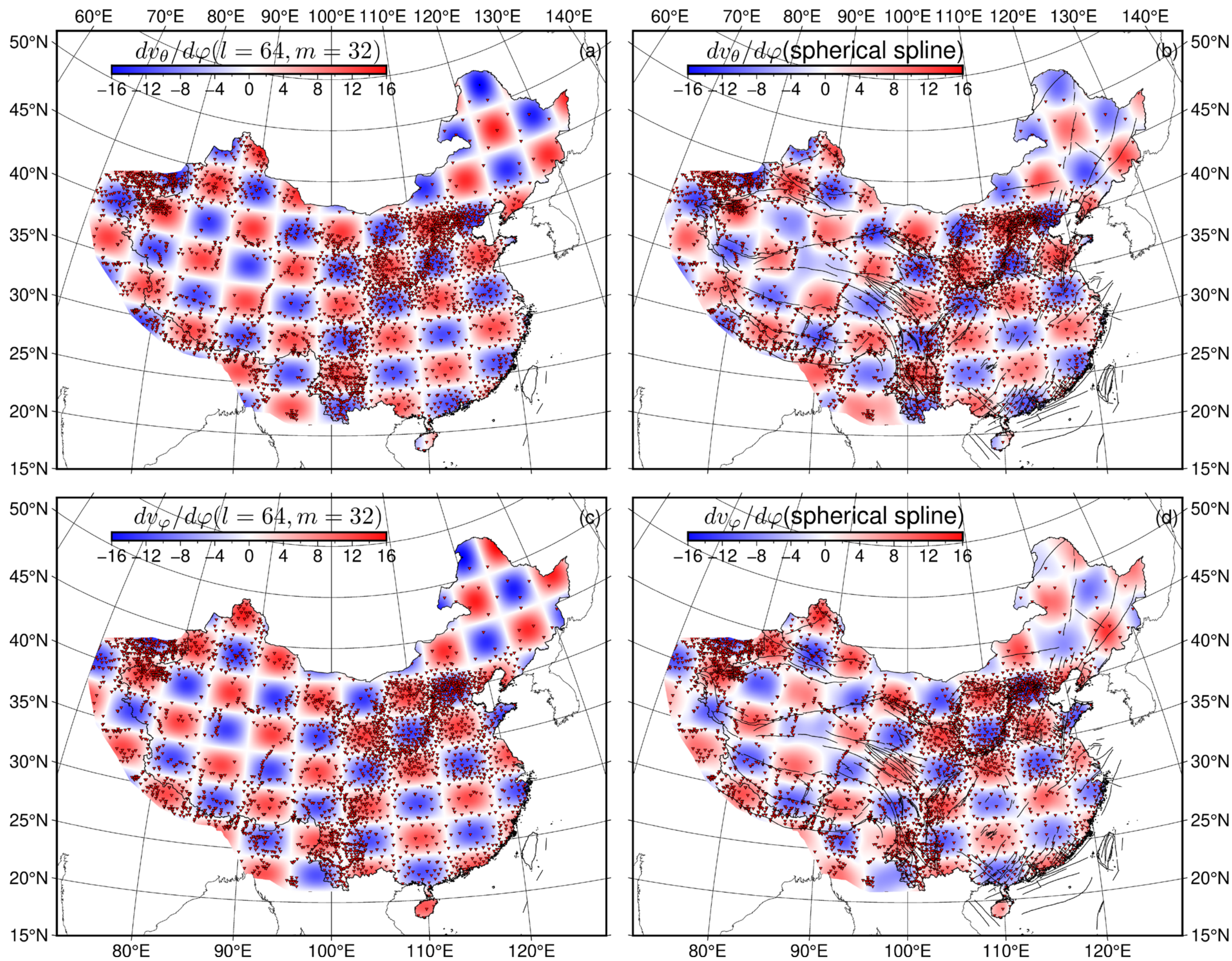

Figure 7. The latitude direction gradient of spherical harmonics with $l = 64, m = 32$ and fitting results of the spherical spline. (a) $\frac{dv_\varphi}{d\theta}$ calculated by spherical harmonics. (b) $\frac{dv_\varphi}{d\theta}$ fitted by spherical spline. (c) $\frac{dv_\theta}{d\theta}$ calculated by spherical harmonics. (d) $\frac{dv_\theta}{d\theta}$ fitted by spherical spline.

Figure 8 shows the detection result of velocity using spherical harmonics with $l = 96, m = 48$ to test minimum resolution because its south-north direction half-wavelength λ_l is about $400km$, earth-west direction half-wavelength λ_m is about $360km$ at $25°N$ and earth-west direction half-wavelength λ_m is about $260km$ at $50°N$. So, the purpose of this detection model is to confirm whether the spherical spline method processes the ability to distinguish the strain rate of minor structures (scale of about $300km$) in dense station areas such as the Pamir Plateau, Tianshan structure zone, Sichuan, Yunnan, Ordos block, North China seismic zone, and South China region. Figure 8a and 8c, respectively, show artificial gridding v_θ, v_φ , which are imaginary parts and real parts of spherical harmonics with $l = 96, m = 48$. Figure 8b and 8d, respectively. They show the relationship between the fitting result of spherical spline and station density.

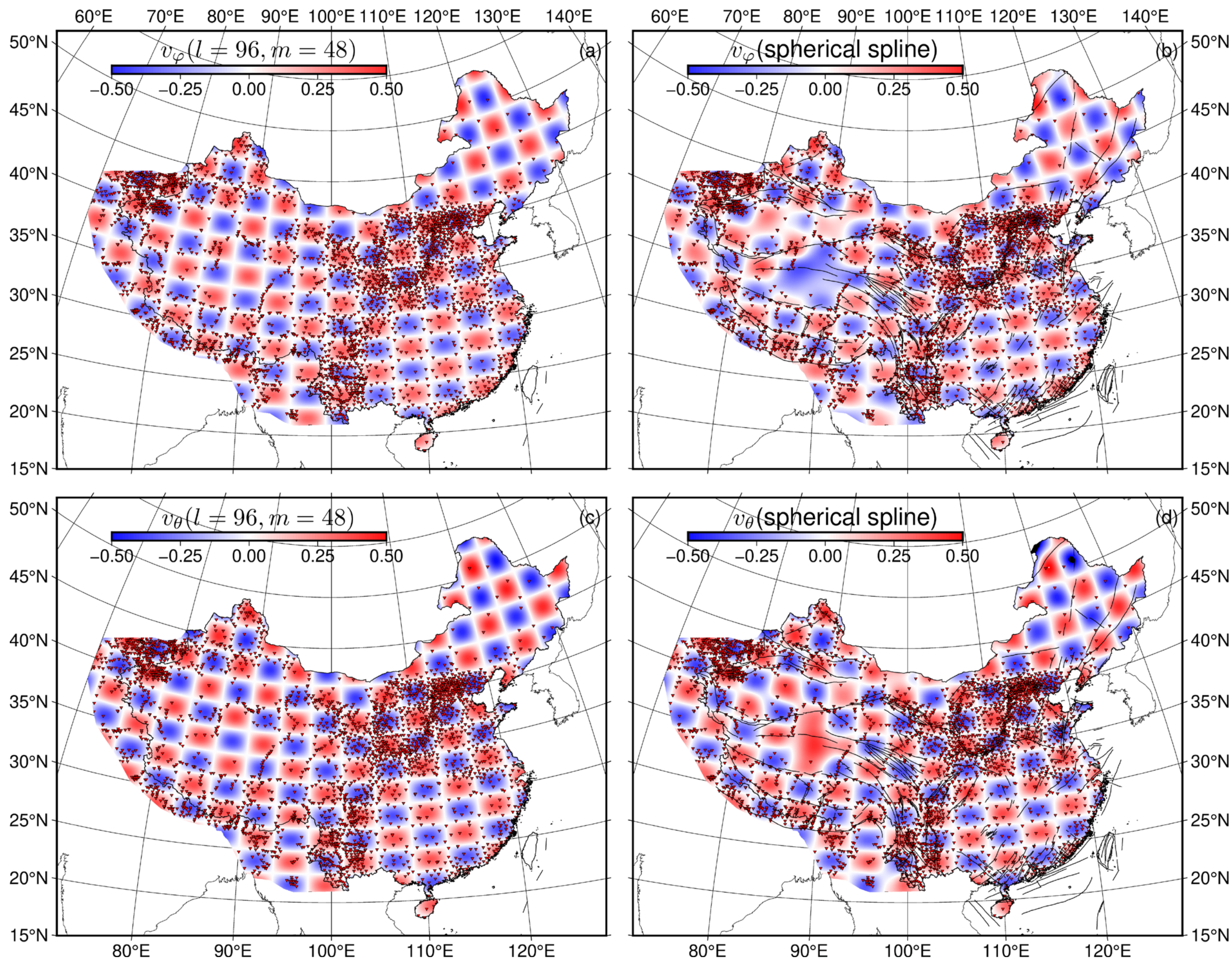

Figure 8. Spherical harmonics with $l = 98, m = 64$ and fitting results of the spherical spline. (a) v_φ calculated by the spherical harmonics function. (b) v_φ fitted by spherical spline. (c) v_θ calculated by spherical harmonics function; (b) v_θ fitted by spherical spline.

Figure 9 shows the fitting detection result of velocity. Figure 9a and 9c, respectively. They show synthetic gridding $\frac{dv_\varphi}{d\theta}, \frac{dv_\theta}{d\theta}$, which are south-north derivatives of the imaginary part and real part of spherical harmonics with $l = 96, m = 48$. The result showed similar characteristics where stations are density and uniform. Fitting the result by spherical spline and theoretical $\frac{dv_\varphi}{d\theta}, \frac{dv_\theta}{d\theta}$ are consistent with figure 9. The results of all strain rates are the sum of the multiples of velocity and velocity gradient. Their characteristics are like the above results. So, they are not shown in the main text but in Figure S3-S8.

From the results of the above two experiments, we can conclude that the spherical spline results we can still give confidence to the strain rate results calculated by the spherical spline of large structures over 600 km in areas where stations are sparse or even absent. Furthermore, in areas with dense or uniform stations, the spherical spline can also reveal the correspondence between structures and strain rates at scales below 300 km or even smaller.

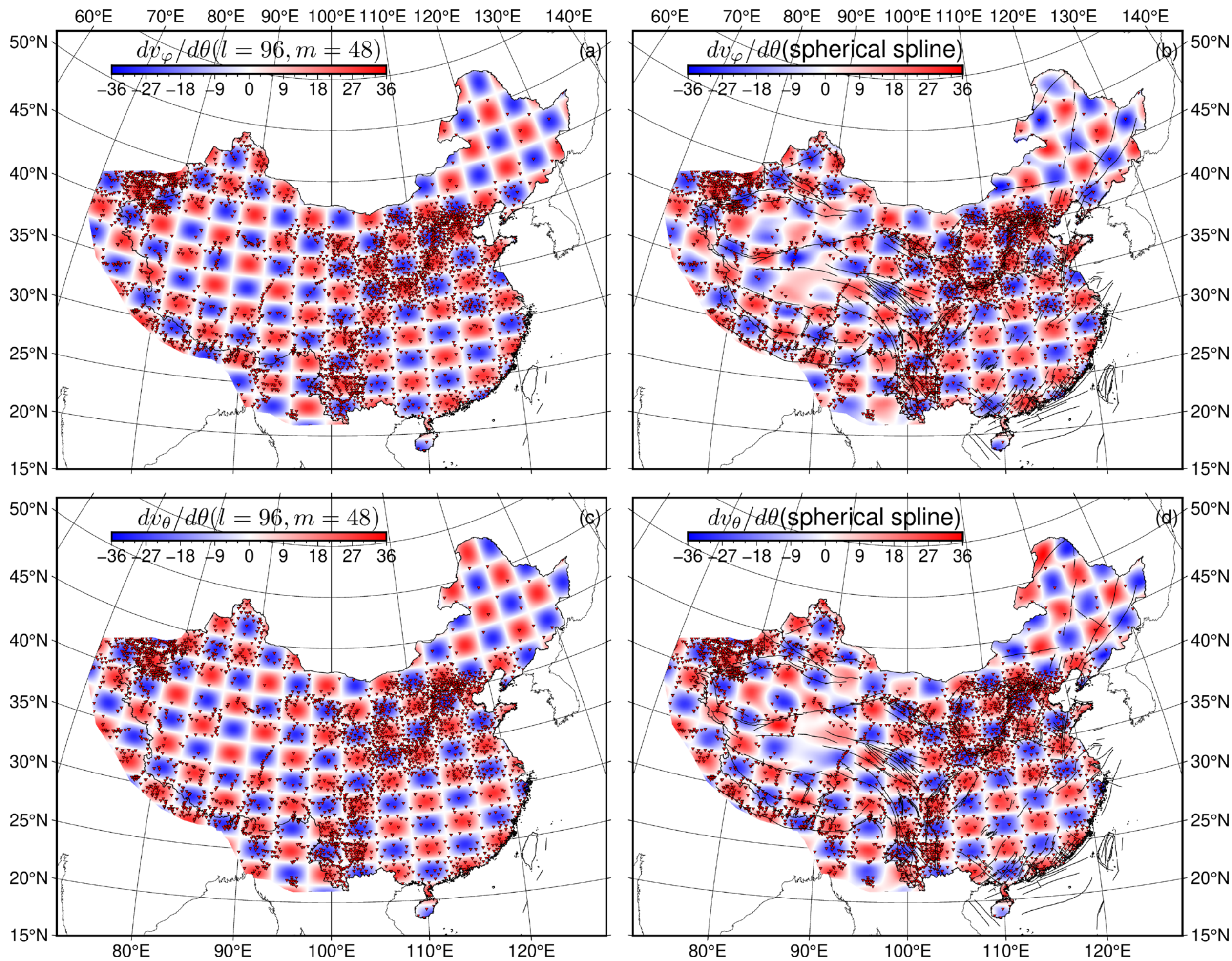

Figure 9. The Gradient of spherical harmonics with $l = 96, m = 48$ and fitting results of the spherical spline. (a) $\frac{dv_\varphi}{d\theta}$ calculated by spherical harmonics. (b) $\frac{dv_\varphi}{d\theta}$ fitted by spherical spline. (c) $\frac{dv_\theta}{d\theta}$ calculated by spherical harmonics. (d) $\frac{dv_\theta}{d\theta}$ fitted by spherical spline.

6 Seismic Mechanism and Strain Rate of Continental China

The Chinese mainland is an active geological tectonic area in a unique tectonic setting where the Eurasian Plate, Indian Plate, and Philippines Sea Plate meet in a triangular framework. As a result of the squeeze from India and the Philippine Sea Plate, earthquake in continental China is quite active. The M 7.8 earthquake in Tangshan in 1976 caused the death of 200,000 people; The M 8.1 earthquake in Hohxil in 2001 was the largest in China since 1960; The 2008 Wenchuan earthquake in Sichuan took nearly 70,000 lives and caused economic losses of almost 85 million RMB. Therefore, the study of seismic activity is of great importance to people's livelihoods and the economy. Studying the strain rate of the shallow ground is an essential reference for understanding the seismic mechanism.

The source of the GNSS velocity data we use is the same as in Section 4. In section 4, we only used the station locations.In contrast, in this section, we will use the measured GNSS velocity data to calculate the strain rate for continental China using the spherical spline method. Figure 10 shows the velocity vector of all stations in continental China and its surroundings. For the accuracy of the calculation results, we excluded the data where the relative error of velocity components exceeded 10% and the relative error of velocity vector size exceeded 30%.

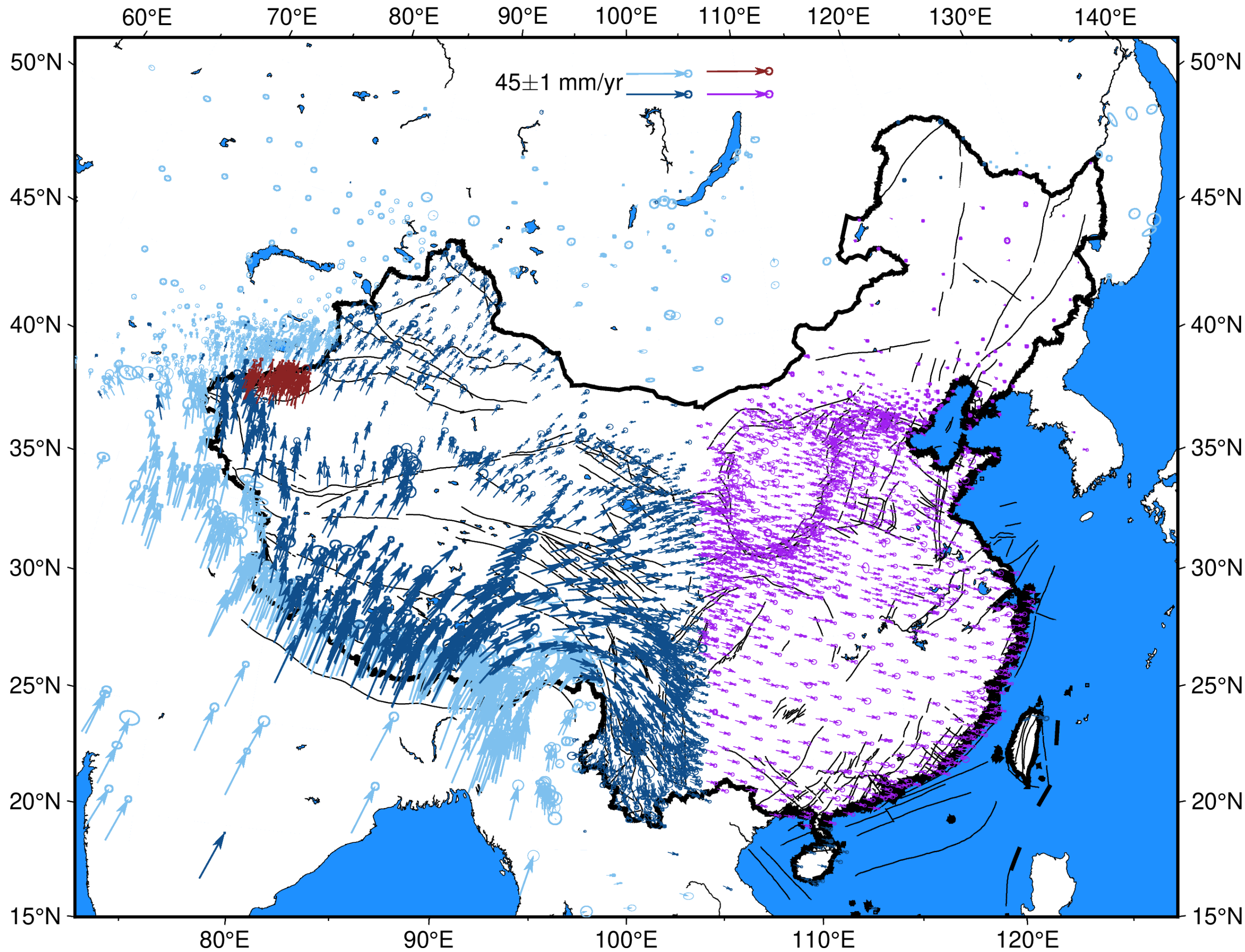

Figure 10. GNSS velocity. The deep blue arrows are from Wang & Shen (2020); the light blue arrows are from Kreemer et al. (2014); the brown arrows are from Li et al. (2022); the purple arrows are from Wang et al. (2022). Wang et al. (2022) processed Ordos data from Hao et al. (2021) so that it would agree with the reference system and noise level of Wang & Shen (2020). We processed data from Li et al. (2022) using the same methodology. All GNSS velocity is listed in Table S1.

The background of Figure 11 shows the dilatation of continental China, whose negative is extrusion and the positive is tension. Due to the north-eastward extrusion of the Indian plate, the largest strain on the Chinese mainland is in the subduction zone of the Himalayan Main Thrust, where the dilatation rate exceeds $-40 \times 10^{-9}/yr$. On the eastern side of the Himalayan Main Thrust, the dilatation rate reaches about $-80 \times 10^{-9}/yr$, caused by the lateral extrusion of the Tibetan plateau being blocked by the SCB (Leigh H. Royden et al., 1997; Zhang et al., 2018; Zhang et al., 2004). The deformation of the Gan-Yushu Fault, XSHF, the Xiangjiang River Fault, and the Red River Fault region in the junction of the Tibetan Plateau and the SCB is to the vertical direction of the extrusion overflow and greater than the extrusion, so these areas generally exhibit a tensile nature (Bai et al., 2010; Zhao et al., 2022). We believe that it is also due to the lateral extrusion of the Qinghai-Tibet Plateau caused by the South China plate blocking it from overflowing in the vertical direction. The seismic mechanism can also explain this in this area exhibiting strike-slip or normal fault. The interior of the Qinghai-Tibet Plateau may also be vertically overflowing when squeezed, so the overall deformation is in tension. At the same time, the seismic mechanism of this region can also indicate this. The northeastern and northern margin of the Qinghai-Tibet Plateau is influenced by the far plant of the Indian plate extrusion, so this area receives extrusion. Figure 11 demonstrates the extrusive nature of the fault system along the northern and northeastern margins of the Tibetan Plateau, and the dilatation rate in this area is between $-15 \times 10^{-9}/yr$ and $-20 \times 10^{-9}/yr$. Also affected by the compression of the Indian plate is the Tianshan orogenic belt, which has a dilatation rate of $-40 \times 10^{-9}/yr$ at the subduction front. At the same time, Figure 11 shows the extrusion strain zone in the eastward extension of North and South Tianshan with a dilatation rate of $-10 \times 10^{-9}/yr$. The seismogenic mechanisms of the northern and northeastern margins of the Qinghai-Tibet Plateau and the Tien Shan frontal margin have been dominated by thrust faulting consistent with the dilatation rate results. And the greater the magnitude of the dilatation rate, the more frequent the earthquakes. Seismic activity and mechanism of western China are correlated with the dilatation rate. Reverse-fault earthquakes frequently occur in regions with negative dilatation rates, and normal-fault or strike-slip earthquakes occur in areas with positive dilatation rates. Although fewer large earthquakes exist in Eastern China, the dilatation results also show this pattern. The Longmenshan Fault, located at the junction of East and West China, is considerably squeezed, and t reverse-fault earthquakes dominate the frequency of earthquakes in this area. However, positive fault earthquakes dominate the East Kunlun F., Ganzi-Yushu F., and Jiali F. to the west. Figure 11 dilatation rate results clearly show this pattern, indicating that our dilatation rate results possess high resolution. The dilatation rate of the North China seismic zone in the East China region is relatively complex. The intersection of the Zhangjiakou-Bohai seismic zone and the Tanlu Fault has the largest dilatation rate, and the Tangshan earthquake occurred in this area in 1976. In addition, the number of large earthquakes is also higher in this area than in the surrounding regions. The SCB is relatively stable and has never experienced an earthquake of $M \geq 5.5$ since 1960 and the dilatation rate in this region is close to zero.

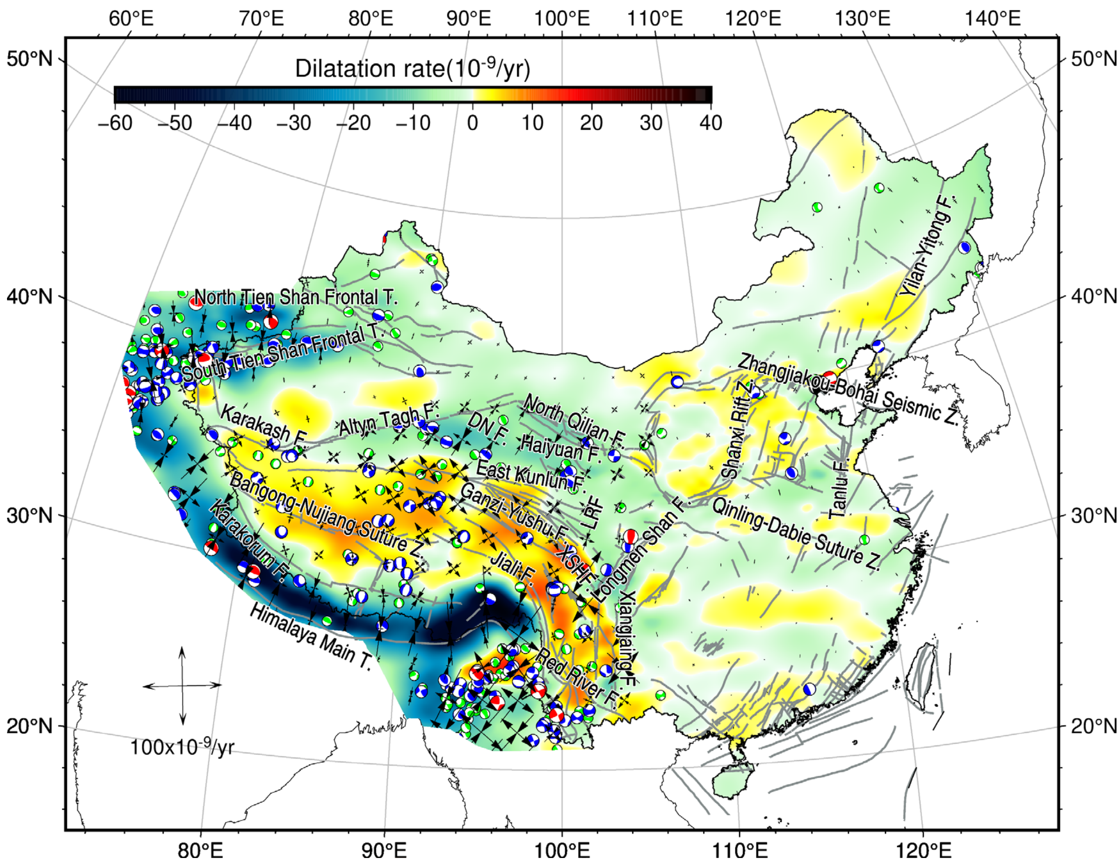

Figure 11. The dilatation rate of continental China. The gray lines on the background denote activity tectonic in continental China; The crossed arrows indicate the magnitude and direction of the maximum and minimum principal strains. The seismic mechanism in continental China from January 1, 1976, to December 31, 2021, is shown in the figure by the focal sphere. The red focal sphere indicates $M \geq 7.5$, the deep blue focal sphere indicates $7.5 \geq M \geq 6.5$, and the green focal sphere indicates $6.5 \geq M \geq 5.5$. Fault name abbreviations are as follows: DNF, Danghe-NanshanFault; LRF, Longriba Fault; XSHF, Xiashuihe Fault.

The background in Figure 12 shows the MSSR (maximum shear strain rate). We still see a clear division between East and West China along $105\,°E$. MSSR is strongly correlated with earthquakes whose source mechanisms are strike-slip faults. In Figure 12, we can conclude that the areas with an MSSR greater than $40 \times 10^{-9}/yr$ are widely distributed on strike-slip faults and reverse-fault earthquakes. By the collisional compression of the Indian plate, the MSSR in continental China is greatest in the western and eastern sections of the HMT. Indian plate directly extrudes the eastern section of the Himalayas, and the MSSR reaches about $100 \times 10^{-9}/yr$. While the eastern section is rotated due to lateral extrusion from the Tibetan plateau, the MSSR reaches about $120 \times 10^{-9}/yr$. Longmenshan Fault, Xiangjiang Fault, and XSHF are located at the junction of Qinghai-Tibetan Plateau and SCB under great compression, and the MSSR has also reached $100 \times 10^{-9}/yr$. The MSSR of the North and South Tianshan Frontal Thrust, influenced by the far field of the Indian Plate extrusion, reaches about $70 \times 10^{-9}/yr$. In the northern and northeastern margins of the Tibetan Plateau, the MSSR show a clear boundary with the stable blocks in the north. In the areas where strike-slip earthquakes are widely developed in the interior of the Tibetan Plateau, the MSSR is more than $40 \times 10^{-9}/yr$. In East China, except for

Zhangjiakou-Bohai Seismic Zone and Yilan-Yitong Fault, the MSRR of other areas is very small and close to $10 \times 10^{-9}/yr$. The MSRR in most of Eastern China is very small, close to $10 \times 10^{-9}/yr$. Only ZBSZ and YYF have MSRR close to $40 \times 10^{-9}/yr$, and there is also some large earthquake distribution. Due to the special plate tectonics of the Chinese continent, the Tibetan Plateau is blocked by the surrounding rigid blocks as it expands outward under compression. All strain rate data are listed in Table S2-S4.

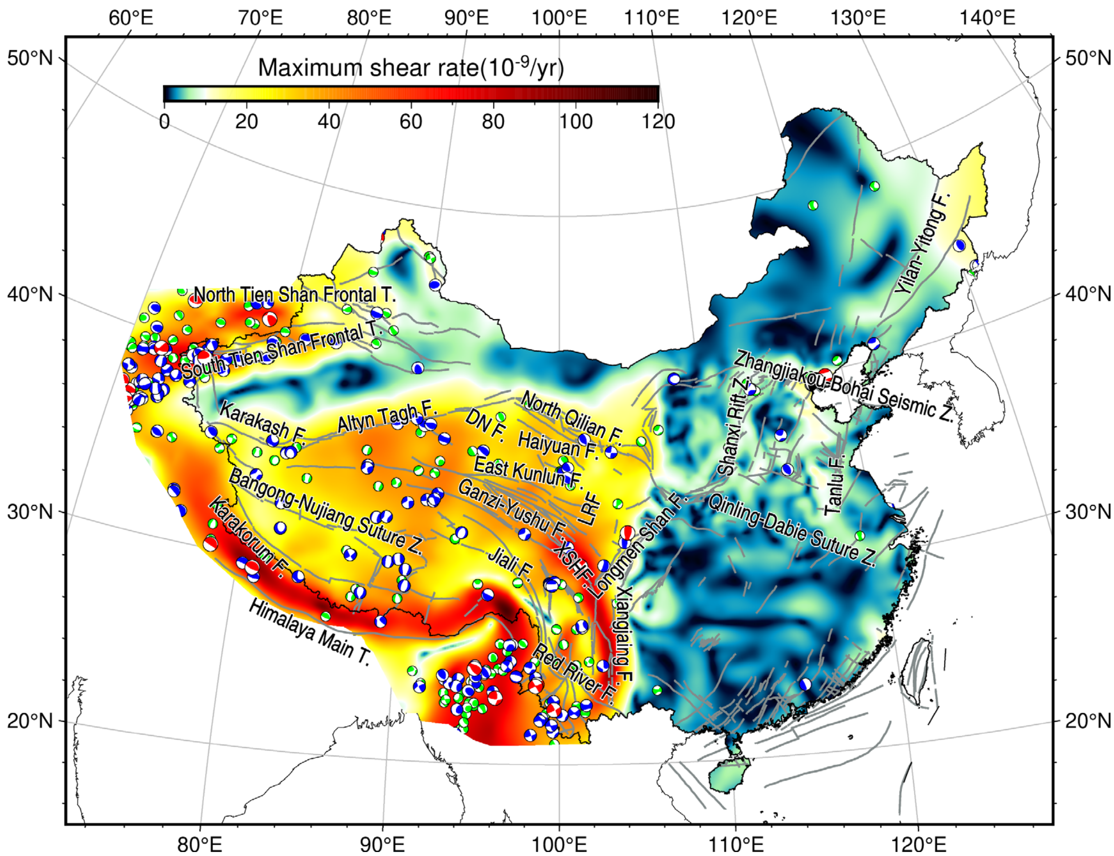

Figure 12. The maximum shear rate of continental China. The gray lines on the background denote active tectonic in continental China. The seismic mechanism in continental China from January 1, 1960, to December 31, 2021, is shown in the figure by the focal sphere. The red focal sphere indicates $M \geq 7.5$, the deep blue focal sphere indicates $7.5 \geq M \geq 6.5$, and the green focal sphere indicates $6.5 \geq M \geq 5.5$ (same as Figure 11).

7 Discussions

7.1 Deformation and Strain Rates of Continental China

7.1.1 Overview of Continental China

Because of the multiscale spherical spline interpolation method, our dilatation rate results (Figure 11 and Figure 12) improve the resolution of the primary structure compared to the previous ones (Rui & Stamps, 2019; Wang & Shen, 2020). Continent China is located in the squeeze triangle of the Indian and Pacific plates and is extremely active in tectonic activities. We propose a concept named 10^{-8} Shear Zone to visualize the influence of the extrusion of these two plates on the deformation of the entire Chinese continent, and we can observe this shear zone in Figure 12. The central part of the 10^{-8} Shear Zone starts at Karakorum F. in the east, extends to ATF and NQF (North Qianlian F.), and curves upward to Northwest Ordos. Then, this shear zone extends down the western edge of the Ordos, passes through the Qinling Mountains, extends the Shanxi Rift Z. on the eastern edge of the Ordos northward to Zhangjiakou, and finally extends the ZBSZ eastward to the Bohai Sea. In addition, there are two other important branches of this shear zone. The first branch extends to the junction of the Southern Tien Shan and the Tarim Basin, then northward in the middle of the Southern Tien Shan to the middle of the Northern Tien Shan, dividing the entire Northern and Southern Tien Shan into East and Western sections. This section of the branch shear zone is connected to the main shear zone on the west side of KF (Karakash F.). Another branch extends through LMSF (Longmen Shan F.) and XJF (Xiaojiang F.), joining the main shear zone in southwest of Ordos. This branch also coincides with the boundary between the Tibetan Plateau and South China. We can see that the tensile and compressive strains within the blocks around the Tibetan Plateau, such as the Tarim block, the Alashan block, the Ordos block, and the South China block, are small in Figure 11. At the same time, the maximum shear strains of these blocks are also small in Figure 12, indicating that these blocks exhibit rigid body properties. But the effects of the squeeze don't go away, with far-field effects affecting areas further afield. Tianshan's high shear strain rate and high extrusion strain rate result from the influence of far-field benefits. Thus, in western China and around the $105°E$, the 10^{-8} Shear Zone mainly indicates the extent of influence of the Indian subcontinent squeezing continental China. Although North China is affected by the dual far-field effects of the Tibetan Plateau and the Pacific Plate, the 10^{-8} Shear Zone also indicates their influence. This shear zone provides visual evidence of the extent to which localized deformation in continental China is affected by plate extrusion and avoids attributing deformations whose causes are unclear to plate extrusion or its far-field effects.

7.1.2 Deformation of Tibetan Plateau

The Tibetan Plateau is inevitably one of continental China's most dramatic active tectonics. The thickening, shortening, and lateral extrusion of the Tibetan Plateau under the compression of the Indian plate and the blocking of surrounding blocks is noticeable and almost indisputable (Gan et al., 2007). However, whether crustal thickening or lateral extrusion played a major role in balancing the plateau's uplift is still controversial. An accurate description of the deformation of the Tibetan Plateau is therefore essential for clarifying these issues. There have been many deformation studies based on GPS velocity fields, and researchers customarily use relative velocity models to delineate microplates and account for their interactions. It may sometimes neglect the overall deformation, so it is more reasonable to use strain rates composed of velocity gradients because the velocity gradient does not vary with the reference system. The microplates of the Tibetan Plateau have been carefully delineated in recent years (Loveless & Meade, 2011; Meade, 2007; Thatcher, 2007; Wang et al., 2017), the microplate model and the continuum deformation model have been harmonized. Rotation has always been a concern in microplate modeling. From our strain rate results, we can get that the internal deformation properties of the Tibetan Plateau tend to be consistent, and the drastic changes in values and properties are mainly at the edge of the Tibetan Plateau. Wang et al. (2017) used the GPS velocity field and microplate model to obtain that the southwestern part of the Tibetan Plateau shows a counterclockwise rotation, the southeastern part shows a clockwise rotation, the Tsaidam Basin shows a clockwise rotation, and the middle part of the Himalaya shows a counterclockwise rotation. In Figure S9, we offer the results of the rotational strain rate where positive values indicate counterclockwise and negative values indicate clockwise. My results generally agree with the nature of Wang et al. (2017) in the southwestern and northeastern Tibetan Plateau, and the nature of the rotation in the Tsaidam Basin and the middle Himalayas is opposite to his results. But our results are identical to those of Ge et al. (2015) and Wang & Shen (2020). Wang et al. (2017) use Ma as the unit of time, and the rotation values in the regions that do not agree with our results are smaller, so there may be some errors in the statistics and calculations. Thus, it follows from our rotational strain rate model that the interior of the Tibetan Plateau may not need to be divided into many microplates to explain deformation. We can see from Fig. 2 that the resolution of our strain rate model on the Tibetan Plateau reaches 110 km at the largest spatial scale (scale factor $q \geq 6$, The larger the scale factor, the higher the resolution), which can fully satisfy the current microplate scale. Of course we don't fully support this model of the Tibetan Plateau as a whole piece. Because our results support the traditional delineation of land parcels bounded by large active tectonics. In Fig. 12, we see the variation of the MSSR on both sides of the BNF to distinguish the Lhasa block from the Qiangtang block. In Fig. 11, we see a change in the nature of the tensile on either side of the EKF (East Kunlun F.) to distinguish the Songpan-Ganzi Block from the Qiangtang Block. There is also a clear zone of high extrusion in the middle of the Qaidam Basin and the Songpan-Ganzi Block. So how can researchers improve the accuracy of numerical experiments to explain the crustal deformation of the Tibetan Plateau without microplates? We believe that it is possible to improve the resolution of the elastic parameters of the material. Our study has given high-resolution strain rates, and high-resolution continuous elastic parameters can be obtained after simple calculations using the Hooke's law (All strain rate data are listed in Table S2-S4). Numerical modeling in conjunction with current plate delineation based on large active ruptures may have been able to give better results.

Another deformation of interest is a crustal circulation channel on the eastern Tibetan Plateau and where it begins and ends. Many researchers believe that the Tibetan Plateau, as it extrudes laterally to the east, is blocked by the tough Sichuan Basin to form northward and southward branches. Branching to the north extends to the RRF (Red River F.), and branching to the east rises to the edge of the Ordos block (Bai et al., 2010; Bao et al., 2015; Zhang et al., 2020). The existence of lower and middle crustal flows has been confirmed by much geophysical observational evidence on the northeast Tibetan Plateau, such as the hyperthermal layer (Deng & Tesauro, 2016; Jiang et al., 2019), the lower and middle crustal low-resistive layers (Zhao et al., 2012), distribution of epicenter depths (Liang et al., 2008; Wang et al., 2020; Wei et al., 2010) and the anisotropy of the crust (Kong et al., 2016; Zheng et al., 2018). There is no evidence of a lubricating or decoupling layer between the lower and middle crust and the upper crust. Therefore, the deformation of the lower and middle crust should be consistent with that of the upper crust. In figure 11, our results show that the crustal flow in the southeastern Tibetan Plateau is divided into two streams, the first one extending from Ganzi-Yushu F., XSHF to XJF., and the other extending from Jiali F. to RRF. It is consistent with the current study. It is also surface observational evidence for the existence of crustal flows. In addition, our results show that the two crustal flow channels are connected near XSHF and XJF. However, our dilatation rates result do not show the effect of crustal flow on the surface in the northeastern Tibetan Plateau, and only the northeastern portion of the Tibetan Plateau showed slightly higher maximum shear rates. It may suggest no large-scale crustal flow in the northeastern Tibetan Plateau or a lubricating layer between the lower and middle crust and the upper crust. Even if there was crustal flow, it didn't spread to the edge of the Ordos Block.

7.1.3 Deformation of North China in Continental China

North China is another region of high seismicity in mainland China, where the deformation and dynamics of the region are of great interest because of the large population and industrial bases and the extrusion of both the eastern side of the Tibetan Plateau and the western Pacific Plate. Figure S9 shows details of strain rates in North China. Our maximum strain rates are similar to the results obtained by the most recent modeling approach using elastic-plastic layering (Shen et al., 2023). The MSSR at the northern edge of the Ordos block is smaller than the other boundaries, showing a semi-enveloped morphology. The MSSR at the northern edge of the Ordos Block is smaller than the different boundaries. It suggests a longer recurrence cycle of strong earthquakes in northern Ordos. Our results differ from Shen et al. (2023) in areas where strain is concentrated. In Figure S10, the eastern part of the Zhangjiakou-Bohai Seismic Zone, where the Tangshan earthquake occurred, is a strain rates concentration area with short recurrence periods of strong earthquakes requiring focused monitoring. In addition, the areas of relatively large strain rates in the North China block are concentrated around the active tectonics, including the Shanxi Rift Z., Anyang-Heze-Linyi F., Weihe Rift, and THCF (Tang Shan-Hejian-Cixian F.). At the boundary between North and South China, Qinling-Dabie Suture Z., there is no stress concentration, and our results are consistent with Shen et al. (2023) and seismological perception (Yu & Chen, 2016). However, we used more intensive measured data to obtain a strain rate model with higher resolution, which also supports the current dominant block models (DENG et al., 2003; Wang et al., 2022; Yin et al., 2015). Thus, our results may be more plausible.

The 10^{-8} shear zone is still in effect in North China, and this zone extends to the THCF and the Tanlu Fault, suggesting that these two active tectonic structures are the concentration of strain in North China as a result of the extrusion of the Tibetan Plateau and the Pacific Plate.

7.2 Seismic Activity and Strain Rates of Continental China

As mentioned earlier in our study, Figure 11 demonstrates that dilatation is highly consistent with the source mechanism of $M \geq 5.5$ earthquakes. Figure 12 demonstrates the agreement of the MSSR with earthquakes on strike-slip faults of $M \geq 5.5$. In addition, there are no major earthquakes in areas where the dilatation rate or the MSSR is anomalous. We consider these areas with abnormal strain rate values as earthquake warning areas. In Figure 11, the dilatation rate along the ATF is approximately $-20 \times 10^{-8}/yr$, and only the western section of the ATF is more seismically intense. In Figure 12, The small MSRR in the east section of the ATF may be why there are fewer large earthquakes in this region. The eastern section of TSFT (TianShan Frontal T.) and the eastern section of the ATF have the same strain rate and seismic distribution characteristics, and this feature is also found in the triangle enclosed by LRF (Longriba F.), XSHF, and LMSF. Although Figures 11 and 12 show that the NQF has this feature again, that is because of the absence of data on the seismic mechanism, and we know from Figure 10 that there is a large distribution of earthquakes in this area. Although the dilatation rate of the western edge of the Ordos block is low, the MSRR is large, especially since the intersection with NQF has the possibility of large earthquakes. The distribution of only a few earthquakes $M \geq 5.5$ in northern China is consistent with the distribution of high values of the dilatation rate and the MSRR, and these areas remain of concern.

7.3 Spherical Spline Method

The spherical spline can directly give a derivative of GNSS velocity, which does not depend on the fitting result of the velocity field. Furthermore, the spherical harmonics detection model shows numerical stability with a large velocity gradient. However, the maximum order and degree of spherical harmonics we use are 96 and 48. We also obtain the ideal results using bigger orders and degrees' spherical harmonics detection model. We observe that there is one station data at the edge of a grid, then this side of the edge of the grid will recover the value sign (positive and negative) of the grid where it is located. (e.g., Figures 5 and 7).

As we mentioned at the beginning of this article, we have developed a set of test criteria to judge whether some methods of calculating strain rate using GPS or GNSS velocity are effective. The criteria do not target spherical spline mainly. In geophysical and geodynamic research, the effectiveness of fitting or smoothing using a different method for the same discrete data has some visible discrepancies. However, only some methods perform well within a large study area. Some methods are better than others in local areas, which is also the principal aspect discussed by researchers when they select fitting or smoothing methods. We present a spherical harmonics grid inspection model by analogy with a seismic wave velocity checkboard test. Using spherical harmonics with a grid distribution feature, we can judge the overall fitting effect of a strain rate calculating method in the study area and consider the local detail resolution of the technique. Even if the same data is used, different methods have different local resolutions, so higher-resolution methods can also be an option in other parts of a larger study area.

Of course, the way to solve the interpolation accuracy and to get a better smoothing effect is to increase the station density locally. However, refining stations in all areas, regardless of cost, is not conducive to cost savings and efficiency, so we use the spherical harmonic grid test model to determine whether the distribution of stations in the study target area is reasonable and improved. We take the station density distribution in continental China as an example. From the results of the spherical harmonic lattice test of the spherical strip, it is necessary to increase the stations in the rectangular area from $32°N$ to $37°N$, $81°E$ to $92°E$. This area has experienced major earthquakes and is in the Tibetan hinterland, a famous no-man's land. However, the deformation mechanism within the Qinghai-Tibet Plateau is still unclear. Based on the spherical spline results, it is unnecessary to deploy stations intensively, but only to add 3-5 stations over a wide range area to significantly improve the resolution of strain rate results. In addition, the spherical harmonic test also shows that adding two or three stations in the hinterland of the Qaidam Basin and the Alashan massif is also beneficial to improving the computational accuracy of the north-south derivatives (which is mainly related to $\dot{\varepsilon}_{\varphi}$). Refining station in other areas is practically unnecessary.

No matter what method or data is used, data can be filtered, and methods can be chosen differently, but the study area is permanently fixed. Although we recommend using different methods in different regions in the previous section, using various methods locally in a fixed study area may have some continuity problems on the boundaries. Moreover, in the last quarter, we mentioned that spherical coordinates are more reliable at high latitudes (e.g., Iceland) or in a large study area at low latitudes (e.g., continental China). Jiang *et al.* (2011) concluded that the least-squares collocation method in spherical coordinates is superior to other methods. However, the least-squares collocation method is based on first-order Taylor expansions of displacement or velocity fields in the spherical and Cartesian coordinate systems. It is like linear interpolation, which can only guarantee the continuity of the strain rate but not the smoothness. This method is reasonable when the stations are dense, but when the stations are sparse, the calculation results are not guaranteed to be practical. Therefore, in addition to proposing a set of test criteria for the strain rate method, this paper also recommends that researchers use the spherical spline method, which is not only a high-precision spherical coordinate method but also ensures continuous and smooth strain rate results.

8 Conclusions

We propose a set of criteria to test the practicality of calculating strain or strain rate fields using GPS or GNSS data. This set of standards is also illustrated using the spherical spline method utilizing the location of stations in and around continental China.

The final three main conclusions drawn in this paper are

(1) Unlike the Cartesian coordinate method, the spherical coordinate method can be adapted to examine rigid body rotation models and reduce the error to less than one percent or even one thousandth. The spherical harmonic grid model is designed to visualize the method's resolution. We can use different sizes and shapes of spherical harmonic grids to examine our strain rate calculation methods rather than just the spherical spline method used in this paper.

(2) The 10^{-8} reveals the extent to which the Chinese mainland is affected by the extrusion of the Indian plate and the extrusion of the Pacific plate. This zone is also valid in North China.

(3) It may be more reasonable to explain the deformation mechanism of the Tibetan Plateau using a continuum model. At the same time, the high-resolution strain rate we provide helps to obtain continuous high-resolution elastic parameters.

(4) We provide strain rate evidence for the distribution of lower and middle crustal flows on the southeastern Tibetan Plateau and inform the connectivity of the two side channels.

(5) The region of high shear strain rate in North China overlaps with the microplate margins delineated by active fault. However, Tangshan is still the region with the highest MSRR and the dilation rate, which needs to be highly emphasized.

(6) The dilatation rate and the MSRR calculated using the spherical spline method have an excellent performance in analyzing the seismic mechanisms of faults or earthquakes. It is recommended that other researchers use the spherical spline method when analyzing the seismic mechanism. Attention must be focused on areas with large dilatation rates and MSRR, especially those anomalous compared to the surrounding areas with a high potential for future major earthquakes.

Acknowledgments

This research is supported by the National Science Foundation of China (U2239205, 41725017) and the National Key R&D Program of the Ministry of Science and Technology of China (2020YFA0713401). It is also partially supported by the National Key Scientific and Technological Infrastructure project "Earth System Science Numerical Simulator Facility" (EarthLab). All the authors greatly appreciate Professor Carl Tape for providing the software package to us.

Open Research

The GNSS data used in this study were taken from published papers (Li et al., 2022; Wang & Shen, 2020; Wang et al., 2022) and are listed in Table S1. The GNSS velocity and strain rate data are published to Zenodo (https://zenodo.org/records/10215151). Earthquake Catalog was obtained from USGS (United States Geological Survey) (https://earthquake.usgs.gov/fdsnws/event/1/query.csv?starttime=1960-01-01%2000:00:00&endtime=2021-12-31%2023:59:59&maxlatitude=55.479&minlatitude=15.824&maxlongitude=138.516&minlongitude=69.082&minmagnitude=5.5&orderby=time). The seismic mechanism data were obtained from the Global Centroid Moment Tensor (Dziewonski et al., 2012; Ekström et al., 2012) (https://www.globalcmt.org/cgi-bin/globalcmt-cgi-bin/CMT5/form?itype=ymd&yr=1976&mo=1&day=1&otype=ymd&oyr=2021&omo=12&oday=31&jyr=1976&jday=1&ojyr=1976&ojday=1&nday=1&lmw=5.5&umw=10&lms=0&ums=10&lmb=0&umb=10&llat=15&ulat=55&llon=70&ulon=140&lhd=0&uhd=1000&lts=-9999&uts=9999&lpe1=0&upe1=90&lpe2=0&upe2=90&list=6).

Reference

Backus, G. (1967). Numerical applications of a formalism for geophysical inverse problems. *Geophysical Journal International, 13*(1-3), 247-276. doi: 10.1111/j.1365-246X.1967.tb02159.x

Backus, G. (1968). The resolving power of gross earth data. *Geophysical Journal International, 16*(2), 169-205. doi: 10.1111/j.1365-246X.1968.tb00216.x

Backus, G. (1970). Uniqueness in the inversion of inaccurate gross earth data. *Royal Society, 266*(1173), 123-192. doi: 10.1098/rsta.1970.0005

Bai, D., Unsworth, M. J., Meju, M. A., Ma, X., Teng, J., Kong, X., et al. (2010). Crustal deformation of the eastern Tibetan plateau revealed by magnetotelluric imaging. *Nature Geoscience, 3*(5), 358-362. doi: 10.1038/ngeo830

Bao, X., Sun, X., Xu, M., Eaton, D. W., Song, X., Wang, L., et al. (2015). Two crustal low-velocity channels beneath SE Tibet revealed by joint inversion of Rayleigh wave dispersion and receiver functions. *Earth and Planetary Science Letters, 415*, 16-24. doi:

Bürgmann, R. (2005). Interseismic coupling and asperity distribution along the Kamchatka subduction zone. *Journal of Geophysical Research, 110*(B7), B07405. doi: 10.1029/2005jb003648

Chen, Q., Freymueller, J. T., Yang, Z., Xu, C., Jiang, W., Wang, Q., & Liu, J. (2004). Spatially variable extension in southern Tibet based on GPS measurements. *Journal of Geophysical Research: Solid Earth, 109*(B9), n/a-n/a. doi: 10.1029/2002jb002350

Day, A. J., Peirce, C., & Sinha, M. C. (2001). Three‐dimensional crustal structure and magma chamber geometry at the intermediate‐spreading, back‐arc Valu Fa Ridge, Lau Basin—results of a wide‐angle seismic tomographic inversion. *Geophysical Journal International, 146*(1), 31-52. doi: 10.1046/j.0956-540X.2001.01446.x

DENG, Q., ZHANG, P., RAN, Y., YANG, X., MIN, W., & CHU, Q. (2003). Basic characteristics of active tectonics of China. *Science in China Series D-Earth Sciences, 46*(4), 356-372. doi: 10.1360/03yd9032

Deng, Y., & Tesauro, M. (2016). Lithospheric strength variations in Mainland China: Tectonic implications. *Tectonics, 35*(10), 2313-2333. doi: 10.1002/2016tc004272

Devachandra, M., Kundu, B., Catherine, J., Kumar, A., & Gahalaut, V. K. (2014). Global Positioning System (GPS) Measurements of Crustal Deformation across the Frontal Eastern Himalayan Syntaxis and Seismic‐Hazard Assessment. *Bulletin of the Seismological Society of America, 104*(3), 1518-1524. doi: 10.1785/0120130290

Dziewonski, A. M., Chou, T. A., & Woodhouse, J. H. (2012). Determination of earthquake source parameters from waveform data for studies of global and regional seismicity. *Journal of Geophysical Research: Solid Earth, 86*(B4), 2825-2852. doi: 10.1029/JB086iB04p02825

Ekström, G., Nettles, M., & Dziewoński, A. M. (2012). The global CMT project 2004–2010: Centroid-moment tensors for 13,017 earthquakes. *Physics of the Earth and Planetary Interiors, 200-201*, 1-9. doi: 10.1016/j.pepi.2012.04.002

Franklin, J. N. (1970). Well-posed stochastic extensions of ill-posed linear problems. *Journal of Mathematical Analysis and Applications, 31*(3), 682-716. doi: 10.1016/0022-247X(70)90017-X

Gan, W., Zhang, P., Shen, Z.-K., Niu, Z., Wang, M., Wan, Y., et al. (2007). Present-day crustal motion within the Tibetan Plateau inferred from GPS measurements. *Journal of Geophysical Research, 112*(B8), B08416. doi: 10.1029/2005jb004120

Ge, W.-P., Molnar, P., Shen, Z.-K., & Li, Q. (2015). Present-day crustal thinning in the southern and northern Tibetan Plateau revealed by GPS measurements. *Geophysical Research Letters, 42*(13), 5227-5235. doi: 10.1002/2015gl064347

Ge, W.-P., Wang, M., Shen, Z. K., Yuan, D. Y., & Zheng, W. J. (2013). Intersiesmic kinematics and information patterns on the upper crust of Qaidan-Qilianshan block. *Chinese J. Geophys. (in Chinese), 56*(09), 2994-3010. doi: 10.6038/cjg20130913

Ge, W. P., Shen, Z. K., Molnar, P., Wang, M., Zhang, P. Z., & Yuan, D. Y. (2022). GPS Determined Asymmetric Deformation Across Central Altyn Tagh Fault Reveals Rheological Structure of Northern Tibet. *Journal of Geophysical Research: Solid Earth, 127*(9). doi: 10.1029/2022jb024216

Glahn, A., Granet, M., & Group, R. G. T. (1993). Southern Rhine Graben: small-wavelength tomographic study and implications for the dynamic evolution of the graben. *Geophysical Journal International, 113*(2), 399-418. doi: 10.1111/j.1365-246X.1993.tb00896.x

Graeber, F. M., Houseman, G. A., & Greenhalgh, S. A. (2002). Regional teleseismic tomography of the western Lachlan Orogen and the Newer Volcanic Province, southeast Australia. *Geophysical Journal International, 149*(2), 249-266. doi: 10.1111/j.1365-246X.1993.tb00896.x

Hao, M., Li, Y., & Zhuang, W. (2019). Crustal movement and strain distribution in East Asia revealed by GPS observations. *Scientific Reports, 9*(1), 16797. doi: 10.1038/s41598-019-53306-y

Hao, M., Wang, Q., Zhang, P., Li, Z., Li, Y., & Zhuang, W. (2021). “Frame Wobbling” Causing Crustal Deformation Around the Ordos Block. *Geophysical Research Letters, 48*(1). doi: 10.1029/2020gl091008

Hori, M., Kameda, T., & Kato, T. (2001). Application of the inversion method to a GPS network for estimating the stress increment in Japan. *Geophysical Journal International, 144*(3), 597-608. doi: 10.1046/j.1365-246x.2001.01337.x

Jiang, G., Hu, S., Shi, Y., Zhang, C., Wang, Z., & Hu, D. (2019). Terrestrial heat flow of continental China: Updated dataset and tectonic implications. *Tectonophysics, 753*, 36-48. doi: 10.1016/j.tecto.2019.01.006

Jiang, G., Xu, C., Wen, Y., Xu, X., Ding, K., & Wang, J. (2014). Contemporary tectonic stressing rates of major strike-slip faults in the Tibetan Plateau from GPS observations using Least-Squares Collocation. *Tectonophysics, 615-616*, 85-95. doi: 10.1016/j.tecto.2013.12.022

Jiang, Z.-S., & Liu, J.-N. (2010). The method for establishing strain field and velocity field of crustal movement using least squares collocation. *Chinese J. Geophys. (in Chinese), 53*(05), 1109+1116-1117. doi: doi.org/10.1002/cjg2.1507

Kong, F., Wu, J., Liu, K. H., & Gao, S. S. (2016). Crustal anisotropy and ductile flow beneath the eastern Tibetan Plateau and adjacent areas. *Earth and Planetary Science Letters, 442*, 72-79. doi:

Kreemer, C., Blewitt, G., & Klein, E. C. (2014). A geodetic plate motion and Global Strain Rate Model. *Geochemistry, Geophysics, Geosystems, 15*(10), 3849-3889. doi: 10.1002/2014gc005407

Lancaster, P., & Salakauskas, K. (1986). *Curve and Surface Fitting, an Introduction*: Academic Press.

Lanza, F., Thurber, C. H., Syracuse, E. M., Power, J. A., & Ghosh, A. (2020). Seismic tomography of compressional wave velocity and attenuation structure for Makushin Volcano, Alaska. *Journal of Volcanology and Geothermal Research, 393*, 106804. doi: 10.1016/j.jvolgeores.2020.106804

Leigh H. Royden, B. Clark Burchfiel, Robert W. King, Erchie Wang, Zhiliang Chen, Feng Shen, & Liu, Y. (1997). Surface Deformation and Lower Crustal Flow in Eastern Tibet. *Science, 276*. doi: 10.1126/science.276.5313.788

Li, H., Li, S., Song, X. D., Gong, M., Li, X., & Jia, J. (2012). Crustal and uppermost mantle velocity structure beneath northwestern China from seismic ambient noise tomography. *Geophysical Journal International, 188*(1), 131-143. doi: 10.1111/j.1365-246X.2011.05205.x

Li, J., Yao, Y., Li, R., Yusan, S., Li, G., Freymueller, J. T., & Wang, Q. (2022). Present‐Day Strike‐Slip Faulting and Thrusting of the Kepingtage Fold‐and‐Thrust Belt in Southern Tianshan: Constraints From GPS Observations. *Geophysical Research Letters, 49*(11). doi: 10.1029/2022gl099105

Li, K., Li, Y., Tapponnier, P., Xu, X., Li, D., & He, Z. (2021). Joint InSAR and Field Constraints on Faulting During the Mw 6.4, July 23, 2020, Nima/Rongma Earthquake in Central Tibet. *Journal of Geophysical Research: Solid Earth, 126*(9). doi: 10.1029/2021jb022212

Liang, S., Gan, W., Shen, C., Xiao, G., Liu, J., Chen, W., et al. (2013). Three‐dimensional velocity field of present‐day crustal motion of the Tibetan Plateau derived from GPS measurements. *Journal of Geophysical Research: Solid Earth, 118*(10), 5722-5732. doi: 10.1002/2013JB010503

Liang, X., Zhou, S., Chen, Y. J., Jin, G., Xiao, L., Liu, P., et al. (2008). Earthquake distribution in southern Tibet and its tectonic implications. *Journal of Geophysical Research: Solid Earth, 113*(B12). doi:

Liu, M., Yang, Y., Shen, Z., Wang, S., Wang, M., & Wan, Y. (2007). Active tectonics and intracontinental earthquakes in China: The kinematics and geodynamics. In *Continental Intraplate Earthquakes: Science, Hazard, and Policy Issues*.

Loveless, J. P., & Meade, B. J. (2010). Geodetic imaging of plate motions, slip rates, and partitioning of deformation in Japan. *Journal of Geophysical Research, 115*(B2), B02410. doi: 10.1029/2008jb006248

Loveless, J. P., & Meade, B. J. (2011). Partitioning of localized and diffuse deformation in the Tibetan Plateau from joint inversions of geologic and geodetic observations. *Earth and Planetary Science Letters, 303*(1-2), 11-24. doi: 10.1016/j.epsl.2010.12.014

Masson, F., Lehujeur, M., Ziegler, Y., & Doubre, C. (2014). Strain rate tensor in Iran from a new GPS velocity field. *Geophysical Journal International, 197*(1), 10-21. doi: 10.1093/gji/ggt509

Meade, B. J. (2007). Present-day kinematics at the India-Asia collision zone. *Geology, 35*(1). doi: 10.1130/g22924a.1

Métois, M., Socquet, A., & Vigny, C. (2012). Interseismic coupling, segmentation and mechanical behavior of the central Chile subduction zone. *Journal of Geophysical Research: Solid Earth, 117*(B3), B03406. doi: 10.1029/2011jb008736

Okazaki, T., Fukahata, Y., & Nishimura, T. (2021). Consistent estimation of strain-rate fields from GNSS velocity data using basis function expansion with ABIC. *Earth, Planets and Space, 73*(1). doi: 10.1186/s40623-021-01474-5

Pang, Y., Wu, Y., Li, Y., & Chen, C. (2023). The mechanism of the present-day crustal deformation in southeast Tibet: from numerical modelling and geodetic observations. *Geophysical Journal International, 235*(1), 12-23. doi: 10.1093/gji/ggad200

Qi, W., Xuejun, Q., Qigui, L., Freymueller, J., Shaomin, Y., Caijun, X., et al. (2011). Rupture of deep faults in the 2008 Wenchuan earthquake and uplift of the Longmen Shan. *Nature Geoscience, 4*(9), 634-640. doi: 10.1038/ngeo1210

Qu, W., Lu, Z., Zhang, Q., Wang, Q., Hao, M., Zhu, W., & Qu, F. (2018). Crustal deformation and strain fields of the Weihe Basin and surrounding area of central China based on GPS observations and kinematic models. *Journal of Geodynamics, 120*, 1-10. doi: 10.1016/j.jog.2018.06.003

Rawlinson, N., Salmon, M., & Kennett, B. L. (2014). Transportable seismic array tomography in southeast Australia: Illuminating the transition from Proterozoic to Phanerozoic lithosphere. *Lithos, 189*, 65-76. doi: 10.1016/j.lithos.2013.06.001

Rui, X., & Stamps, D. S. (2019). A Geodetic Strain Rate and Tectonic Velocity Model for China. *Geochemistry, Geophysics, Geosystems, 20*(3), 1280-1297. doi: 10.1029/2018gc007806

Savage, J. C., Gan, W., & Svarc, J. L. (2001). Strain accumulation and rotation in the Eastern California Shear Zone. *Journal of Geophysical Research: Solid Earth, 106*(B10), 21995-22007. doi: 10.1029/2000jb000127

She, Y., & Fu, G. (2020). Uplift Mechanism of the Highest Mountains at Eastern Himalayan Syntaxis Revealed by In Situ Dense Gravimetry. *Geophysical Research Letters, 47*(22). doi: 10.1029/2020gl091208

Shen, F., Wang, L., Barbot, S., & Xu, J. (2023). North China as a mechanical bridge linking Pacific subduction and extrusion of the Tibetan Plateau. *Earth and Planetary Science Letters, 622*. doi: 10.1016/j.epsl.2023.118407

Shen, Z.-K., Jackson, D. D., & Ge, B. X. (1996). Crustal deformation across and beyond the Los Angeles basin from geodetic measurements. *Journal of Geophysical Research: Solid Earth, 101*(B12), 27957-27980. doi: 10.1029/96jb02544

Shen, Z.-K., Sun, J., Zhang, P., Wan, Y., Wang, M., Bürgmann, R., et al. (2009). Slip maxima at fault junctions and rupturing of barriers during the 2008 Wenchuan earthquake. *Nature Geoscience, 2*(10), 718-724. doi: 10.1038/ngeo636

Shen, Z.-K., Wang, M., Li, Y., Jackson, D. D., Yin, A., Dong, D., & Fang, P. (2001). Crustal deformation along the Altyn Tagh fault system, western China, from GPS. *Journal of Geophysical Research: Solid Earth, 106*(B12), 30607-30621. doi: 10.1029/2001JB000349

Shen, Z.-K., Wang, M., Zeng, Y., & Wang, F. (2015). Optimal Interpolation of Spatially Discretized Geodetic Data. *Bulletin of the Seismological Society of America, 105*(4), 2117-2127. doi: 10.1785/0120140247

Su, X.-N., Meng, G.-J., & Wang, Z. (2016). Methodology and application of GPS strain field estimation based on multi-scaler spherical wavelet. *Chinese J. Geophys. (in Chinese), 59*(05), 1585-1595. doi: 10.6038/cjg20160504

Tape, C., Musé, P., Simons, M., Dong, D., & Webb, F. (2009). Multiscale estimation of GPS velocity fields. *Geophysical Journal International, 179*(2), 945-971. doi: 10.1111/j.1365-246X.2009.04337.x

Thatcher, W. (2007). Microplate model for the present-day deformation of Tibet. *Journal of Geophysical Research, 112*(B1). doi: 10.1029/2005jb004244

Walck, M. C., & Clayton, R. W. (1987). P wave velocity variations in the Coso region, California, derived from local earthquake travel times. *Journal of Geophysical Research: Solid Earth, 92*(B1), 393-405. doi: 10.1029/JB092iB01p00393

Wang, H., Liu, M., Cao, J., Shen, X., & Zhang, G. (2011). Slip rates and seismic moment deficits on major active faults in mainland China. *Journal of Geophysical Research, 116*(B2), B02405. doi: 10.1029/2010jb007821

Wang, M., & Shen, Z. K. (2020). Present - Day Crustal Deformation of Continental China Derived From GPS and Its Tectonic Implications. *Journal of Geophysical Research: Solid Earth, 125*(2), e2019JB018774. doi: 10.1029/2019jb018774

Wang, Q., Zhang, P.-Z., Freymueller, J. T., Bilham, R., Larson, K. M., Lai, X. a., et al. (2001). Present-Day Crustal Deformation in China Constrained by Global Positioning System Measurements. *Science, 294*(5542), 574-577. doi: 10.1126/science.106364

Wang, W., Qiao, X., Yang, S., & Wang, D. (2017). Present-day velocity field and block kinematics of Tibetan Plateau from GPS measurements. *Geophysical Journal International, 208*(2), 1088-1102. doi: 10.1093/gji/ggw445

Wang, W., Zhao, B., Qiao, X., & Ding, K. (2022). Block Kinematics in North China From GPS Measurements. *Geochemistry, Geophysics, Geosystems, 23*(3). doi: 10.1029/2021gc010216

Wang, Y., Deng, Y., Shi, F., & Peng, Z. (2020). The Indo–Eurasia convergent margin and earthquakes in and around Tibetan Plateau. *Journal of Mineralogical and Petrological Sciences, 115*(2), 118-137. doi:

Wang, Z., & Dahlen, F. (1995). Spherical - spline parameterization of three - dimensional Earth models. *Geophysical Research Letters, 22*(22), 3099-3102. doi: 10.1029/95GL03080

Wang, Z., Tromp, J., & Ekström, G. (1998). Global and regional surface-wave inversions: A spherical-spline parameterization. *Geophysical Research Letters, 25*(2), 207-210. doi: 10.1029/97gl03634

Wei, S., Chen, Y. J., Sandvol, E., Zhou, S., Yue, H., Jin, G., et al. (2010). Regional earthquakes in northern Tibetan Plateau: Implications for lithospheric strength in Tibet. *Geophysical Research Letters, 37*(19). doi:

Wei, W., Dijin, W., Bin, Z., Yong, H., Caihong, Z., Kai, T., & Shaomin, Y. (2014). Horizontal crustal deformation in Chinese Mainland analyzed by CMONOC GPS data from 2009–2013. *Geodesy and Geodynamics, 5*(3), 41-45. doi: 10.3724/SP.J.1246.2014.03041

Wieczorek, M. A., & Meschede, M. (2018). SHTools: Tools for Working with Spherical Harmonics. *Geochemistry, Geophysics, Geosystems, 19*(8), 2574-2592. doi: 10.1029/2018gc007529

Wiggins, R. A. (1972). The general linear inverse problem: Implication of surface waves and free oscillations for earth structure. *Reviews of Geophysics, 10*(1), 251-285. doi: 10.1029/RG010i001p00251

Wu, Y., Jiang, Z.-S., Yang, G.-h., Fang, Y., & Wang, W.-X. (2009). The Method of GPS Strain Calculation in Whole Mode Using Least Square Collocation on Sphere Surface and Its Application. *Chinese J. Geophys. (in Chinese), 52*(07), 1707-1714. doi: 10.1002/cjg2.1398

Wu, Y., Jiang, Z., Yang, G., Wei, W., & Liu, X. (2011). Comparison of GPS strain rate computing methods and their reliability. *Geophysical Journal International, 185*(2), 703-717. doi: 10.1111/j.1365-246X.2011.04976.x

Xiong, Z., Zhuang, J., Zhou, S., Matsu'ura, M., Hao, M., & Wang, Q. (2021). Crustal strain-rate fields estimated from GNSS data with a Bayesian approach and its correlation to seismic activity in Mainland China. *Tectonophysics, 815*. doi: 10.1016/j.tecto.2021.229003

Xu, X., X.-Y.Wu, Yu, G., Tan, X., & Li, K. (2017). Seismo-geological signatures for identifying M⩾7.0 earthquake risk areas and their premilimary application in mainland China. *seismology and geology, 39*(02), 219-275. doi: 10.3969/j.issn.0253-4967.2017.02

Yang, Q.-Y., Santosh, M., & Dong, G. (2014). Late Palaeoproterozoic post-collisional magmatism in the North China Craton: geochemistry, zircon U–Pb geochronology, and Hf isotope of the pyroxenite–gabbro–diorite suite from Xinghe, Inner Mongolia. *International Geology Review, 56*(8), 959-984. doi: 10.1080/00206814.2014.908421

Yin, A. (2010). Cenozoic tectonic evolution of Asia: A preliminary synthesis. *Tectonophysics, 488*(1-4), 293-325. doi: 10.1016/j.tecto.2009.06.002

Yin, A., & Harrison, T. M. (2000). Geologic evolution of the Himalayan-Tibetan orogen. *Annual Review of Earth and Planetary Sciences, 28*(1), 211-280. doi: 10.1146/annurev.earth.28.1.211

Yin, A., Yu, X., Shen, Z.-K., & Liu-Zeng, J. (2015). A possible seismic gap and high earthquake hazard in the North China Basin. *Geology, 43*(1), 19-22. doi: 10.1130/g35986.1

Yu, J., Tan, K., Zhang, C., Zhao, B., Wang, D., & Li, Q. (2019). Present-day crustal movement of the Chinese mainland based on Global Navigation Satellite System data from 1998 to 2018. *Advances in Space Research, 63*(2), 840-856. doi: 10.1016/j.asr.2018.10.001

Yu, Y., & Chen, Y. J. (2016). Seismic anisotropy beneath the southern Ordos block and the Qinling-Dabie orogen, China: Eastward Tibetan asthenospheric flow around the southern Ordos. *Earth and Planetary Science Letters, 455*, 1-6. doi: 10.1016/j.epsl.2016.08.026

Zhang, F., Wu, Q., Li, Y., Zhang, R., Sun, L., Pan, J., & Ding, Z. (2018). Seismic Tomography of Eastern Tibet: Implications for the Tibetan Plateau Growth. *Tectonics, 37*(9), 2833-2847. doi: 10.1029/2018tc004977

Zhang, P.-Z. (2013). A review on active tectonics and deep crustal processes of the Western Sichuan region, eastern margin of the Tibetan Plateau. *Tectonophysics, 584*, 7-22. doi: 10.1016/j.tecto.2012.02.021

Zhang, P.-Z., Shen, Z., Wang, M., Gan, W., Bürgmann, R., Molnar, P., et al. (2004). Continuous deformation of the Tibetan Plateau from global positioning system data. *Geology, 32*(9), 809-812. doi: 10.1130/G20554.1

Zhang, Z., Yao, H., & Yang, Y. (2020). Shear wave velocity structure of the crust and upper mantle in Southeastern Tibet and its geodynamic implications. *Science China Earth Sciences, 63*, 1278-1293. doi:

Zhao, D., Qu, C., Shan, X., Gong, W., Zhang, Y., & Zhang, G. (2018). InSAR and GPS derived coseismic deformation and fault model of the 2017 Ms7. 0 Jiuzhaigou earthquake in the Northeast Bayanhar block. *Tectonophysics, 726*, 86-99. doi:

Zhao, G., Unsworth, M. J., Zhan, Y., Wang, L., Chen, X., Jones, A. G., et al. (2012). Crustal structure and rheology of the Longmenshan and Wenchuan Mw 7.9 earthquake epicentral area from magnetotelluric data. *Geology, 40*(12), 1139-1142. doi:

Zhao, J., Yuan, Z., Ren, J., Jiang, Z., Yao, Q., Zhou, Z., et al. (2022). Acceleration of Deep Slip Along the Longmenshan Fault Plane Before the 2008 M8.0 Wenchuan Earthquake. *Frontiers in Earth Science, 10*. doi: 10.3389/feart.2022.830317

Zheng, G., Wang, H., Wright, T. J., Lou, Y., Zhang, R., Zhang, W., et al. (2017). Crustal Deformation in the India-Eurasia Collision Zone From 25 Years of GPS Measurements. *Journal of Geophysical Research: Solid Earth, 122*(11), 9290-9312. doi: 10.1002/2017jb014465

Zheng, T., Ding, Z., Ning, J., Chang, L., Wang, X., Kong, F., et al. (2018). Crustal azimuthal anisotropy beneath the southeastern Tibetan Plateau and its geodynamic implications. *Journal of Geophysical Research: Solid Earth, 123*(11), 9733-9749. doi:

Zheng, Y.-F., Xiao, W.-J., & Zhao, G. (2013). Introduction to tectonics of China. *Gondwana Research, 23*(4), 1189-1206. doi: 10.1016/j.gr.2012.10.001

Zhu, S., Chen, J., & Shi, Y. (2022). Earthquake potential in the peripheral zones of the Ordos Block based on contemporary GPS strain rates and seismicity. *Tectonophysics, 824*. doi: 10.1016/j.tecto.2022.229224

Zhu, S., & Shi, Y. (2011). Estimation of GPS strain rate and its error analysis in the Chinese continent. *Journal of Asian Earth Sciences, 40*(1), 351-362. doi: 10.1016/j.jseaes.2010.06.007

Reconciling High-resolution Strain Rate of Continental China from GNSS Data with the Spherical Spline Interpolation

Zhengfeng Zhang[1], Huai Zhang[1,2,3] and Yaolin Shi[1]

[1]Key Laboratory of Computational Geodynamics of Chinese Academy of Sciences, College of Earth and Planetary Science, University of Chinese Academy of Sciences, Beijing 100049, China.

[2]Southern Marine Science and Engineering Guangdong Laboratory (Zhuhai), Zhuhai 519080, China.

[3]Beijing Yanshan Earth Critical Zone National Research Station, University of Chinese Academy of Sciences, Beijing 101408, China.

Corresponding author: Huai Zhang (hzhang@ucas.ac.cn)

Key Points:

- The multiple-scale spherical spline and detection model based on the latest GNSS data of continental China is proposed
- Revised high-resolution strain rate reveals new deformation features in continental China and local regions
- High-resolution strain rates exhibit excellent correlation with seismic activities and their focal mechanisms along major fault zones

Abstract

In this work, we propose a new generation of high-resolution strain rate model of present-day continental China from up-to-date GNSS observation data of 3571 stations. To reconcile the sparsely distributed GNSS (Global Navigation Satellite System) velocity data into an integrated vastly regional spherical coordinate frame, a novel interpolation method, namely the spherical spline method, is introduced as well. It can simultaneously calculate the strain rate with an ideal order of continuity while preserving the discontinuity from tectonically active major fault zones or deforming blocks. We take advantage of a set of inspection standards to assess the validity and resolution of our proposed model. The spherical spline method is deliberately examined and justified to fit the GNSS velocity data to illustrate inspection standards. Moreover, we construct a spherical harmony model for the resolution test. By the test criteria, the spherical spline method can reproduce the velocity and strain rate field at substantial order, suggesting that our method has high applicability and resolution in estimating strain rate in active tectonic regions or even global models. Finally, using the spherical spline method, we used measured GNSS velocity data to calculate the strain rate field in continental China. We also analyze the correlation between the seismic mechanism and the strain rate field of earthquakes, exhibiting that our proposed high-resolution strain rate model has great potential in explaining the deformation or evolution models of continental China.

Plain Language Summary

Continental China is characterized by Cenozoic active tectonics and intensive earthquakes widely distributed along major fault zones. Therefore, a high-resolution rate model based on the latest GNSS observation is of great importance in explaining such phenomena. This work introduces a novel multiscale spherical spline method that can adapt to discrete data at medium and high latitudes to remove the distortions caused by the conventional method in the Cartesian coordinate system. The rigid-body rotation and spherical harmonic checkerboard detection are utilized to validate the feasibility and resolution of the approach. GNSS data are collected from the most recent studies to estimate the high-resolution strain rate of continental China. Meanwhile, we analyze the correlation between strain rate and focal mechanisms and interpret the deformation and seismicity in continental China.

1 Introduction

Using GNSS velocity data estimating strain rate field has been studied for a long time (Hori et al., 2001; Savage et al., 2001; Shen et al., 2001). Even though the researchers use roughly the same data set, the results are not entirely consistent (Jiang & Liu, 2010; Rui & Stamps, 2019; Wang & Shen, 2020; Wu et al., 2009), which is mainly relative to their method. According to the distinction of using coordinates, estimating strain rate fields using GPS velocity data can be divided into Cartesian and spherical. Delaunay triangulation is always used in the Cartesian coordinate system because Delaunay triangulation in the sphere involves a highly complex algorithm and is time-consuming. This method has the advantage of being less computationally intensive but is error-sensitive and does not guarantee first-order continuity of the strain rate. As a common geostatistical method, Kriging interpolation can also fit strain rates using GNSS data (Zhu & Shi, 2011).

Nevertheless, Kriging interpolation does not consider the overall spatial correlation of the estimated values enough. It also requires high-quality data, and GNSS data are susceptible to various environmental factors and cannot meet the requirements. Numerous Cartesian coordinate methods always adopt the first-order Taylor series of the velocity field (Okazaki et al., 2021; Savage et al., 2001), then construct and solve the equations system to obtain strain rate. However, this practice is equivalent to linear interpolation, which decreases detail when GNSS stations are spares. Therefore, this method suits station-dense areas and large-scale surface deformation analysis. Some Cartesian coordinate methods can accurately fit the velocity values (Xiong et al., 2021), but because GNSS velocity data have large errors, over-fitting may cause distortions in the estimation results. Least-squares collocation and multi-surface function can be implemented in the Cartesian and spherical coordinate systems (Rui & Stamps, 2019; Shen et al., 2015; Wang & Shen, 2020; Wu et al., 2009). These two methods also do not guarantee the first-order smoothness of the strain rate. The higher-order continuity of the strain rate is critical for the equation of strain compatibility in the continuum mechanics, limiting the application of these methods. The Spherical wavelet and spherical harmonics are pure spherical coordinate algorithms. Moreover, spherical wavelet and spherical harmonics as pure spherical coordinate methods are like trigonometric functions, which might smooth out much detail of strain rate when GPS or GNSS stations are dense (Su et al., 2016; Wu et al., 2009). These methods will not be able to help analyze small-scale deformation and seismic mechanisms.

Continental China is a geologically active region with frequent earthquakes. Many researchers use GNSS velocity data and strain rate to study its continued deformation, active tectonics, and seismic activity. The Qinghai-Tibet Plateau region is one of the most tectonically active regions in the world, and its continuous deformation and its tectonic implications have always been of concern (Chen et al., 2004; Devachandra et al., 2014; Gan et al., 2007; Liang et al., 2013; Wang et al., 2017; Zhang et al., 2004). Due to the Qinghai-Tibetan plateau's implication, its surroundings are seismically active. Shen et al. (2009) and Qi et al. (2011) used GPS velocity data from the Longmen Mountain area to study active tectonics and seismic hazards in this area. Zhao et al. (2018) studied the tectonic influence and seismic mechanism of the 2017 Jiuzhaigou earthquake. (Shen et al., 2001) analyzed the deformation characteristic of the fault system in the western Tibetan Plateau. (Qu et al., 2018) studied the creeping nature of the crust in the Weihe Basin. In addition to the local region, the continuous deformation and seismicity of the Chinese mainland as a whole are also hot spots for researchers (Liu et al., 2007; Rui & Stamps, 2019; Wang et al., 2011; Wang & Shen, 2020; Wei et al., 2014; Xiong et al., 2021; Yu et al., 2019; Zheng et al., 2017). The continental China region straddles the mid and low latitudes. It is in a particular area of the Asia-European plate where active tectonics and seismic hazards are widely distributed. The compression of the Indian plate located at low latitudes also dramatically impacts the mid-latitude and eastern region of continental China. Therefore, it is necessary to develop a high spatial resolution and latitude-adaptation method to further study continental China’s strain rate field, seismic activity, and seismic mechanism. The multi-scale spherical spline method can automatically adapt to the inhomogeneous characteristics of the station distribution. Furthermore, it can ensure the smoothness of the strain rate as well as the discontinuous strain rate near the significant active tectonics. At the same time, the spherical spline method can ensure the second-order continuity of the velocity field, which can provide continuous boundary conditions for numerical simulations such as finite elements.

Solving an ill-posed equation is necessary to obtain the velocity or strain rate in the meshed grid regardless of the method used. Because of this problem's ill-posed nature, it can have multiple solutions or no solution. Using a smoothing tool can obtain a relatively reasonable solution but also introduces errors (Gan et al., 2007; Ge et al., 2013; Shen et al., 1996; Tape et al., 2009; Wu et al., 2011). Assessing effectiveness and resolution is always a significant issue for solving inverse problems. Scholars studying geophysical inverse problems realized the importance of method uncertainty and resolution in determining the solution (Backus, 1967, 1968, 1970; Franklin, 1970; Wiggins, 1972). Calculating strain rate using GPS or GNSS velocity is a typical ill-posed problem.

Many researchers currently use synthetic models to test their methods, but these models all have drawbacks. Some synthetic models can only be adapted to the distribution of stations in a specific study area and tectonic structures (Tape et al., 2009). Other methods are to fit a particular function and judge the merit of the method by the goodness of fit (Tape et al., 2009; Wu et al., 2011). However, the general function shows different values in the specific range, so these tests do not give a resolution of the different areas of the method, and the degree of fit is not easy to observe directly. Many scholars use statistical techniques to determine the accumulation of errors due to smoothings, such as calculating the variance or standard deviation (Jiang et al., 2014; Masson et al., 2014; Tape et al., 2009; Wu et al., 2009; Zhu & Shi, 2011). Nevertheless, the statistical parameters can only represent the overall error situation and do not provide good error discrimination for local areas. Therefore, building a universal set of standards to judge the uncertainty of calculating strain rate by using GNSS velocity data is essential.

The Cartesian coordinate methods still use geometric equations based on Cartesian coordinates to calculate strain rates. When researchers estimate the strain rate using Cartesian geometric equations in the sphere, the error can be ignored in low-latitude areas but can not be neglected in high-latitude study areas. It is also a problem with the Cartesian coordinate methods, so they are suitable for low-latitude areas but not high-latitude areas. In this paper, we use a rigid body rotation model to verify the superiority of the spherical coordinate method. Checkerboard test in seismic tomography is widely appreciated in geophysical inverse problem resolution tests (Day et al., 2001; Glahn et al., 1993; Graeber et al., 2002; Rawlinson et al., 2014; Walck & Clayton, 1987). The model consists of a regular grid of alternating positive and negative values, which can also be extended to three dimensions. The advantage of the checkerboard test is that it can detect the resolution and uncertainty of seismic wave inversion results visually and quickly. Because GNSS stations are limited and there are few sampling points in local areas, we imitate the checkerboard test using a spherical harmonic function to check the resolution of the strain rate calculation method. The spherical harmonic function is a continuous function that exhibits a regular lattice of positive and negative values under certain circumstances. We judge the method's merits by observing the degree of recovery of the spherical harmonic function by the inversion method. Using the spherical harmonic test model, we can also conclude that the spherical spline algorithm possesses high resolution.

In this article, we first introduce the spherical spline smoothing algorithm and method of calculating strain rate. Then, using the 3571 station sites of continental China and its surroundings from CMONOC I, CMONOC II, and the other sources, we establish a rotation of the rigid body and spherical harmonics models to examine the spherical spline smoothing algorithm. Finally, we calculate the strain rate field in continental China, analyze the correlation between the strain rate field and the earthquake source mechanism, and discuss the earthquake rate in continental China.

2 Seismic Activity and Tectonics Setting of Continental China

The seismic zone in continental China extends along active faults and orogenic zones and is very active (Wang et al., 2001; Yin, 2010). Figure 1 shows recent earthquake events and a significant tectonic setting in mainland China following Li et al. (2012), Xu et al. (2017), Yang et al. (2014), and Zhang (2013). The plate tectonics of continental China is complex. In general, it is divided into two major domains, east and west (i.e., Wang et al., 2011; Zheng et al., 2013), based on $105°E$ (i.e., Liu et al., 2007; Rui & Stamps, 2019). Eastern China mainly includes the NCB (Northeast China Block), the NCC (North China Craton), and the SCB (South China Block). Northeast China is part of the Eurasian plate, and the vast Songliao Basin is rich in oil and gas resources. At the same time, the Yilan-Yitong Fault and the Changbai Mountain Range are surrounded by frequent seismic activity. Separated from the Northeast Block by the ZBFZ (Zhangjiakou-Bohai Fault Zone), the NCC consists of the North China Plain, Ordos Block, and the SRZ (Shanxi Rift Zone) (Wang & Shen, 2020; Zheng et al., 2013). Their border zones are all very seismically active areas, and the Tangshan earthquake occurred at the intersection of the ZBFZ and the TLFZ (Tan-Lu Fault Zone). The SCB and the NCC are divided by the Qinling-Dabie Suture Zone. The SCB consists of the Yangzi Craton and the South China Fold Belt separated by the Jiao-Shao Fault (Zheng et al., 2013). This area is relatively stable and with few major earthquakes. Western China consists mainly of the Qinghai-Tibet Plateau and several important basins and blocks (i.e., Tarim, Qaidam, Junggar, and Alashan), which are divided by several large faults and orogen belts (i.e., West and East Kunlun Fault, ATF (Altyn Tagh Fault), Qilian-Haiyuan Fault, and South and North Tian Shan Orogen belt). Because the Qinghai-Tibet Plateau is directly extruded by the northeastern direction of the Indian Plate, its interior and the Himalayan Orogenic Belt at the boundary are highly seismic.

Moreover, the extrusion of the Qinghai-Tibet Plateau to the east collided with the South China block, causing frequent earthquakes in the Xianshuihe-Xiaojiang Fault and the Longmen Shan Fault, which are ones of the world's most active faults and where the Wenchuan earthquake occurred. The North and South Tianshan, orogenic belts above the northern part of the Tibetan Plateau, are also very involved in seismic activity because of the far-field effect of the Indian plate thrusting (Yin & Harrison, 2000). Seismicity in the eastern region is weaker than in the western part of China in terms of magnitude and frequency, and earthquakes in both western and eastern China are mainly concentrated at block boundaries and large active structures.

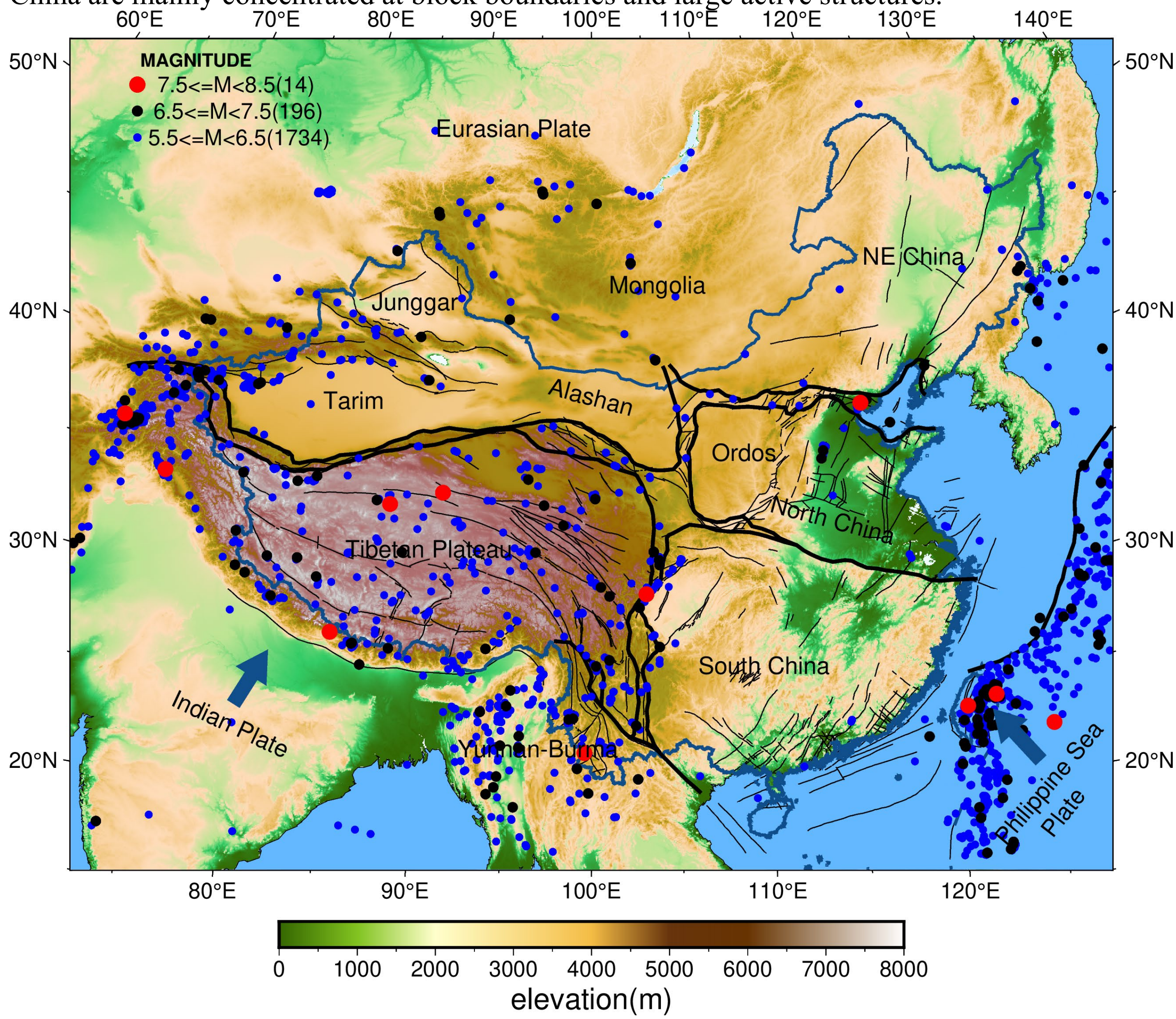

Figure 1. A simple tectonic unit and distribution of earthquake in continental China. The black lines are boundaries of blocks; the deep arrows donate the subduction direction of the Pacific plate

and the Indian Ocean plate; the color dots show seismic hazards with $M \geq 5.5$ from January 1, 1960, to December 31, 2021.

3 Spherical Spline Method

3.1 Gird Meshing and Choosing Scale Factor

Gird meshing in a sphere is always the research focus and previous steps of the interpolation algorithm of discrete data in the spherical surface. This study adopts the method of making spherical surface mesh high-resolution grids with spherical equilateral triangular (Wang & Dahlen, 1995; Wang et al., 1998), which has been used in many studies (Hao et al., 2019; Su et al., 2016; Tape et al., 2009). It is acknowledged that a spherical surface can not be arbitrarily divided into equilateral triangular being like a plane because a maximum of twenty spherical equilateral triangular can be divided on a spherical surface. We link the midpoints of an equilateral triangle to each other, which makes us obtain four equilateral triangles. Then, by repeating this operation, we can get high-resolution grids. We also link the trisection point, which can make us bring mesh of any density cooperating connecting the midpoint. We make a list of relationships with scale factor q (numbers of repeating), numbers of grids (Faces), and spatial support (average angular distance ($\overline{\Delta}$) and side arclength (l)).

Table 1. The relationship between scale factor and spatial scale.

Scale		**Spatial support**	
q	Faces	$\overline{\Delta}$	l
0	20	63.435°	$7053.64km$
1	80	31.718°	$3526.82km$
2	320	15.859°	$1763.41km$
3	1280	7.929°	$881.71.km$
4	5120	3.965°	$440.85km$
5	20480	1.982°	$220.43km$
6	81920	0.991°	$110.21km$
7	327680	0.496°	$55.11km$
8	1310720	0.248°	$27.55km$
9	5242880	0.124°	$13.78km$
10	20971520	0.062°	$6.78km$
11	83886080	0.031°	$3.44km$
12	335544320	0.016°	$1.72km$

We must choose a scale factor for ourselves using the spherical spline algorithm. In this study, we only discuss the scale factor of the station in mainland China and its surrounding regions, and Figure 2 shows the situation of grids meshing for q=12. We have observed that areas with q=9,10 are small, and q=11,12 is none. Finally, we chose q=10 meshing grids in our study. For other situations, the scale factor is selected from 7 to 9 and is not more than 12 (Tape et al., 2009).

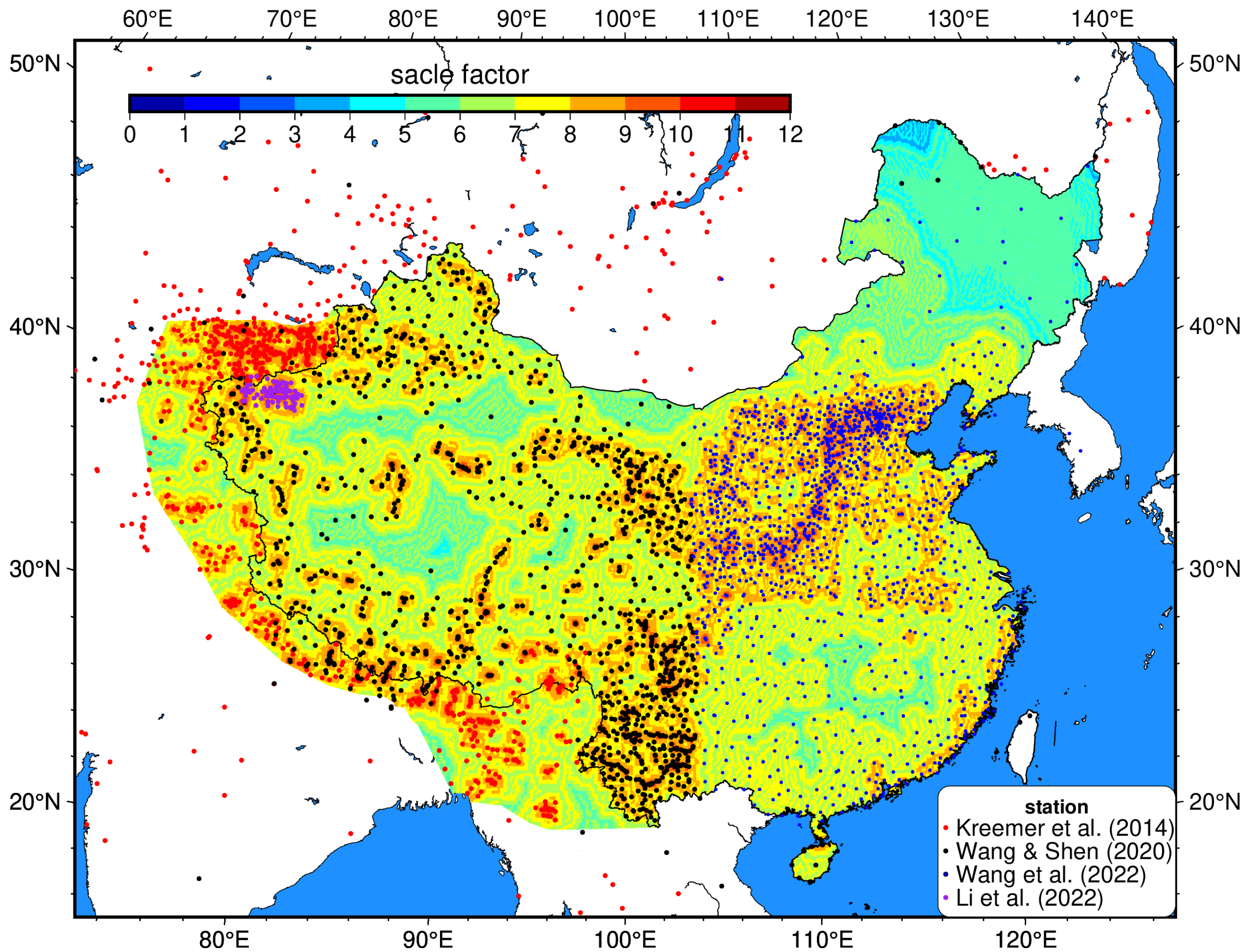

Figure 2. Station of mainland China and example of meshing scale using q=0-12. All station locations are from Wang & Shen (2020), Wang et al. (2022), and Li et al. (2022). The red dots denote GPS stations around continental China combined by Kreemer et al. (2014), which have been used by Wang & Shen (2020) in their research; The black dots represent the GPS station from Wang & Shen (2020); The deep blue dots represent the GPS station from Wang et al. (2022); The purple dots represent the GPS station from Li et al. (2022). Where stations are dense, the meshing of continental China with q=5-12 is available.

3.2 Basis Function of Spherical Spline

We utilize the GNSS station site to define the basic function of the spherical spline (Lancaster & Salakauskas, 1986).

$$f = \begin{cases} \frac{3}{4}\overline{\Delta}^{-3}\Delta^3 - \frac{6}{4}\overline{\Delta}^{-2}\Delta^2 + 1, & \Delta \le \overline{\Delta}, \\ -\frac{1}{4}\overline{\Delta}_1^3 + \frac{3}{4}\overline{\Delta}_1^2 - \frac{3}{4}\overline{\Delta}_1 + \frac{1}{4}, & \Delta \le \Delta \le 2\overline{\Delta} \end{cases} \tag{1}$$

where Δ is the angular distance between grid nodes with the station site, $\overline{\Delta} = \frac{\operatorname{acos}\left(\frac{\cos(72°)}{1-\cos(72°)}\right)}{2^q}$ is the angular distance of adjacent grid nodes and $\overline{\Delta}_1 = \frac{\overline{\Delta}-\Delta}{\overline{\Delta}}$. We define θ, φ as codimension and longitude of station sites and θ', φ' *as* codimension and longitude of grid nodes. According to spherical trigonometry, $\Delta = \mathrm{acos}[\cos\theta' \cos\theta + \sin\theta' \sin\theta \cos(\varphi' - \varphi)]$.

Function (2) and function (3) show the basic function of the spherical spline of the first derivative,

$$\begin{cases} \dfrac{\partial f}{\partial \theta} = \dfrac{1}{\bar{\Delta}}\left(\dfrac{9}{4}\bar{\Delta}^{-2}\Delta^2 - 3\bar{\Delta}\Delta\right)\dfrac{\partial \Delta}{\partial \theta} \\ \dfrac{\partial f}{\partial \varphi} = \dfrac{1}{\bar{\Delta}}\left(\dfrac{9}{4}\bar{\Delta}^{-2}\Delta^2 - 3\bar{\Delta}\Delta\right)\dfrac{\partial \Delta'}{\partial \varphi} \end{cases} \qquad 0 \le \Delta \le \bar{\Delta}, \tag{2}$$

$$\begin{cases} \dfrac{\partial f}{\partial \theta} = \dfrac{1}{\bar{\Delta}}\left(-\dfrac{3}{4}\bar{\Delta}_1^2 + \dfrac{3}{2}\bar{\Delta}_1 - \dfrac{3}{4}\right)\dfrac{\partial \Delta}{\partial \theta} \\ \dfrac{\partial f}{\partial \varphi} = \dfrac{1}{\bar{\Delta}}\left(-\dfrac{3}{4}\bar{\Delta}_1^2 + \dfrac{3}{2}\bar{\Delta}_1 - \dfrac{3}{4}\right)\dfrac{\partial \Delta'}{\partial \varphi} \end{cases} \qquad \bar{\Delta} \le \Delta \le \overline{2\Delta}. \tag{3}$$

When station sites and grid nodes are superposition ($\Delta = 0$), we use function (4) as the basic function.

$$f = 1 \qquad \frac{\partial f}{\partial \varphi} = 0 \qquad \frac{\partial f}{\partial \theta} = 0 \tag{4}$$

And when Δ is more than $2\overline{\Delta}$, we use function (5) as the basic function.

$$f = 0 \qquad \frac{\partial f}{\partial \varphi} = 0 \qquad \frac{\partial f}{\partial \theta} = 0 \tag{5}$$

3.3 Decomposition of the Velocity Field in Spherical Spline

The velocity field tangent to the sphere can be resolved as the sum of two vectors (function (6)),

$$v(\theta, \varphi) = v_\lambda(\theta, \varphi)\hat{\theta} + v_\varphi(\theta, \varphi)\hat{\varphi}, \tag{6}$$

where $\hat{\theta}$, $\hat{\varphi}$ are two unit vectors with south-north and east-west directions and θ, φ is codimension and longitudes of station sites. It is acknowledged that any scalar function $g \in L^2(S^2)$ can be written as the product of two vectors,

$$g(x, y) = \sum_{k=1}^{M} m_k g_k(x, y) = g_k^T(x, y) m. \tag{7}$$

Thus, function (6) can be rewritten as

$$v(\theta, \varphi) = \sum_{k=1}^{M} a_k f_k(\theta, \varphi)\,\hat{\theta} + \sum_{k=1}^{M} b_k f_k(\theta, \varphi)\,\hat{\varphi}. \tag{8}$$

Function (8) is discrete by observation sites (θ_i, φ_i), $i = 1, \dots\dots, N$, as

$$\begin{cases} v_\theta^i = \sum_{k=1}^{M} a_k f_k(\theta_i, \varphi_i) + n_\theta^i \\ v_\varphi^i = \sum_{k=1}^{M} b_k f_k(\theta_i, \varphi_i) + n_\varphi^i \end{cases}, \quad (9)$$

where v_θ^i, v_φ^i are the velocity of the solo station whose observation errors are denoted by n_θ^i, n_φ^i. Two equations of function (9) possess the same form; thus, estimation methods of a_k, b_k are also the same. We rewrite function (9) as matrix form,

$$\mathbf{d} = \mathbf{Fm} + \mathbf{n}, \quad (10)$$

where $\mathbf{d}$ is a column vector composed by v_θ^i or v_φ^i, $\mathbf{F}$ is a designed matrix composed of a quantity of spherical spline basis function, $\mathbf{m}$ is a column vector consisting of the model parameter, which is an unknown quantity to be solved, and $\mathbf{n}$ is a column vector composed of observation error. Function (10) is an ill-posed equation whose solution is not unique. Thus, we obtain model parameter $\mathbf{n}$ by least-squares functional,

$$G(\mathbf{m}) = \frac{1}{2}(\mathbf{Fm} - \mathbf{d})^T \mathbf{C}_D^{-1}(\mathbf{Fm} - \mathbf{d}) + \frac{1}{2}\lambda^2 \mathbf{m}^\mathbf{T}\mathbf{Sm}, \quad (11)$$

where λ controls the smoothness of the solution. Then we make $\frac{dG(\mathbf{m})}{d\mathbf{m}} = 0$ and get

$$\mathbf{m} = (\mathbf{F}^T \mathbf{C}_\mathbf{D}^{-1}\mathbf{F} + \lambda^2 \mathbf{S})^{-1}\mathbf{F}^T \mathbf{C}_\mathbf{D}^{-1}\mathbf{d}, \quad (12)$$

where $\mathbf{C_D}$ is east and north velocity correlation acquired on GPS velocity data files. Moreover, we select λ by ordinary cross-validation (Tape et al., 2009). In this section, we only introduce the fitting of the velocity field, but calculating the velocity gradient method is the same.

3.4 Calculating the Strian Field

Calculating the strain rate in our study looks like a three-dimensional spherical surface. Still, we do not obtain radial derivate of velocity component due to GPS or GNSS station observing only above the earth's surface. So, we do not discuss the radial strain rate on the spherical surface. Then it is related to v_φ, v_θ when calculating strain rate from the velocity field. The horizontal strain rate is the divergence and its transpose of GNSS velocities in the spherical coordinate system as

$$\begin{cases} \dot{\varepsilon}_\theta = \frac{1}{r}\frac{\partial v_\theta}{\partial \theta} \\ \dot{\varepsilon}_\varphi = \frac{1}{r sin\theta}\frac{\partial v_\varphi}{\partial \varphi} + \frac{v_\theta}{r} cot\theta \\ 2\dot{\varepsilon}_{\theta\varphi} = \frac{1}{r sin\theta}\frac{\partial v_\theta}{\partial \varphi} - \frac{v_\varphi}{r} cot\theta + \frac{1}{r}\frac{\partial v_\varphi}{\partial \theta} \\ 2\dot{\omega}_r = \frac{1}{r}\frac{\partial v_\varphi}{\partial \theta} + \frac{v_\varphi}{r} cot\,\theta - \frac{1}{r\,sin\,\theta}\frac{\partial v_\theta}{\partial \varphi} \end{cases}. \quad (13)$$

4 Detection Model

Because of the uneven distribution of stations, it is a significant issue how researchers estimate horizontal strain rates from these stations. Many adopt different methods to integrate and fit the velocity and strain rate fields, but they always obtain different results, even using the same data sets. Thus, judging a method's merits is a crucial assignment.

First, we present a rigid rotation model to illustrate that the spherical coordinate method is more suitable for calculations on the sphere. Generally, when calculating in the low latitude study area and small study area, the Cartesian method's result is almost identical to the spherical coordinate method. However, the Cartesian coordinate method cannot undertake this mission when the studied area is large-wide or high-latitude.

In addition, we present a spherical harmonics model. We use the spherical spline method to fit the spherical harmonic values generated by the latitude and longitude of each station and compare the results with the theoretical spherical harmonic values to determine the precision and resolution by analogy with the checkerboard test of seismic tomography (Bürgmann, 2005; Lanza et al., 2020; Loveless & Meade, 2010; Métois et al., 2012). It can help us visually judge the merits and effectiveness of the method in study areas.

4.1 Rigid Body Rotation

We assume continental China and its surrounding areas are located inside a rigid plate that only orbits a synthetic Euler polar with an angular velocity of $5 \times 10^{-8}\, rad/yr$. Then we calculate the linear velocity component v_θ (south-north direction), v_φ (east-west direction) of every station in our study areas. When a plate as a rigid body revolves, it has no deformation. The normal and shear strain rates are zero relative to the angular velocity. The rotation rate is not zero.

Function (14) is the relationship between v_θ, v_φ with latitude and longitude of the Euler polar.

$$\begin{cases} v_\theta = R\Omega\, sin(\varphi - \varphi')\sin\theta' \\ v_\varphi = R\Omega[\cos\varphi\cos\varphi'\cos\theta\cos\theta' - \cos\theta'\sin\theta + \cos\theta\sin\varphi\sin\varphi'\sin\theta'] \end{cases} . \tag{14}$$

According to functions (13-14), we have the rotation rate

$$\omega_{\theta\varphi} = -\frac{\Omega}{sin\theta}(sin\, sin\varphi' sin\theta' + cos\varphi cos\varphi' sin\theta' + cos\theta cos\theta' sin\theta - cos\varphi cos\varphi' \, cos^2\theta\, sin\theta' - cos^2\theta\, sin\varphi sin\varphi' sin\theta'), \tag{15}$$

where θ, φ denote codimension and latitude of GPS or GNSS stations, θ', φ' denote codimension and latitude of the polar axis, R is the radius of the earth, $6371km$ and Ω is angular velocity. Meanwhile, we also get a normal strain rate, and the shear strain rate is zero, which can illustrate that function (14) is correct. Then we input the velocity of stations into a spherical spline program to obtain fitting velocity and rotation rate compared with the theoretical results of the entire study area.

4.2 Spherical Harmonics

The spherical harmonics function is widely applied in the spherical coordinate system. In geophysical studies, we often take the earth as a research object. Because the earth's shape is approximately a sphere, its physics field possesses a spherical symmetric future. Thus, spherical harmonics are widely used in geodesy, meteorology, spherical finite element, and numerical simulation of geodynamics.

We use function (16) to build our spherical harmonics model,

$$Y_l^m(\theta,\varphi) = \sqrt{\frac{(2l+1)(l-m)!}{4\pi(l+m)!}}\, P_l^m(cos\theta)e^{im\varphi}, \qquad -l \le m \le l, \tag{16}$$

where l, m are the order and degree of spherical harmonics, i is the imaginary unit and $P_l^m(x)$ is Associated Legendre Polynomial and,

$$P_l^m(x) = (-1)^m(1-x^2)^{\frac{m}{2}}\frac{d^m}{dx^m}\big(P_l(x)\big).$$

$P_l(x)$ is Orthogonal Legendre polynomial,

$$P_l(x) = \frac{1}{2^l l!}\frac{d^l}{dx^l}(x^2-1)^l. \tag{17}$$

Due to the future of spherical harmonics, its distribution takes on transversal, longitudinal strips or spherical rectangles (Figure 3) when l, m take different numbers. We use the latitude and longitude of GNSS station sites to calculate spherical harmonics values ($Y_l^m(\theta,\varphi)$) of their site. Then, v_φ denote the real part of the values and v_θ denote the imaginary part of the values, which will be inputted into the spherical spline program to obtain fitting velocity and velocity gradient results. Meanwhile, to show the resolution of the method intuitively, we can calculate the longitudinal and latitudinal half-wavelength of spherical harmonics with l, m selected by us. Function (18) is the equation of calculating half-wavelength (Wieczorek & Meschede, 2018),

$$\begin{cases} \lambda_l = \dfrac{2\pi R}{\sqrt{l(l+1)}}, \\ \lambda_m = \dfrac{2\pi R\cos\theta}{l} \end{cases} \tag{18}$$

where λ_l, λ_m are meridional and zonal half-wavelength, θ is colatitude and R is the earth's radius, $6371km$.

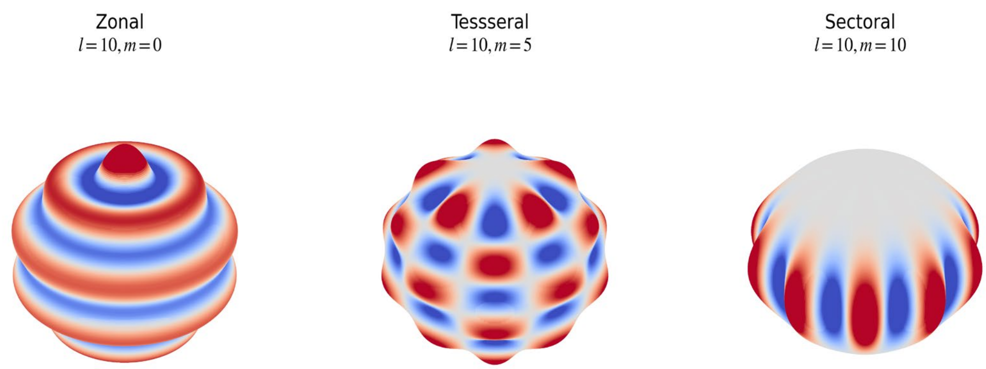

Figure 3. The shape of the strips or lattices produced by the spherical harmonic function on the sphere.

5 Data and Results

In Sections 5 and 6, the stations used by us are from three recent studies (Li et al., 2022; Wang & Shen, 2020; Wang et al., 2022). Wang & Shen (2020) supply complete GPS velocity data for continental China and its surroundings and this dataset has been adopted in many studies (Ge et al., 2022; Li et al., 2021; Pang et al., 2023; She & Fu, 2020; Wang et al., 2022; Zhu et al., 2022). The data set combines the CMONOC I, CMONOC II, and some regional densified stations in continental China, and their observations span from 1991 to 2016. In addition, he has assembled data from several other studies to compensate for the lack of data from surrounding continental China (Kreemer et al., 2014). We then use the North China dataset from Wang et al. (2022) to densify data in Ordos Block and replace the overlapping station portion between this dataset and the dataset from Wang & Shen (2020). The dataset used by Wang et al. (2022) came from Hao et al. (2021), and it multiplied the uncertainty by 3 to make the data fit the noise of the dataset from Wang & Shen (2020), to be able to use the two sets of data together. Finally, we processed the data set from (2022) using the method of Wang et al. (2022) to densify data in North and South TianShan and replace its overlapping parts between Li et al. (2022) and Wang & Shen (2020). Therefore, we finally assembled the data from 3715 stations in and around continental China and removed 144 groups of stations in which the relative error of one of the velocity components exceeded ten percent and the error of the velocity vector magnitude exceeded thirty percent. The 3571 stations we used are labeled in Figure 2.

5.1 Inspection Result of Rigid Body Rotation

Figure 4a shows the artificial linear velocity field (black arrow) of stations revolving around the Euler polar $(90°N, 105°E)$ and theoretical rotation rate (background) correlation with an angular velocity of $5 \times 10^{-8} rad/yr$. Figure 4b shows that the rotation rate calculated by using the spherical spline method is almost identical to the theoretical rotation rate; Figure 4c shows the absolute error of the theoretical and fitting rotation rates. We can observe that the relative error is not more than two thousandths where the difference is largest. In contrast, relative errors in the interior of continental China are mainly under one ten-thousandth. Other strain rate components are calculated by the spherical spline method shown in Figure S1, and their theoretical value is zero. The order of magnitude of the rotation rate is 10^{-8}. Whereas the order of magnitude of strain rate components in Figure S1 is 10^{-11}, and the largest errors are on the boundary. Thus, the result calculated by the spherical spline method can be better.

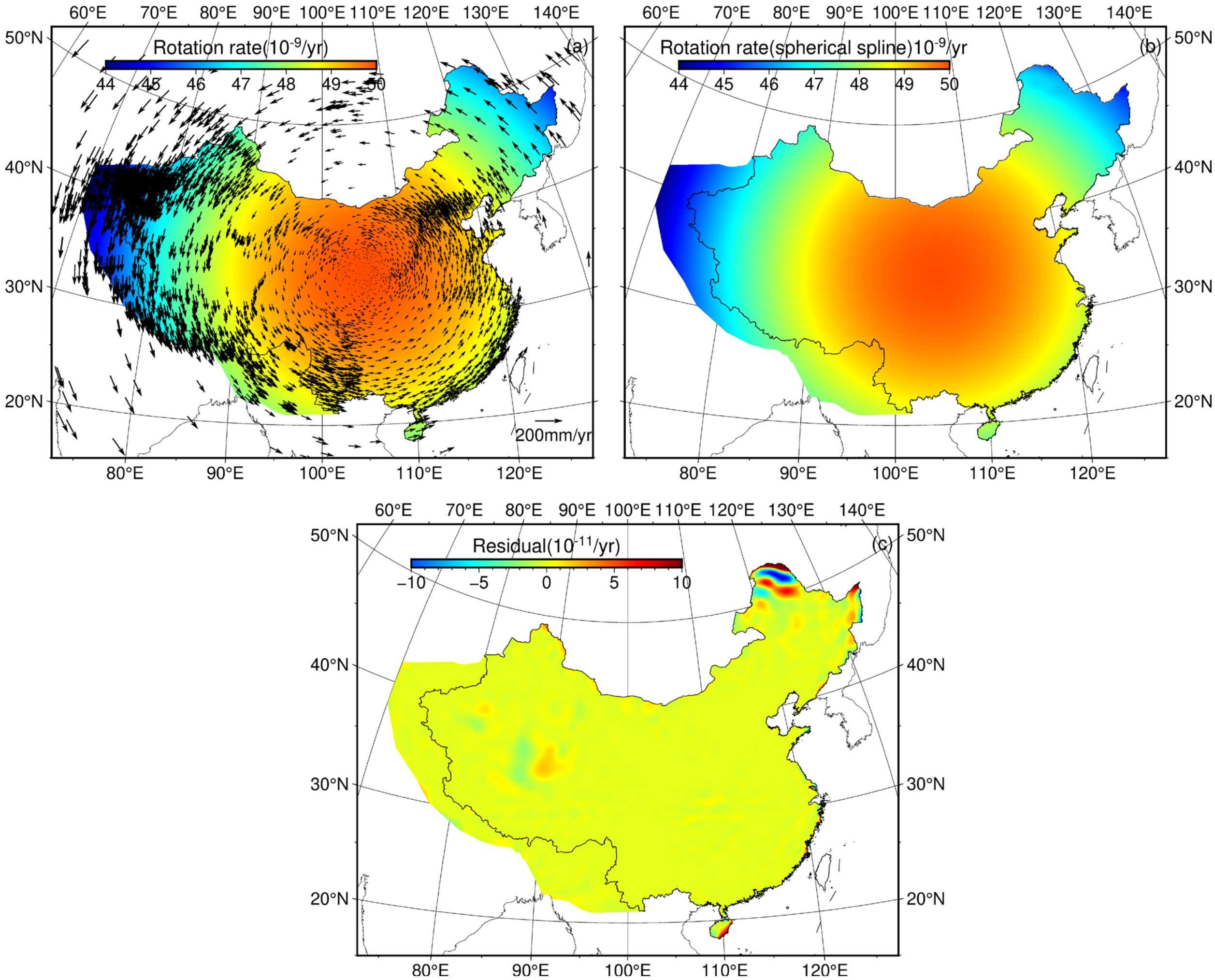

Figure 4. Theoretical result and estimated result of rotation rate. (a) Theoretical result of rotation rate and artificial velocity (black arrow). (b) result of the spherical spline. (c) absolute error (difference between theoretical results and estimated results).

Figure 5a shows the linear velocity field (black arrow) of stations revolving around the Euler polar $(35°N, 105°E)$ and theoretical rotation rate (background) with an angular velocity of $5 \times 10^{-8} rad/yr$; Figure 5b shows that the rotation rate calculated using the spherical spline method is almost identical to the theoretical rotation rate; Figure 5c shows the absolute error of the theoretical and fitting rotation rate. The result showed similar characteristics to Figure 4. Other strain rate components with zero theoretical results are shown in Figure S2, which also indicates similar futures to Figure S1.

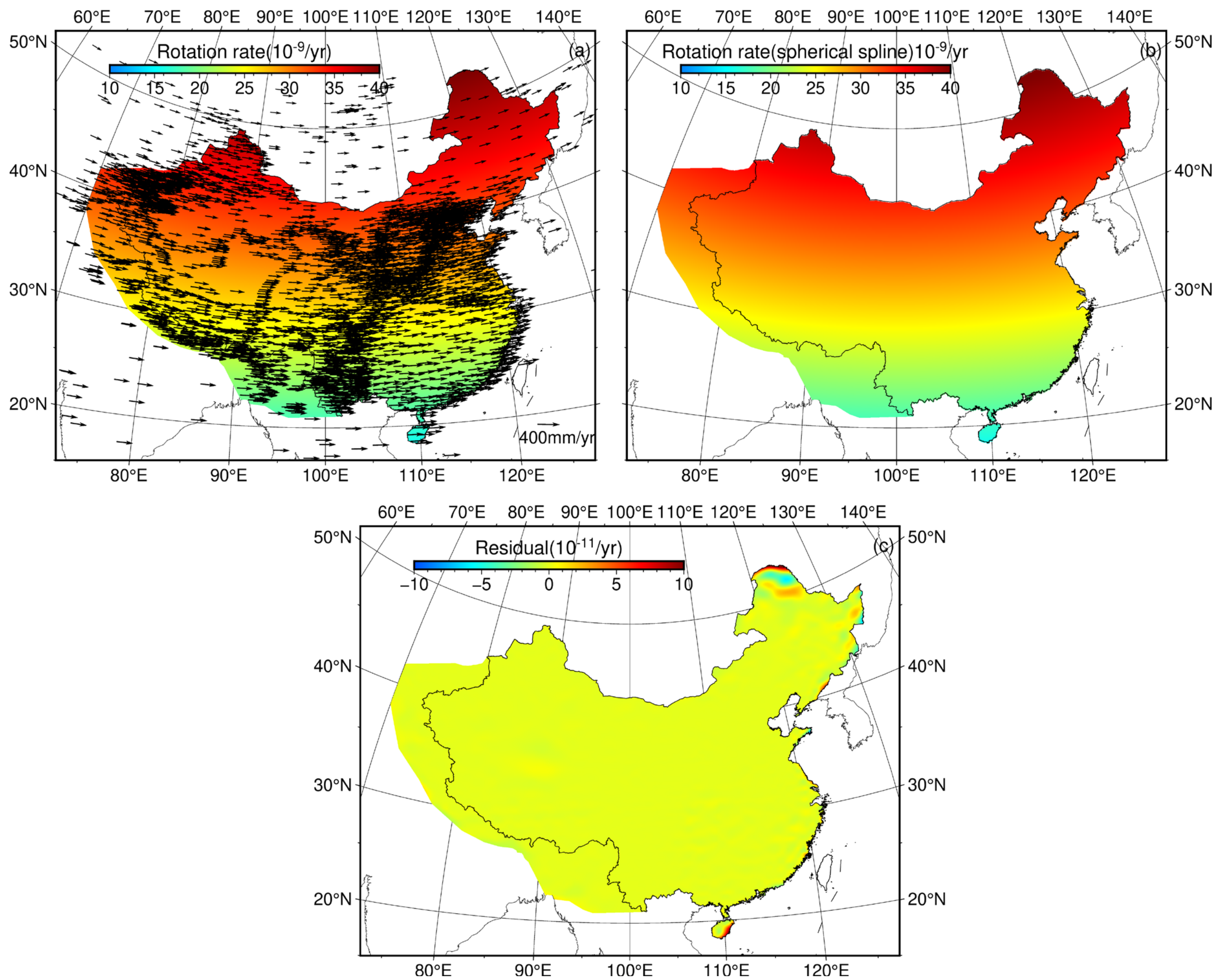

Figure 5. Theoretical result and estimated result of rotation rate. (a) Theoretical result of rotation rate and synthetic velocity (black arrow). (b) result of the spherical spline. (c) absolute error (difference between theoretical results and estimated results).

5.2 Inspection Result of Spherical Harmonics

Figure 6 shows the detection result of velocity. Figure 6a and 6c, respectively, show synthetic gridding v_θ and v_φ, which are imaginary parts and real parts of spherical harmonics with $l = 64, m = 32$. According to function (22), we can obtain that south-north direction half-wavelength λ_l is about $620km$, earth-west direction half-wavelength λ_m is about $567km$ at $25°N$ and earth-west direction half-wavelength λ_m is about $402km$ at $50°N$. Figure 5b and 6d, respectively. They exhibit a relationship between the fitting result of spherical spline and station density. We can observe that where stations are density and uniform, fitting results by spherical spline and theoretical v_θ, v_φ are consistent, and where there are no stations ($32°N$ to $37°N$, $81°E$ to $92°E$), the grids of spherical harmonics are blurred, but the shape is still visible.

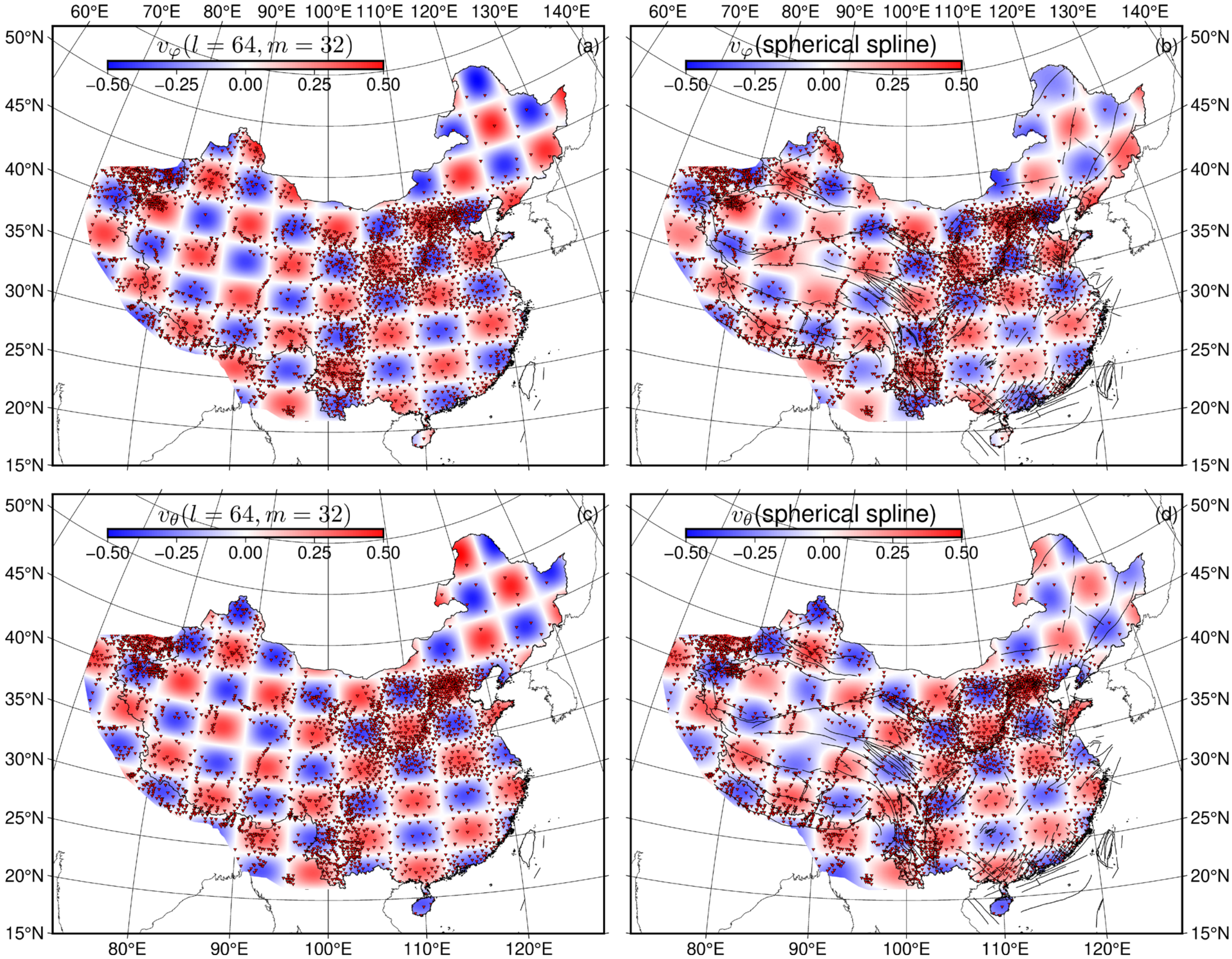

Figure 6. The spherical harmonics with $l = 64, m = 32$ and fitting results of the spherical spline. (a) v_φ calculated by spherical harmonics. (b) v_φ fitted by spherical spline. (c) v_θ calculated by spherical harmonics. (d) v_θ fitted by spherical spline. The rad inverted triangles are all stations of continental China and the surroundings from Figure 1, and the black lines on the background donate significant activity tectonics of continental China (same as Figure 6-9 and Figure S3-S8).

Figure 7 shows the detection result of the velocity gradient. Figure 7a and 7c, respectively. They illustrate synthetic gridding $\frac{dv_\varphi}{d\theta}, \frac{dv_\theta}{d\theta}$, which are south-north derivatives of the imaginary part and the real part of spherical harmonics with $l = 64, m = 32$. The result showed similar characteristics where stations are density and uniform, fitting the result by spherical spline and theoretical $\frac{dv_\varphi}{d\theta}, \frac{dv_\theta}{d\theta}$ are consistent, and where there are no stations ($32°N$ to $37°N$, $81°E$ to $92°E$), the grids of spherical harmonics are blurred, but the shape is still visible in Figure 7.

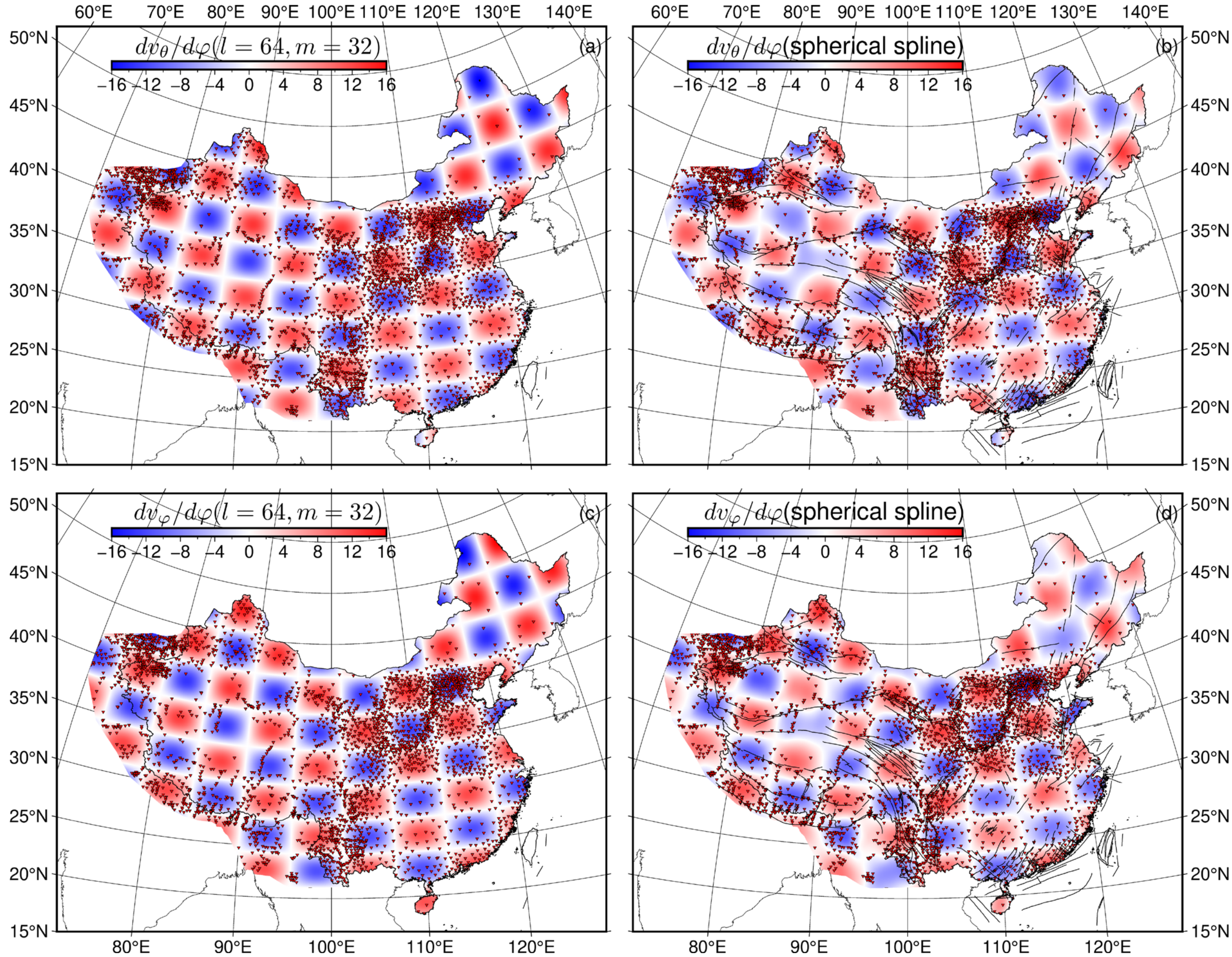

Figure 7. The latitude direction gradient of spherical harmonics with $l = 64, m = 32$ and fitting results of the spherical spline. (a) $\frac{dv_\varphi}{d\theta}$ calculated by spherical harmonics. (b) $\frac{dv_\varphi}{d\theta}$ fitted by spherical spline. (c) $\frac{dv_\theta}{d\theta}$ calculated by spherical harmonics. (d) $\frac{dv_\theta}{d\theta}$ fitted by spherical spline.

Figure 8 shows the detection result of velocity using spherical harmonics with $l = 96, m = 48$ to test minimum resolution because its south-north direction half-wavelength λ_l is about $400km$, earth-west direction half-wavelength λ_m is about $360km$ at $25°N$ and earth-west direction half-wavelength λ_m is about $260km$ at $50°N$. So, the purpose of this detection model is to confirm whether the spherical spline method processes the ability to distinguish the strain rate of minor structures (scale of about $300km$) in dense station areas such as the Pamir Plateau, Tianshan structure zone, Sichuan, Yunnan, Ordos block, North China seismic zone, and South China region. Figure 8a and 8c, respectively, show artificial gridding v_θ, v_φ , which are imaginary parts and real parts of spherical harmonics with $l = 96, m = 48$. Figure 8b and 8d, respectively. They show the relationship between the fitting result of spherical spline and station density.

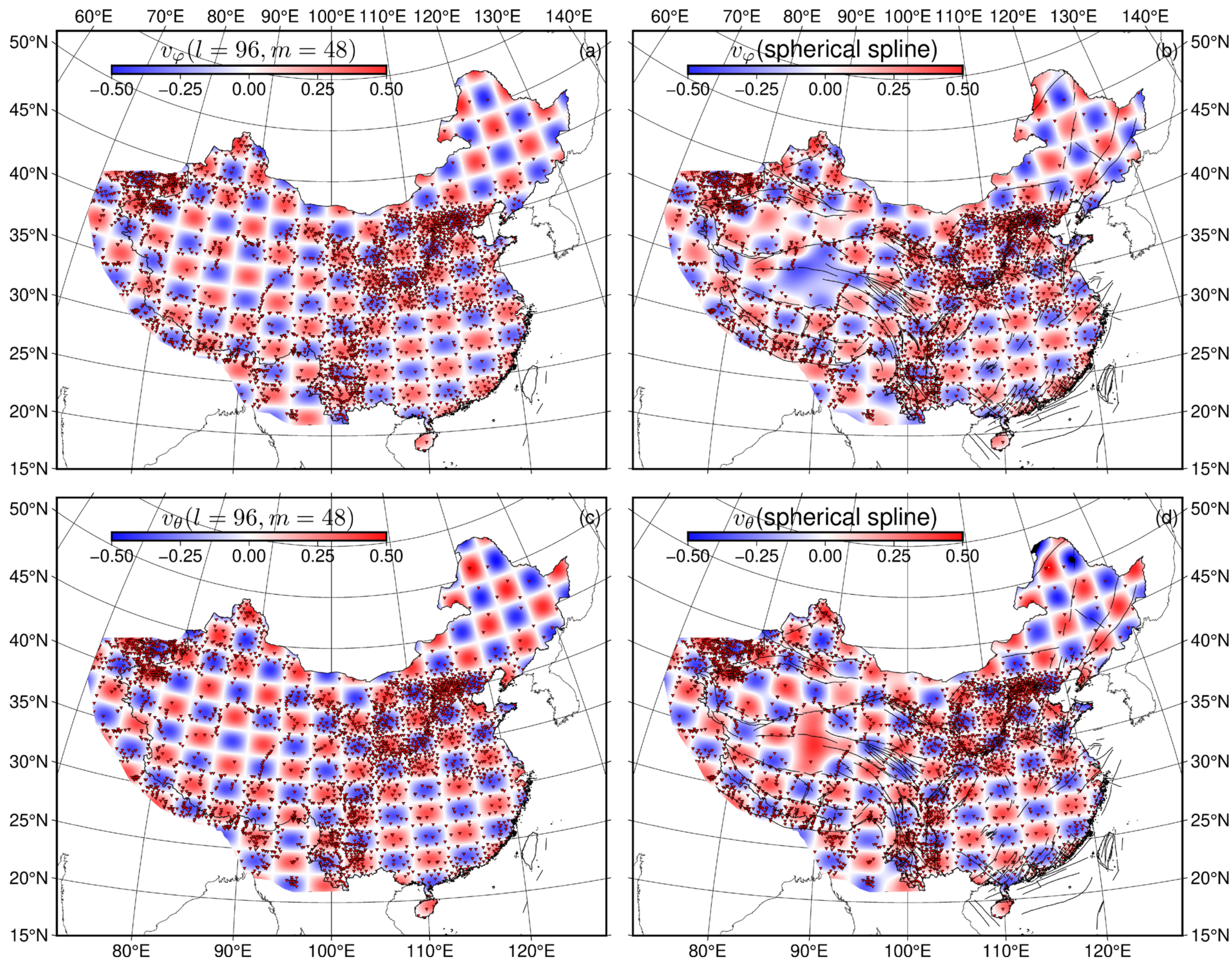

Figure 8. Spherical harmonics with $l = 98, m = 64$ and fitting results of the spherical spline. (a) v_φ calculated by the spherical harmonics function. (b) v_φ fitted by spherical spline. (c) v_θ calculated by spherical harmonics function; (b) v_θ fitted by spherical spline.

Figure 9 shows the fitting detection result of velocity. Figure 9a and 9c, respectively. They show synthetic gridding $\frac{dv_\varphi}{d\theta}, \frac{dv_\theta}{d\theta}$, which are south-north derivatives of the imaginary part and real part of spherical harmonics with $l = 96, m = 48$. The result showed similar characteristics where stations are density and uniform. Fitting the result by spherical spline and theoretical $\frac{dv_\varphi}{d\theta}, \frac{dv_\theta}{d\theta}$ are consistent with figure 9. The results of all strain rates are the sum of the multiples of velocity and velocity gradient. Their characteristics are like the above results. So, they are not shown in the main text but in Figure S3-S8.

From the results of the above two experiments, we can conclude that the spherical spline results we can still give confidence to the strain rate results calculated by the spherical spline of large structures over 600 km in areas where stations are sparse or even absent. Furthermore, in areas with dense or uniform stations, the spherical spline can also reveal the correspondence between structures and strain rates at scales below 300 km or even smaller.

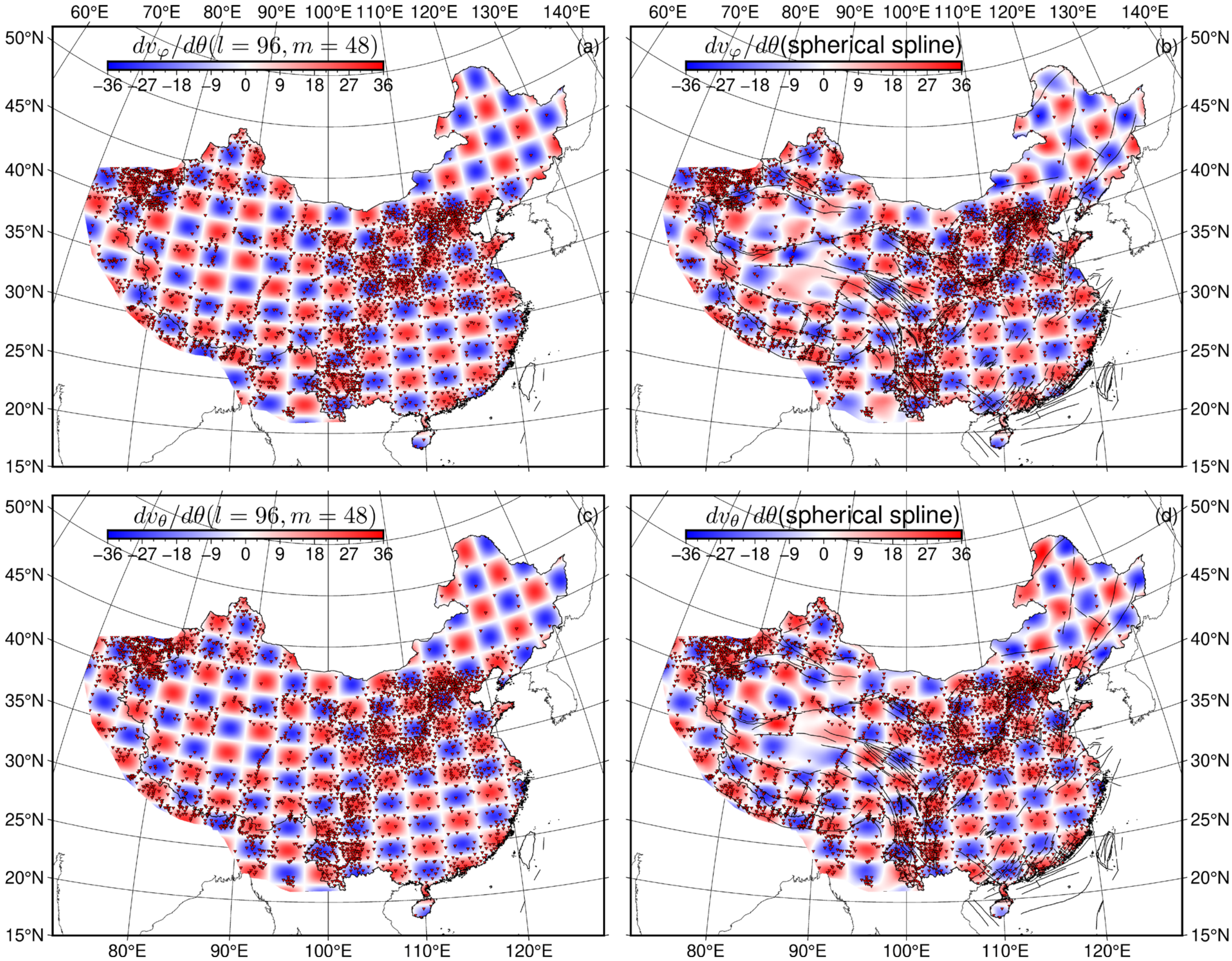

Figure 9. The Gradient of spherical harmonics with $l = 96, m = 48$ and fitting results of the spherical spline. (a) $\frac{dv_\varphi}{d\theta}$ calculated by spherical harmonics. (b) $\frac{dv_\varphi}{d\theta}$ fitted by spherical spline. (c) $\frac{dv_\theta}{d\theta}$ calculated by spherical harmonics. (d) $\frac{dv_\theta}{d\theta}$ fitted by spherical spline.

6 Seismic Mechanism and Strain Rate of Continental China

The Chinese mainland is an active geological tectonic area in a unique tectonic setting where the Eurasian Plate, Indian Plate, and Philippines Sea Plate meet in a triangular framework. As a result of the squeeze from India and the Philippine Sea Plate, earthquake in continental China is quite active. The M 7.8 earthquake in Tangshan in 1976 caused the death of 200,000 people; The M 8.1 earthquake in Hohxil in 2001 was the largest in China since 1960; The 2008 Wenchuan earthquake in Sichuan took nearly 70,000 lives and caused economic losses of almost 85 million RMB. Therefore, the study of seismic activity is of great importance to people's livelihoods and the economy. Studying the strain rate of the shallow ground is an essential reference for understanding the seismic mechanism.

The source of the GNSS velocity data we use is the same as in Section 4. In section 4, we only used the station locations.In contrast, in this section, we will use the measured GNSS velocity data to calculate the strain rate for continental China using the spherical spline method. Figure 10 shows the velocity vector of all stations in continental China and its surroundings. For the accuracy of the calculation results, we excluded the data where the relative error of velocity components exceeded 10% and the relative error of velocity vector size exceeded 30%.

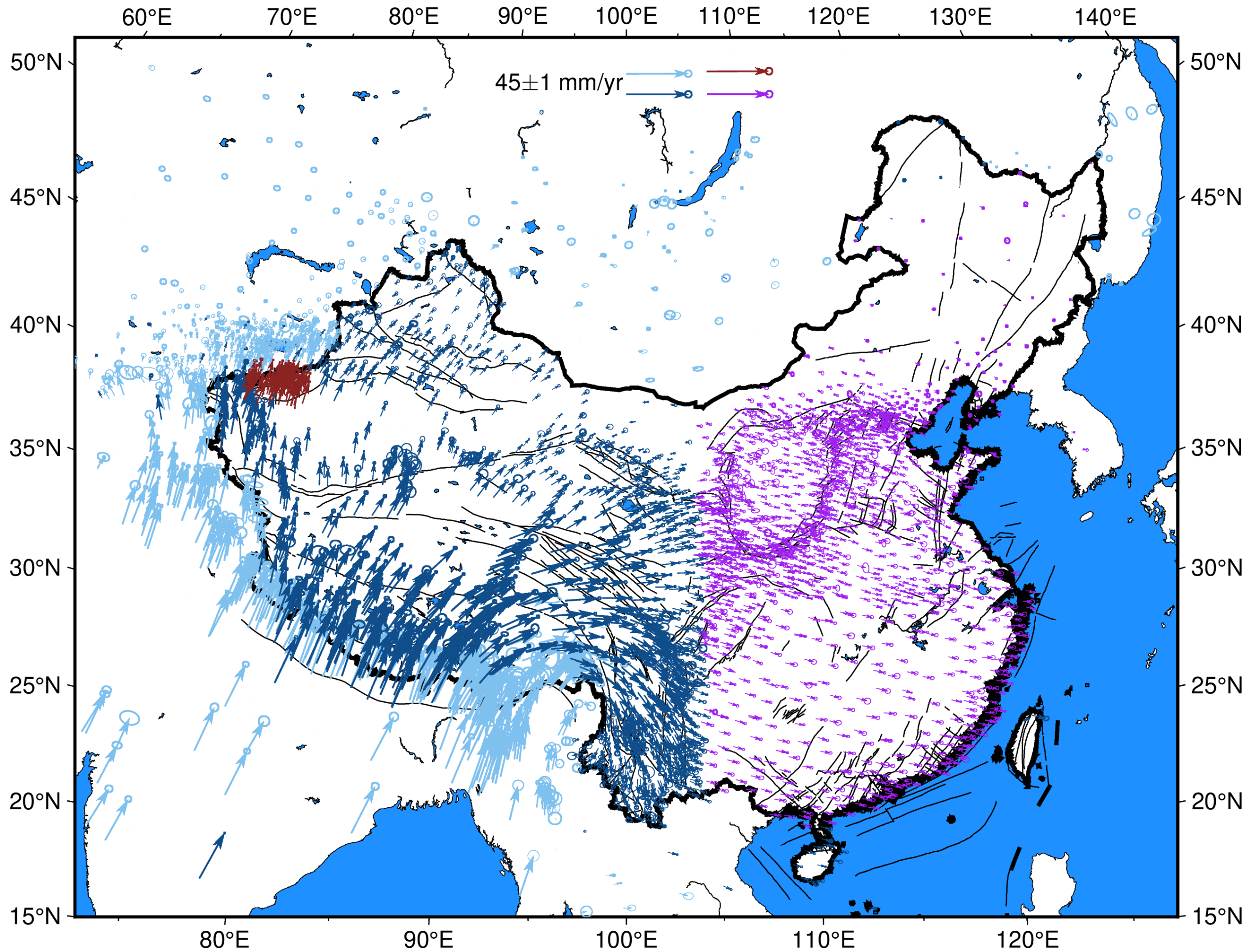

Figure 10. GNSS velocity. The deep blue arrows are from Wang & Shen (2020); the light blue arrows are from Kreemer et al. (2014); the brown arrows are from Li et al. (2022); the purple arrows are from Wang et al. (2022). Wang et al. (2022) processed Ordos data from Hao et al. (2021) so that it would agree with the reference system and noise level of Wang & Shen (2020). We processed data from Li et al. (2022) using the same methodology. All GNSS velocity is listed in Table S1.

The background of Figure 11 shows the dilatation of continental China, whose negative is extrusion and the positive is tension. Due to the north-eastward extrusion of the Indian plate, the largest strain on the Chinese mainland is in the subduction zone of the Himalayan Main Thrust, where the dilatation rate exceeds $-40 \times 10^{-9}/yr$. On the eastern side of the Himalayan Main Thrust, the dilatation rate reaches about $-80 \times 10^{-9}/yr$, caused by the lateral extrusion of the Tibetan plateau being blocked by the SCB (Leigh H. Royden et al., 1997; Zhang et al., 2018; Zhang et al., 2004). The deformation of the Gan-Yushu Fault, XSHF, the Xiangjiang River Fault, and the Red River Fault region in the junction of the Tibetan Plateau and the SCB is to the vertical direction of the extrusion overflow and greater than the extrusion, so these areas generally exhibit a tensile nature (Bai et al., 2010; Zhao et al., 2022). We believe that it is also due to the lateral extrusion of the Qinghai-Tibet Plateau caused by the South China plate blocking it from overflowing in the vertical direction. The seismic mechanism can also explain this in this area exhibiting strike-slip or normal fault. The interior of the Qinghai-Tibet Plateau may also be vertically overflowing when squeezed, so the overall deformation is in tension. At the same time, the seismic mechanism of this region can also indicate this. The northeastern and northern margin of the Qinghai-Tibet Plateau is influenced by the far plant of the Indian plate extrusion, so this area receives extrusion. Figure 11 demonstrates the extrusive nature of the fault system along the northern and northeastern margins of the Tibetan Plateau, and the dilatation rate in this area is between $-15 \times 10^{-9}/yr$ and $-20 \times 10^{-9}/yr$. Also affected by the compression of the Indian plate is the Tianshan orogenic belt, which has a dilatation rate of $-40 \times 10^{-9}/yr$ at the subduction front. At the same time, Figure 11 shows the extrusion strain zone in the eastward extension of North and South Tianshan with a dilatation rate of $-10 \times 10^{-9}/yr$. The seismogenic mechanisms of the northern and northeastern margins of the Qinghai-Tibet Plateau and the Tien Shan frontal margin have been dominated by thrust faulting consistent with the dilatation rate results. And the greater the magnitude of the dilatation rate, the more frequent the earthquakes. Seismic activity and mechanism of western China are correlated with the dilatation rate. Reverse-fault earthquakes frequently occur in regions with negative dilatation rates, and normal-fault or strike-slip earthquakes occur in areas with positive dilatation rates. Although fewer large earthquakes exist in Eastern China, the dilatation results also show this pattern. The Longmenshan Fault, located at the junction of East and West China, is considerably squeezed, and t reverse-fault earthquakes dominate the frequency of earthquakes in this area. However, positive fault earthquakes dominate the East Kunlun F., Ganzi-Yushu F., and Jiali F. to the west. Figure 11 dilatation rate results clearly show this pattern, indicating that our dilatation rate results possess high resolution. The dilatation rate of the North China seismic zone in the East China region is relatively complex. The intersection of the Zhangjiakou-Bohai seismic zone and the Tanlu Fault has the largest dilatation rate, and the Tangshan earthquake occurred in this area in 1976. In addition, the number of large earthquakes is also higher in this area than in the surrounding regions. The SCB is relatively stable and has never experienced an earthquake of $M \geq 5.5$ since 1960 and the dilatation rate in this region is close to zero.

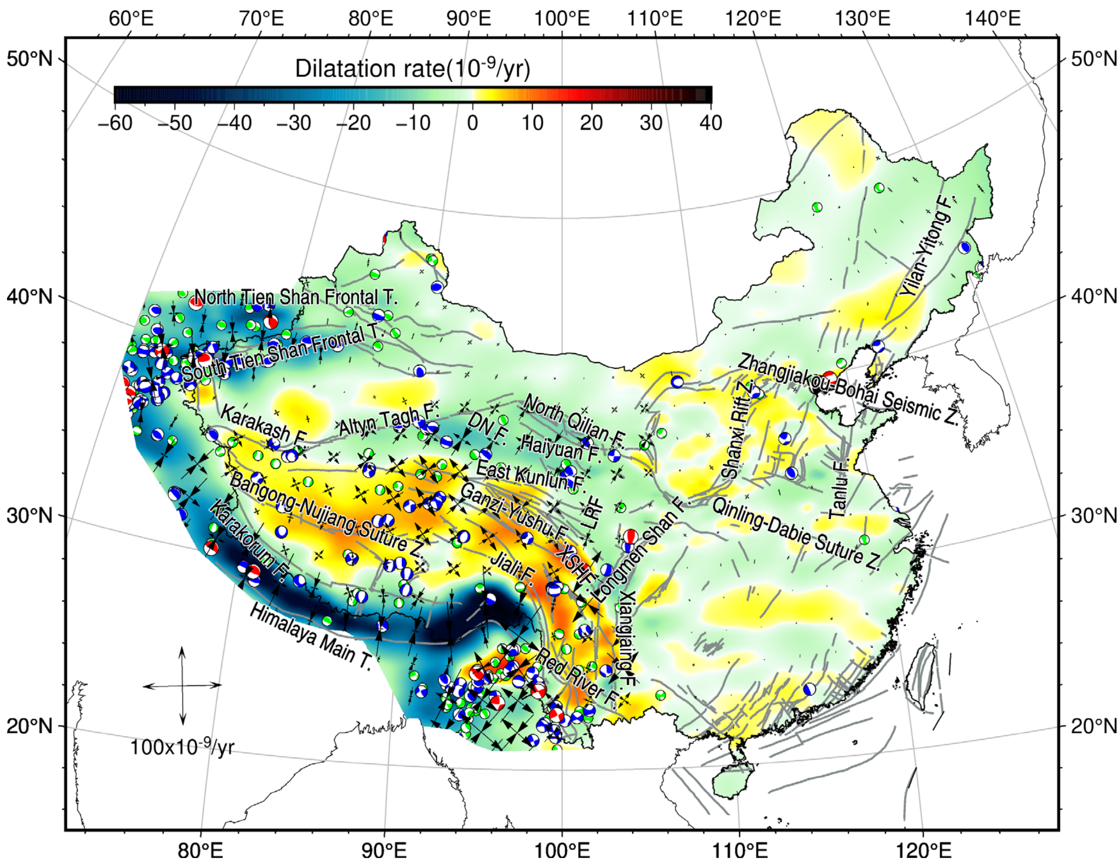

Figure 11. The dilatation rate of continental China. The gray lines on the background denote activity tectonic in continental China; The crossed arrows indicate the magnitude and direction of the maximum and minimum principal strains. The seismic mechanism in continental China from January 1, 1976, to December 31, 2021, is shown in the figure by the focal sphere. The red focal sphere indicates $M \geq 7.5$, the deep blue focal sphere indicates $7.5 \geq M \geq 6.5$, and the green focal sphere indicates $6.5 \geq M \geq 5.5$. Fault name abbreviations are as follows: DNF, Danghe-NanshanFault; LRF, Longriba Fault; XSHF, Xiashuihe Fault.

The background in Figure 12 shows the MSSR (maximum shear strain rate). We still see a clear division between East and West China along $105\,°E$. MSSR is strongly correlated with earthquakes whose source mechanisms are strike-slip faults. In Figure 12, we can conclude that the areas with an MSSR greater than $40 \times 10^{-9}/yr$ are widely distributed on strike-slip faults and reverse-fault earthquakes. By the collisional compression of the Indian plate, the MSSR in continental China is greatest in the western and eastern sections of the HMT. Indian plate directly extrudes the eastern section of the Himalayas, and the MSSR reaches about $100 \times 10^{-9}/yr$. While the eastern section is rotated due to lateral extrusion from the Tibetan plateau, the MSSR reaches about $120 \times 10^{-9}/yr$. Longmenshan Fault, Xiangjiang Fault, and XSHF are located at the junction of Qinghai-Tibetan Plateau and SCB under great compression, and the MSSR has also reached $100 \times 10^{-9}/yr$. The MSSR of the North and South Tianshan Frontal Thrust, influenced by the far field of the Indian Plate extrusion, reaches about $70 \times 10^{-9}/yr$. In the northern and northeastern margins of the Tibetan Plateau, the MSSR show a clear boundary with the stable blocks in the north. In the areas where strike-slip earthquakes are widely developed in the interior of the Tibetan Plateau, the MSSR is more than $40 \times 10^{-9}/yr$. In East China, except for

Zhangjiakou-Bohai Seismic Zone and Yilan-Yitong Fault, the MSRR of other areas is very small and close to $10 \times 10^{-9}/yr$. The MSRR in most of Eastern China is very small, close to $10 \times 10^{-9}/yr$. Only ZBSZ and YYF have MSRR close to $40 \times 10^{-9}/yr$, and there is also some large earthquake distribution. Due to the special plate tectonics of the Chinese continent, the Tibetan Plateau is blocked by the surrounding rigid blocks as it expands outward under compression. All strain rate data are listed in Table S2-S4.

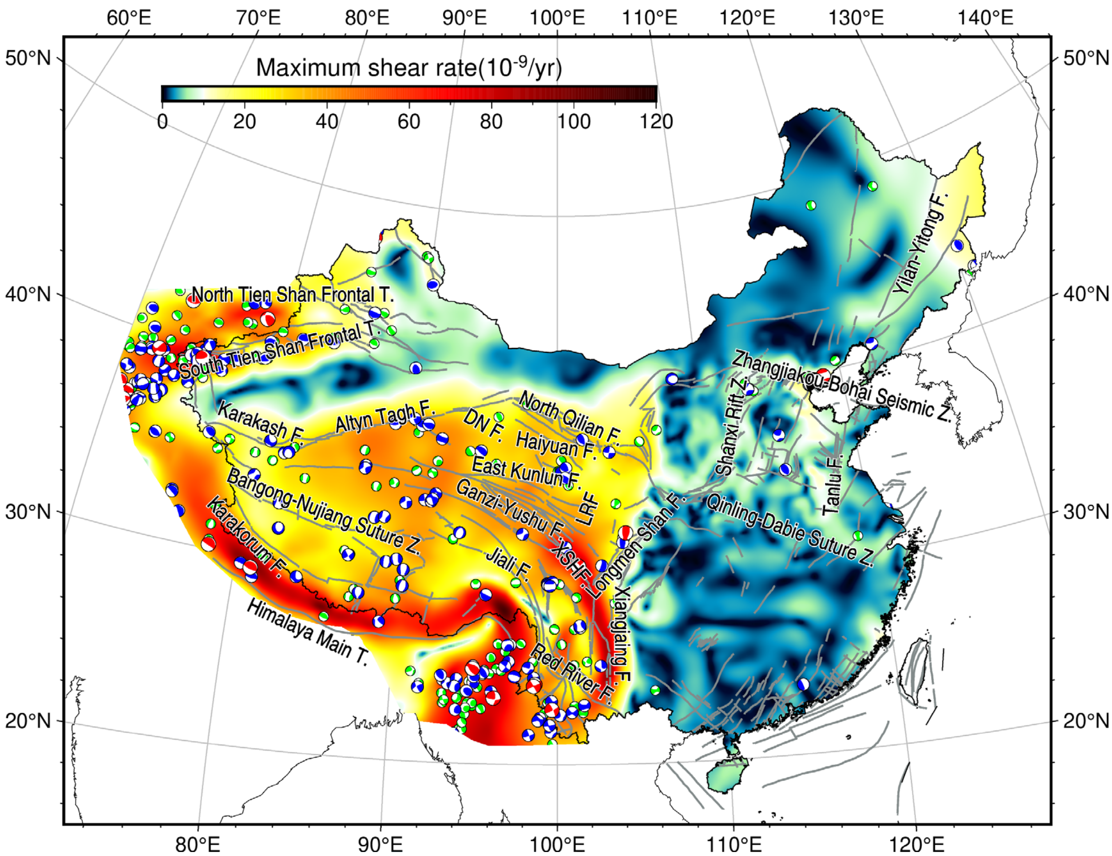

Figure 12. The maximum shear rate of continental China. The gray lines on the background denote active tectonic in continental China. The seismic mechanism in continental China from January 1, 1960, to December 31, 2021, is shown in the figure by the focal sphere. The red focal sphere indicates $M \geq 7.5$, the deep blue focal sphere indicates $7.5 \geq M \geq 6.5$, and the green focal sphere indicates $6.5 \geq M \geq 5.5$ (same as Figure 11).

7 Discussions

7.1 Deformation and Strain Rates of Continental China

7.1.1 Overview of Continental China

Because of the multiscale spherical spline interpolation method, our dilatation rate results (Figure 11 and Figure 12) improve the resolution of the primary structure compared to the previous ones (Rui & Stamps, 2019; Wang & Shen, 2020). Continent China is located in the squeeze triangle of the Indian and Pacific plates and is extremely active in tectonic activities. We propose a concept named 10^{-8} Shear Zone to visualize the influence of the extrusion of these two plates on the deformation of the entire Chinese continent, and we can observe this shear zone in Figure 12. The central part of the 10^{-8} Shear Zone starts at Karakorum F. in the east, extends to ATF and NQF (North Qianlian F.), and curves upward to Northwest Ordos. Then, this shear zone extends down the western edge of the Ordos, passes through the Qinling Mountains, extends the Shanxi Rift Z. on the eastern edge of the Ordos northward to Zhangjiakou, and finally extends the ZBSZ eastward to the Bohai Sea. In addition, there are two other important branches of this shear zone. The first branch extends to the junction of the Southern Tien Shan and the Tarim Basin, then northward in the middle of the Southern Tien Shan to the middle of the Northern Tien Shan, dividing the entire Northern and Southern Tien Shan into East and Western sections. This section of the branch shear zone is connected to the main shear zone on the west side of KF (Karakash F.). Another branch extends through LMSF (Longmen Shan F.) and XJF (Xiaojiang F.), joining the main shear zone in southwest of Ordos. This branch also coincides with the boundary between the Tibetan Plateau and South China. We can see that the tensile and compressive strains within the blocks around the Tibetan Plateau, such as the Tarim block, the Alashan block, the Ordos block, and the South China block, are small in Figure 11. At the same time, the maximum shear strains of these blocks are also small in Figure 12, indicating that these blocks exhibit rigid body properties. But the effects of the squeeze don't go away, with far-field effects affecting areas further afield. Tianshan's high shear strain rate and high extrusion strain rate result from the influence of far-field benefits. Thus, in western China and around the $105°E$, the 10^{-8} Shear Zone mainly indicates the extent of influence of the Indian subcontinent squeezing continental China. Although North China is affected by the dual far-field effects of the Tibetan Plateau and the Pacific Plate, the 10^{-8} Shear Zone also indicates their influence. This shear zone provides visual evidence of the extent to which localized deformation in continental China is affected by plate extrusion and avoids attributing deformations whose causes are unclear to plate extrusion or its far-field effects.

7.1.2 Deformation of Tibetan Plateau

The Tibetan Plateau is inevitably one of continental China's most dramatic active tectonics. The thickening, shortening, and lateral extrusion of the Tibetan Plateau under the compression of the Indian plate and the blocking of surrounding blocks is noticeable and almost indisputable (Gan et al., 2007). However, whether crustal thickening or lateral extrusion played a major role in balancing the plateau's uplift is still controversial. An accurate description of the deformation of the Tibetan Plateau is therefore essential for clarifying these issues. There have been many deformation studies based on GPS velocity fields, and researchers customarily use relative velocity models to delineate microplates and account for their interactions. It may sometimes neglect the overall deformation, so it is more reasonable to use strain rates composed of velocity gradients because the velocity gradient does not vary with the reference system. The microplates of the Tibetan Plateau have been carefully delineated in recent years (Loveless & Meade, 2011; Meade, 2007; Thatcher, 2007; Wang et al., 2017), the microplate model and the continuum deformation model have been harmonized. Rotation has always been a concern in microplate modeling. From our strain rate results, we can get that the internal deformation properties of the Tibetan Plateau tend to be consistent, and the drastic changes in values and properties are mainly at the edge of the Tibetan Plateau. Wang et al. (2017) used the GPS velocity field and microplate model to obtain that the southwestern part of the Tibetan Plateau shows a counterclockwise rotation, the southeastern part shows a clockwise rotation, the Tsaidam Basin shows a clockwise rotation, and the middle part of the Himalaya shows a counterclockwise rotation. In Figure S9, we offer the results of the rotational strain rate where positive values indicate counterclockwise and negative values indicate clockwise. My results generally agree with the nature of Wang et al. (2017) in the southwestern and northeastern Tibetan Plateau, and the nature of the rotation in the Tsaidam Basin and the middle Himalayas is opposite to his results. But our results are identical to those of Ge et al. (2015) and Wang & Shen (2020). Wang et al. (2017) use Ma as the unit of time, and the rotation values in the regions that do not agree with our results are smaller, so there may be some errors in the statistics and calculations. Thus, it follows from our rotational strain rate model that the interior of the Tibetan Plateau may not need to be divided into many microplates to explain deformation. We can see from Fig. 2 that the resolution of our strain rate model on the Tibetan Plateau reaches 110 km at the largest spatial scale (scale factor $q \geq 6$, The larger the scale factor, the higher the resolution), which can fully satisfy the current microplate scale. Of course we don't fully support this model of the Tibetan Plateau as a whole piece. Because our results support the traditional delineation of land parcels bounded by large active tectonics. In Fig. 12, we see the variation of the MSSR on both sides of the BNF to distinguish the Lhasa block from the Qiangtang block. In Fig. 11, we see a change in the nature of the tensile on either side of the EKF (East Kunlun F.) to distinguish the Songpan-Ganzi Block from the Qiangtang Block. There is also a clear zone of high extrusion in the middle of the Qaidam Basin and the Songpan-Ganzi Block. So how can researchers improve the accuracy of numerical experiments to explain the crustal deformation of the Tibetan Plateau without microplates? We believe that it is possible to improve the resolution of the elastic parameters of the material. Our study has given high-resolution strain rates, and high-resolution continuous elastic parameters can be obtained after simple calculations using the Hooke's law (All strain rate data are listed in Table S2-S4). Numerical modeling in conjunction with current plate delineation based on large active ruptures may have been able to give better results.

Another deformation of interest is a crustal circulation channel on the eastern Tibetan Plateau and where it begins and ends. Many researchers believe that the Tibetan Plateau, as it extrudes laterally to the east, is blocked by the tough Sichuan Basin to form northward and southward branches. Branching to the north extends to the RRF (Red River F.), and branching to the east rises to the edge of the Ordos block (Bai et al., 2010; Bao et al., 2015; Zhang et al., 2020). The existence of lower and middle crustal flows has been confirmed by much geophysical observational evidence on the northeast Tibetan Plateau, such as the hyperthermal layer (Deng & Tesauro, 2016; Jiang et al., 2019), the lower and middle crustal low-resistive layers (Zhao et al., 2012), distribution of epicenter depths (Liang et al., 2008; Wang et al., 2020; Wei et al., 2010) and the anisotropy of the crust (Kong et al., 2016; Zheng et al., 2018). There is no evidence of a lubricating or decoupling layer between the lower and middle crust and the upper crust. Therefore, the deformation of the lower and middle crust should be consistent with that of the upper crust. In figure 11, our results show that the crustal flow in the southeastern Tibetan Plateau is divided into two streams, the first one extending from Ganzi-Yushu F., XSHF to XJF., and the other extending from Jiali F. to RRF. It is consistent with the current study. It is also surface observational evidence for the existence of crustal flows. In addition, our results show that the two crustal flow channels are connected near XSHF and XJF. However, our dilatation rates result do not show the effect of crustal flow on the surface in the northeastern Tibetan Plateau, and only the northeastern portion of the Tibetan Plateau showed slightly higher maximum shear rates. It may suggest no large-scale crustal flow in the northeastern Tibetan Plateau or a lubricating layer between the lower and middle crust and the upper crust. Even if there was crustal flow, it didn't spread to the edge of the Ordos Block.

7.1.3 Deformation of North China in Continental China

North China is another region of high seismicity in mainland China, where the deformation and dynamics of the region are of great interest because of the large population and industrial bases and the extrusion of both the eastern side of the Tibetan Plateau and the western Pacific Plate. Figure S9 shows details of strain rates in North China. Our maximum strain rates are similar to the results obtained by the most recent modeling approach using elastic-plastic layering (Shen et al., 2023). The MSSR at the northern edge of the Ordos block is smaller than the other boundaries, showing a semi-enveloped morphology. The MSSR at the northern edge of the Ordos Block is smaller than the different boundaries. It suggests a longer recurrence cycle of strong earthquakes in northern Ordos. Our results differ from Shen et al. (2023) in areas where strain is concentrated. In Figure S10, the eastern part of the Zhangjiakou-Bohai Seismic Zone, where the Tangshan earthquake occurred, is a strain rates concentration area with short recurrence periods of strong earthquakes requiring focused monitoring. In addition, the areas of relatively large strain rates in the North China block are concentrated around the active tectonics, including the Shanxi Rift Z., Anyang-Heze-Linyi F., Weihe Rift, and THCF (Tang Shan-Hejian-Cixian F.). At the boundary between North and South China, Qinling-Dabie Suture Z., there is no stress concentration, and our results are consistent with Shen et al. (2023) and seismological perception (Yu & Chen, 2016). However, we used more intensive measured data to obtain a strain rate model with higher resolution, which also supports the current dominant block models (DENG et al., 2003; Wang et al., 2022; Yin et al., 2015). Thus, our results may be more plausible.

The 10^{-8} shear zone is still in effect in North China, and this zone extends to the THCF and the Tanlu Fault, suggesting that these two active tectonic structures are the concentration of strain in North China as a result of the extrusion of the Tibetan Plateau and the Pacific Plate.

7.2 Seismic Activity and Strain Rates of Continental China

As mentioned earlier in our study, Figure 11 demonstrates that dilatation is highly consistent with the source mechanism of $M \geq 5.5$ earthquakes. Figure 12 demonstrates the agreement of the MSSR with earthquakes on strike-slip faults of $M \geq 5.5$. In addition, there are no major earthquakes in areas where the dilatation rate or the MSSR is anomalous. We consider these areas with abnormal strain rate values as earthquake warning areas. In Figure 11, the dilatation rate along the ATF is approximately $-20 \times 10^{-8}/yr$, and only the western section of the ATF is more seismically intense. In Figure 12, The small MSRR in the east section of the ATF may be why there are fewer large earthquakes in this region. The eastern section of TSFT (TianShan Frontal T.) and the eastern section of the ATF have the same strain rate and seismic distribution characteristics, and this feature is also found in the triangle enclosed by LRF (Longriba F.), XSHF, and LMSF. Although Figures 11 and 12 show that the NQF has this feature again, that is because of the absence of data on the seismic mechanism, and we know from Figure 10 that there is a large distribution of earthquakes in this area. Although the dilatation rate of the western edge of the Ordos block is low, the MSRR is large, especially since the intersection with NQF has the possibility of large earthquakes. The distribution of only a few earthquakes $M \geq 5.5$ in northern China is consistent with the distribution of high values of the dilatation rate and the MSRR, and these areas remain of concern.

7.3 Spherical Spline Method

The spherical spline can directly give a derivative of GNSS velocity, which does not depend on the fitting result of the velocity field. Furthermore, the spherical harmonics detection model shows numerical stability with a large velocity gradient. However, the maximum order and degree of spherical harmonics we use are 96 and 48. We also obtain the ideal results using bigger orders and degrees' spherical harmonics detection model. We observe that there is one station data at the edge of a grid, then this side of the edge of the grid will recover the value sign (positive and negative) of the grid where it is located. (e.g., Figures 5 and 7).

As we mentioned at the beginning of this article, we have developed a set of test criteria to judge whether some methods of calculating strain rate using GPS or GNSS velocity are effective. The criteria do not target spherical spline mainly. In geophysical and geodynamic research, the effectiveness of fitting or smoothing using a different method for the same discrete data has some visible discrepancies. However, only some methods perform well within a large study area. Some methods are better than others in local areas, which is also the principal aspect discussed by researchers when they select fitting or smoothing methods. We present a spherical harmonics grid inspection model by analogy with a seismic wave velocity checkboard test. Using spherical harmonics with a grid distribution feature, we can judge the overall fitting effect of a strain rate calculating method in the study area and consider the local detail resolution of the technique. Even if the same data is used, different methods have different local resolutions, so higher-resolution methods can also be an option in other parts of a larger study area.

Of course, the way to solve the interpolation accuracy and to get a better smoothing effect is to increase the station density locally. However, refining stations in all areas, regardless of cost, is not conducive to cost savings and efficiency, so we use the spherical harmonic grid test model to determine whether the distribution of stations in the study target area is reasonable and improved. We take the station density distribution in continental China as an example. From the results of the spherical harmonic lattice test of the spherical strip, it is necessary to increase the stations in the rectangular area from $32°N$ to $37°N$, $81°E$ to $92°E$. This area has experienced major earthquakes and is in the Tibetan hinterland, a famous no-man's land. However, the deformation mechanism within the Qinghai-Tibet Plateau is still unclear. Based on the spherical spline results, it is unnecessary to deploy stations intensively, but only to add 3-5 stations over a wide range area to significantly improve the resolution of strain rate results. In addition, the spherical harmonic test also shows that adding two or three stations in the hinterland of the Qaidam Basin and the Alashan massif is also beneficial to improving the computational accuracy of the north-south derivatives (which is mainly related to $\dot{\varepsilon}_{\varphi}$). Refining station in other areas is practically unnecessary.

No matter what method or data is used, data can be filtered, and methods can be chosen differently, but the study area is permanently fixed. Although we recommend using different methods in different regions in the previous section, using various methods locally in a fixed study area may have some continuity problems on the boundaries. Moreover, in the last quarter, we mentioned that spherical coordinates are more reliable at high latitudes (e.g., Iceland) or in a large study area at low latitudes (e.g., continental China). Jiang *et al.* (2011) concluded that the least-squares collocation method in spherical coordinates is superior to other methods. However, the least-squares collocation method is based on first-order Taylor expansions of displacement or velocity fields in the spherical and Cartesian coordinate systems. It is like linear interpolation, which can only guarantee the continuity of the strain rate but not the smoothness. This method is reasonable when the stations are dense, but when the stations are sparse, the calculation results are not guaranteed to be practical. Therefore, in addition to proposing a set of test criteria for the strain rate method, this paper also recommends that researchers use the spherical spline method, which is not only a high-precision spherical coordinate method but also ensures continuous and smooth strain rate results.

8 Conclusions

We propose a set of criteria to test the practicality of calculating strain or strain rate fields using GPS or GNSS data. This set of standards is also illustrated using the spherical spline method utilizing the location of stations in and around continental China.

The final three main conclusions drawn in this paper are

(1) Unlike the Cartesian coordinate method, the spherical coordinate method can be adapted to examine rigid body rotation models and reduce the error to less than one percent or even one thousandth. The spherical harmonic grid model is designed to visualize the method's resolution. We can use different sizes and shapes of spherical harmonic grids to examine our strain rate calculation methods rather than just the spherical spline method used in this paper.

(2) The 10^{-8} reveals the extent to which the Chinese mainland is affected by the extrusion of the Indian plate and the extrusion of the Pacific plate. This zone is also valid in North China.

(3) It may be more reasonable to explain the deformation mechanism of the Tibetan Plateau using a continuum model. At the same time, the high-resolution strain rate we provide helps to obtain continuous high-resolution elastic parameters.

(4) We provide strain rate evidence for the distribution of lower and middle crustal flows on the southeastern Tibetan Plateau and inform the connectivity of the two side channels.

(5) The region of high shear strain rate in North China overlaps with the microplate margins delineated by active fault. However, Tangshan is still the region with the highest MSRR and the dilation rate, which needs to be highly emphasized.

(6) The dilatation rate and the MSRR calculated using the spherical spline method have an excellent performance in analyzing the seismic mechanisms of faults or earthquakes. It is recommended that other researchers use the spherical spline method when analyzing the seismic mechanism. Attention must be focused on areas with large dilatation rates and MSRR, especially those anomalous compared to the surrounding areas with a high potential for future major earthquakes.

Acknowledgments

This research is supported by the National Science Foundation of China (U2239205, 41725017) and the National Key R&D Program of the Ministry of Science and Technology of China (2020YFA0713401). It is also partially supported by the National Key Scientific and Technological Infrastructure project "Earth System Science Numerical Simulator Facility" (EarthLab). All the authors greatly appreciate Professor Carl Tape for providing the software package to us.

Open Research

The GNSS data used in this study were taken from published papers (Li et al., 2022; Wang & Shen, 2020; Wang et al., 2022) and are listed in Table S1. The GNSS velocity and strain rate data are published to Zenodo (https://zenodo.org/records/10215151). Earthquake Catalog was obtained from USGS (United States Geological Survey) (https://earthquake.usgs.gov/fdsnws/event/1/query.csv?starttime=1960-01-01%2000:00:00&endtime=2021-12-31%2023:59:59&maxlatitude=55.479&minlatitude=15.824&maxlongitude=138.516&minlongitude=69.082&minmagnitude=5.5&orderby=time). The seismic mechanism data were obtained from the Global Centroid Moment Tensor (Dziewonski et al., 2012; Ekström et al., 2012) (https://www.globalcmt.org/cgi-bin/globalcmt-cgi-bin/CMT5/form?itype=ymd&yr=1976&mo=1&day=1&otype=ymd&oyr=2021&omo=12&oday=31&jyr=1976&jday=1&ojyr=1976&ojday=1&nday=1&lmw=5.5&umw=10&lms=0&ums=10&lmb=0&umb=10&llat=15&ulat=55&llon=70&ulon=140&lhd=0&uhd=1000&lts=-9999&uts=9999&lpe1=0&upe1=90&lpe2=0&upe2=90&list=6).

Reference

Backus, G. (1967). Numerical applications of a formalism for geophysical inverse problems. *Geophysical Journal International, 13*(1-3), 247-276. doi: 10.1111/j.1365-246X.1967.tb02159.x

Backus, G. (1968). The resolving power of gross earth data. *Geophysical Journal International, 16*(2), 169-205. doi: 10.1111/j.1365-246X.1968.tb00216.x

Backus, G. (1970). Uniqueness in the inversion of inaccurate gross earth data. *Royal Society, 266*(1173), 123-192. doi: 10.1098/rsta.1970.0005

Bai, D., Unsworth, M. J., Meju, M. A., Ma, X., Teng, J., Kong, X., et al. (2010). Crustal deformation of the eastern Tibetan plateau revealed by magnetotelluric imaging. *Nature Geoscience, 3*(5), 358-362. doi: 10.1038/ngeo830

Bao, X., Sun, X., Xu, M., Eaton, D. W., Song, X., Wang, L., et al. (2015). Two crustal low-velocity channels beneath SE Tibet revealed by joint inversion of Rayleigh wave dispersion and receiver functions. *Earth and Planetary Science Letters, 415*, 16-24. doi:

Bürgmann, R. (2005). Interseismic coupling and asperity distribution along the Kamchatka subduction zone. *Journal of Geophysical Research, 110*(B7), B07405. doi: 10.1029/2005jb003648

Chen, Q., Freymueller, J. T., Yang, Z., Xu, C., Jiang, W., Wang, Q., & Liu, J. (2004). Spatially variable extension in southern Tibet based on GPS measurements. *Journal of Geophysical Research: Solid Earth, 109*(B9), n/a-n/a. doi: 10.1029/2002jb002350

Day, A. J., Peirce, C., & Sinha, M. C. (2001). Three‐dimensional crustal structure and magma chamber geometry at the intermediate‐spreading, back‐arc Valu Fa Ridge, Lau Basin—results of a wide‐angle seismic tomographic inversion. *Geophysical Journal International, 146*(1), 31-52. doi: 10.1046/j.0956-540X.2001.01446.x

DENG, Q., ZHANG, P., RAN, Y., YANG, X., MIN, W., & CHU, Q. (2003). Basic characteristics of active tectonics of China. *Science in China Series D-Earth Sciences, 46*(4), 356-372. doi: 10.1360/03yd9032

Deng, Y., & Tesauro, M. (2016). Lithospheric strength variations in Mainland China: Tectonic implications. *Tectonics, 35*(10), 2313-2333. doi: 10.1002/2016tc004272

Devachandra, M., Kundu, B., Catherine, J., Kumar, A., & Gahalaut, V. K. (2014). Global Positioning System (GPS) Measurements of Crustal Deformation across the Frontal Eastern Himalayan Syntaxis and Seismic‐Hazard Assessment. *Bulletin of the Seismological Society of America, 104*(3), 1518-1524. doi: 10.1785/0120130290

Dziewonski, A. M., Chou, T. A., & Woodhouse, J. H. (2012). Determination of earthquake source parameters from waveform data for studies of global and regional seismicity. *Journal of Geophysical Research: Solid Earth, 86*(B4), 2825-2852. doi: 10.1029/JB086iB04p02825

Ekström, G., Nettles, M., & Dziewoński, A. M. (2012). The global CMT project 2004–2010: Centroid-moment tensors for 13,017 earthquakes. *Physics of the Earth and Planetary Interiors, 200-201*, 1-9. doi: 10.1016/j.pepi.2012.04.002

Franklin, J. N. (1970). Well-posed stochastic extensions of ill-posed linear problems. *Journal of Mathematical Analysis and Applications, 31*(3), 682-716. doi: 10.1016/0022-247X(70)90017-X

Gan, W., Zhang, P., Shen, Z.-K., Niu, Z., Wang, M., Wan, Y., et al. (2007). Present-day crustal motion within the Tibetan Plateau inferred from GPS measurements. *Journal of Geophysical Research, 112*(B8), B08416. doi: 10.1029/2005jb004120

Ge, W.-P., Molnar, P., Shen, Z.-K., & Li, Q. (2015). Present-day crustal thinning in the southern and northern Tibetan Plateau revealed by GPS measurements. *Geophysical Research Letters, 42*(13), 5227-5235. doi: 10.1002/2015gl064347

Ge, W.-P., Wang, M., Shen, Z. K., Yuan, D. Y., & Zheng, W. J. (2013). Intersiesmic kinematics and information patterns on the upper crust of Qaidan-Qilianshan block. *Chinese J. Geophys. (in Chinese), 56*(09), 2994-3010. doi: 10.6038/cjg20130913

Ge, W. P., Shen, Z. K., Molnar, P., Wang, M., Zhang, P. Z., & Yuan, D. Y. (2022). GPS Determined Asymmetric Deformation Across Central Altyn Tagh Fault Reveals Rheological Structure of Northern Tibet. *Journal of Geophysical Research: Solid Earth, 127*(9). doi: 10.1029/2022jb024216

Glahn, A., Granet, M., & Group, R. G. T. (1993). Southern Rhine Graben: small-wavelength tomographic study and implications for the dynamic evolution of the graben. *Geophysical Journal International, 113*(2), 399-418. doi: 10.1111/j.1365-246X.1993.tb00896.x

Graeber, F. M., Houseman, G. A., & Greenhalgh, S. A. (2002). Regional teleseismic tomography of the western Lachlan Orogen and the Newer Volcanic Province, southeast Australia. *Geophysical Journal International, 149*(2), 249-266. doi: 10.1111/j.1365-246X.1993.tb00896.x

Hao, M., Li, Y., & Zhuang, W. (2019). Crustal movement and strain distribution in East Asia revealed by GPS observations. *Scientific Reports, 9*(1), 16797. doi: 10.1038/s41598-019-53306-y

Hao, M., Wang, Q., Zhang, P., Li, Z., Li, Y., & Zhuang, W. (2021). "Frame Wobbling" Causing Crustal Deformation Around the Ordos Block. *Geophysical Research Letters, 48*(1). doi: 10.1029/2020gl091008

Hori, M., Kameda, T., & Kato, T. (2001). Application of the inversion method to a GPS network for estimating the stress increment in Japan. *Geophysical Journal International, 144*(3), 597-608. doi: 10.1046/j.1365-246x.2001.01337.x

Jiang, G., Hu, S., Shi, Y., Zhang, C., Wang, Z., & Hu, D. (2019). Terrestrial heat flow of continental China: Updated dataset and tectonic implications. *Tectonophysics, 753*, 36-48. doi: 10.1016/j.tecto.2019.01.006

Jiang, G., Xu, C., Wen, Y., Xu, X., Ding, K., & Wang, J. (2014). Contemporary tectonic stressing rates of major strike-slip faults in the Tibetan Plateau from GPS observations using Least-Squares Collocation. *Tectonophysics, 615-616*, 85-95. doi: 10.1016/j.tecto.2013.12.022

Jiang, Z.-S., & Liu, J.-N. (2010). The method for establishing strain field and velocity field of crustal movement using least squares collocation. *Chinese J. Geophys. (in Chinese), 53*(05), 1109+1116-1117. doi: doi.org/10.1002/cjg2.1507

Kong, F., Wu, J., Liu, K. H., & Gao, S. S. (2016). Crustal anisotropy and ductile flow beneath the eastern Tibetan Plateau and adjacent areas. *Earth and Planetary Science Letters, 442*, 72-79. doi:

Kreemer, C., Blewitt, G., & Klein, E. C. (2014). A geodetic plate motion and Global Strain Rate Model. *Geochemistry, Geophysics, Geosystems, 15*(10), 3849-3889. doi: 10.1002/2014gc005407

Lancaster, P., & Salakauskas, K. (1986). *Curve and Surface Fitting, an Introduction*: Academic Press.

Lanza, F., Thurber, C. H., Syracuse, E. M., Power, J. A., & Ghosh, A. (2020). Seismic tomography of compressional wave velocity and attenuation structure for Makushin Volcano, Alaska. *Journal of Volcanology and Geothermal Research, 393*, 106804. doi: 10.1016/j.jvolgeores.2020.106804

Leigh H. Royden, B. Clark Burchfiel, Robert W. King, Erchie Wang, Zhiliang Chen, Feng Shen, & Liu, Y. (1997). Surface Deformation and Lower Crustal Flow in Eastern Tibet. *Science, 276*. doi: 10.1126/science.276.5313.788

Li, H., Li, S., Song, X. D., Gong, M., Li, X., & Jia, J. (2012). Crustal and uppermost mantle velocity structure beneath northwestern China from seismic ambient noise tomography. *Geophysical Journal International, 188*(1), 131-143. doi: 10.1111/j.1365-246X.2011.05205.x

Li, J., Yao, Y., Li, R., Yusan, S., Li, G., Freymueller, J. T., & Wang, Q. (2022). Present‐Day Strike‐Slip Faulting and Thrusting of the Kepingtage Fold‐and‐Thrust Belt in Southern Tianshan: Constraints From GPS Observations. *Geophysical Research Letters, 49*(11). doi: 10.1029/2022gl099105

Li, K., Li, Y., Tapponnier, P., Xu, X., Li, D., & He, Z. (2021). Joint InSAR and Field Constraints on Faulting During the Mw 6.4, July 23, 2020, Nima/Rongma Earthquake in Central Tibet. *Journal of Geophysical Research: Solid Earth, 126*(9). doi: 10.1029/2021jb022212

Liang, S., Gan, W., Shen, C., Xiao, G., Liu, J., Chen, W., et al. (2013). Three‐dimensional velocity field of present‐day crustal motion of the Tibetan Plateau derived from GPS measurements. *Journal of Geophysical Research: Solid Earth, 118*(10), 5722-5732. doi: 10.1002/2013JB010503

Liang, X., Zhou, S., Chen, Y. J., Jin, G., Xiao, L., Liu, P., et al. (2008). Earthquake distribution in southern Tibet and its tectonic implications. *Journal of Geophysical Research: Solid Earth, 113*(B12). doi:

Liu, M., Yang, Y., Shen, Z., Wang, S., Wang, M., & Wan, Y. (2007). Active tectonics and intracontinental earthquakes in China: The kinematics and geodynamics. In *Continental Intraplate Earthquakes: Science, Hazard, and Policy Issues*.

Loveless, J. P., & Meade, B. J. (2010). Geodetic imaging of plate motions, slip rates, and partitioning of deformation in Japan. *Journal of Geophysical Research, 115*(B2), B02410. doi: 10.1029/2008jb006248

Loveless, J. P., & Meade, B. J. (2011). Partitioning of localized and diffuse deformation in the Tibetan Plateau from joint inversions of geologic and geodetic observations. *Earth and Planetary Science Letters, 303*(1-2), 11-24. doi: 10.1016/j.epsl.2010.12.014

Masson, F., Lehujeur, M., Ziegler, Y., & Doubre, C. (2014). Strain rate tensor in Iran from a new GPS velocity field. *Geophysical Journal International, 197*(1), 10-21. doi: 10.1093/gji/ggt509

Meade, B. J. (2007). Present-day kinematics at the India-Asia collision zone. *Geology, 35*(1). doi: 10.1130/g22924a.1

Métois, M., Socquet, A., & Vigny, C. (2012). Interseismic coupling, segmentation and mechanical behavior of the central Chile subduction zone. *Journal of Geophysical Research: Solid Earth, 117*(B3), B03406. doi: 10.1029/2011jb008736

Okazaki, T., Fukahata, Y., & Nishimura, T. (2021). Consistent estimation of strain-rate fields from GNSS velocity data using basis function expansion with ABIC. *Earth, Planets and Space, 73*(1). doi: 10.1186/s40623-021-01474-5

Pang, Y., Wu, Y., Li, Y., & Chen, C. (2023). The mechanism of the present-day crustal deformation in southeast Tibet: from numerical modelling and geodetic observations. *Geophysical Journal International, 235*(1), 12-23. doi: 10.1093/gji/ggad200

Qi, W., Xuejun, Q., Qigui, L., Freymueller, J., Shaomin, Y., Caijun, X., et al. (2011). Rupture of deep faults in the 2008 Wenchuan earthquake and uplift of the Longmen Shan. *Nature Geoscience, 4*(9), 634-640. doi: 10.1038/ngeo1210

Qu, W., Lu, Z., Zhang, Q., Wang, Q., Hao, M., Zhu, W., & Qu, F. (2018). Crustal deformation and strain fields of the Weihe Basin and surrounding area of central China based on GPS observations and kinematic models. *Journal of Geodynamics, 120*, 1-10. doi: 10.1016/j.jog.2018.06.003

Rawlinson, N., Salmon, M., & Kennett, B. L. (2014). Transportable seismic array tomography in southeast Australia: Illuminating the transition from Proterozoic to Phanerozoic lithosphere. *Lithos, 189*, 65-76. doi: 10.1016/j.lithos.2013.06.001

Rui, X., & Stamps, D. S. (2019). A Geodetic Strain Rate and Tectonic Velocity Model for China. *Geochemistry, Geophysics, Geosystems, 20*(3), 1280-1297. doi: 10.1029/2018gc007806

Savage, J. C., Gan, W., & Svarc, J. L. (2001). Strain accumulation and rotation in the Eastern California Shear Zone. *Journal of Geophysical Research: Solid Earth, 106*(B10), 21995-22007. doi: 10.1029/2000jb000127

She, Y., & Fu, G. (2020). Uplift Mechanism of the Highest Mountains at Eastern Himalayan Syntaxis Revealed by In Situ Dense Gravimetry. *Geophysical Research Letters, 47*(22). doi: 10.1029/2020gl091208

Shen, F., Wang, L., Barbot, S., & Xu, J. (2023). North China as a mechanical bridge linking Pacific subduction and extrusion of the Tibetan Plateau. *Earth and Planetary Science Letters, 622*. doi: 10.1016/j.epsl.2023.118407

Shen, Z.-K., Jackson, D. D., & Ge, B. X. (1996). Crustal deformation across and beyond the Los Angeles basin from geodetic measurements. *Journal of Geophysical Research: Solid Earth, 101*(B12), 27957-27980. doi: 10.1029/96jb02544

Shen, Z.-K., Sun, J., Zhang, P., Wan, Y., Wang, M., Bürgmann, R., et al. (2009). Slip maxima at fault junctions and rupturing of barriers during the 2008 Wenchuan earthquake. *Nature Geoscience, 2*(10), 718-724. doi: 10.1038/ngeo636

Shen, Z.-K., Wang, M., Li, Y., Jackson, D. D., Yin, A., Dong, D., & Fang, P. (2001). Crustal deformation along the Altyn Tagh fault system, western China, from GPS. *Journal of Geophysical Research: Solid Earth, 106*(B12), 30607-30621. doi: 10.1029/2001JB000349

Shen, Z.-K., Wang, M., Zeng, Y., & Wang, F. (2015). Optimal Interpolation of Spatially Discretized Geodetic Data. *Bulletin of the Seismological Society of America, 105*(4), 2117-2127. doi: 10.1785/0120140247

Su, X.-N., Meng, G.-J., & Wang, Z. (2016). Methodology and application of GPS strain field estimation based on multi-scaler spherical wavelet. *Chinese J. Geophys. (in Chinese), 59*(05), 1585-1595. doi: 10.6038/cjg20160504

Tape, C., Musé, P., Simons, M., Dong, D., & Webb, F. (2009). Multiscale estimation of GPS velocity fields. *Geophysical Journal International, 179*(2), 945-971. doi: 10.1111/j.1365-246X.2009.04337.x

Thatcher, W. (2007). Microplate model for the present-day deformation of Tibet. *Journal of Geophysical Research, 112*(B1). doi: 10.1029/2005jb004244

Walck, M. C., & Clayton, R. W. (1987). P wave velocity variations in the Coso region, California, derived from local earthquake travel times. *Journal of Geophysical Research: Solid Earth, 92*(B1), 393-405. doi: 10.1029/JB092iB01p00393

Wang, H., Liu, M., Cao, J., Shen, X., & Zhang, G. (2011). Slip rates and seismic moment deficits on major active faults in mainland China. *Journal of Geophysical Research, 116*(B2), B02405. doi: 10.1029/2010jb007821

Wang, M., & Shen, Z. K. (2020). Present - Day Crustal Deformation of Continental China Derived From GPS and Its Tectonic Implications. *Journal of Geophysical Research: Solid Earth, 125*(2), e2019JB018774. doi: 10.1029/2019jb018774

Wang, Q., Zhang, P.-Z., Freymueller, J. T., Bilham, R., Larson, K. M., Lai, X. a., et al. (2001). Present-Day Crustal Deformation in China Constrained by Global Positioning System Measurements. *Science, 294*(5542), 574-577. doi: 10.1126/science.106364

Wang, W., Qiao, X., Yang, S., & Wang, D. (2017). Present-day velocity field and block kinematics of Tibetan Plateau from GPS measurements. *Geophysical Journal International, 208*(2), 1088-1102. doi: 10.1093/gji/ggw445

Wang, W., Zhao, B., Qiao, X., & Ding, K. (2022). Block Kinematics in North China From GPS Measurements. *Geochemistry, Geophysics, Geosystems, 23*(3). doi: 10.1029/2021gc010216

Wang, Y., Deng, Y., Shi, F., & Peng, Z. (2020). The Indo–Eurasia convergent margin and earthquakes in and around Tibetan Plateau. *Journal of Mineralogical and Petrological Sciences, 115*(2), 118-137. doi:

Wang, Z., & Dahlen, F. (1995). Spherical‐spline parameterization of three‐dimensional Earth models. *Geophysical Research Letters, 22*(22), 3099-3102. doi: 10.1029/95GL03080

Wang, Z., Tromp, J., & Ekström, G. (1998). Global and regional surface-wave inversions: A spherical-spline parameterization. *Geophysical Research Letters, 25*(2), 207-210. doi: 10.1029/97gl03634

Wei, S., Chen, Y. J., Sandvol, E., Zhou, S., Yue, H., Jin, G., et al. (2010). Regional earthquakes in northern Tibetan Plateau: Implications for lithospheric strength in Tibet. *Geophysical Research Letters, 37*(19). doi:

Wei, W., Dijin, W., Bin, Z., Yong, H., Caihong, Z., Kai, T., & Shaomin, Y. (2014). Horizontal crustal deformation in Chinese Mainland analyzed by CMONOC GPS data from 2009–2013. *Geodesy and Geodynamics, 5*(3), 41-45. doi: 10.3724/SP.J.1246.2014.03041

Wieczorek, M. A., & Meschede, M. (2018). SHTools: Tools for Working with Spherical Harmonics. *Geochemistry, Geophysics, Geosystems, 19*(8), 2574-2592. doi: 10.1029/2018gc007529

Wiggins, R. A. (1972). The general linear inverse problem: Implication of surface waves and free oscillations for earth structure. *Reviews of Geophysics, 10*(1), 251-285. doi: 10.1029/RG010i001p00251

Wu, Y., Jiang, Z.-S., Yang, G.-h., Fang, Y., & Wang, W.-X. (2009). The Method of GPS Strain Calculation in Whole Mode Using Least Square Collocation on Sphere Surface and Its Application. *Chinese J. Geophys. (in Chinese), 52*(07), 1707-1714. doi: 10.1002/cjg2.1398

Wu, Y., Jiang, Z., Yang, G., Wei, W., & Liu, X. (2011). Comparison of GPS strain rate computing methods and their reliability. *Geophysical Journal International, 185*(2), 703-717. doi: 10.1111/j.1365-246X.2011.04976.x

Xiong, Z., Zhuang, J., Zhou, S., Matsu'ura, M., Hao, M., & Wang, Q. (2021). Crustal strain-rate fields estimated from GNSS data with a Bayesian approach and its correlation to seismic activity in Mainland China. *Tectonophysics, 815*. doi: 10.1016/j.tecto.2021.229003

Xu, X., X.-Y.Wu, Yu, G., Tan, X., & Li, K. (2017). Seismo-geological signatures for identifying M⩾7.0 earthquake risk areas and their premilimary application in mainland China. *seismology and geology, 39*(02), 219-275. doi: 10.3969/j.issn.0253-4967.2017.02

Yang, Q.-Y., Santosh, M., & Dong, G. (2014). Late Palaeoproterozoic post-collisional magmatism in the North China Craton: geochemistry, zircon U–Pb geochronology, and Hf isotope of the pyroxenite–gabbro–diorite suite from Xinghe, Inner Mongolia. *International Geology Review, 56*(8), 959-984. doi: 10.1080/00206814.2014.908421

Yin, A. (2010). Cenozoic tectonic evolution of Asia: A preliminary synthesis. *Tectonophysics, 488*(1-4), 293-325. doi: 10.1016/j.tecto.2009.06.002

Yin, A., & Harrison, T. M. (2000). Geologic evolution of the Himalayan-Tibetan orogen. *Annual Review of Earth and Planetary Sciences, 28*(1), 211-280. doi: 10.1146/annurev.earth.28.1.211

Yin, A., Yu, X., Shen, Z.-K., & Liu-Zeng, J. (2015). A possible seismic gap and high earthquake hazard in the North China Basin. *Geology, 43*(1), 19-22. doi: 10.1130/g35986.1

Yu, J., Tan, K., Zhang, C., Zhao, B., Wang, D., & Li, Q. (2019). Present-day crustal movement of the Chinese mainland based on Global Navigation Satellite System data from 1998 to 2018. *Advances in Space Research, 63*(2), 840-856. doi: 10.1016/j.asr.2018.10.001

Yu, Y., & Chen, Y. J. (2016). Seismic anisotropy beneath the southern Ordos block and the Qinling-Dabie orogen, China: Eastward Tibetan asthenospheric flow around the southern Ordos. *Earth and Planetary Science Letters, 455*, 1-6. doi: 10.1016/j.epsl.2016.08.026

Zhang, F., Wu, Q., Li, Y., Zhang, R., Sun, L., Pan, J., & Ding, Z. (2018). Seismic Tomography of Eastern Tibet: Implications for the Tibetan Plateau Growth. *Tectonics, 37*(9), 2833-2847. doi: 10.1029/2018tc004977

Zhang, P.-Z. (2013). A review on active tectonics and deep crustal processes of the Western Sichuan region, eastern margin of the Tibetan Plateau. *Tectonophysics, 584*, 7-22. doi: 10.1016/j.tecto.2012.02.021

Zhang, P.-Z., Shen, Z., Wang, M., Gan, W., Bürgmann, R., Molnar, P., et al. (2004). Continuous deformation of the Tibetan Plateau from global positioning system data. *Geology, 32*(9), 809-812. doi: 10.1130/G20554.1

Zhang, Z., Yao, H., & Yang, Y. (2020). Shear wave velocity structure of the crust and upper mantle in Southeastern Tibet and its geodynamic implications. *Science China Earth Sciences, 63*, 1278-1293. doi:

Zhao, D., Qu, C., Shan, X., Gong, W., Zhang, Y., & Zhang, G. (2018). InSAR and GPS derived coseismic deformation and fault model of the 2017 Ms7. 0 Jiuzhaigou earthquake in the Northeast Bayanhar block. *Tectonophysics, 726*, 86-99. doi:

Zhao, G., Unsworth, M. J., Zhan, Y., Wang, L., Chen, X., Jones, A. G., et al. (2012). Crustal structure and rheology of the Longmenshan and Wenchuan Mw 7.9 earthquake epicentral area from magnetotelluric data. *Geology, 40*(12), 1139-1142. doi:

Zhao, J., Yuan, Z., Ren, J., Jiang, Z., Yao, Q., Zhou, Z., et al. (2022). Acceleration of Deep Slip Along the Longmenshan Fault Plane Before the 2008 M8.0 Wenchuan Earthquake. *Frontiers in Earth Science, 10*. doi: 10.3389/feart.2022.830317

Zheng, G., Wang, H., Wright, T. J., Lou, Y., Zhang, R., Zhang, W., et al. (2017). Crustal Deformation in the India-Eurasia Collision Zone From 25 Years of GPS Measurements. *Journal of Geophysical Research: Solid Earth, 122*(11), 9290-9312. doi: 10.1002/2017jb014465

Zheng, T., Ding, Z., Ning, J., Chang, L., Wang, X., Kong, F., et al. (2018). Crustal azimuthal anisotropy beneath the southeastern Tibetan Plateau and its geodynamic implications. *Journal of Geophysical Research: Solid Earth, 123*(11), 9733-9749. doi:

Zheng, Y.-F., Xiao, W.-J., & Zhao, G. (2013). Introduction to tectonics of China. *Gondwana Research, 23*(4), 1189-1206. doi: 10.1016/j.gr.2012.10.001

Zhu, S., Chen, J., & Shi, Y. (2022). Earthquake potential in the peripheral zones of the Ordos Block based on contemporary GPS strain rates and seismicity. *Tectonophysics, 824*. doi: 10.1016/j.tecto.2022.229224

Zhu, S., & Shi, Y. (2011). Estimation of GPS strain rate and its error analysis in the Chinese continent. *Journal of Asian Earth Sciences, 40*(1), 351-362. doi: 10.1016/j.jseaes.2010.06.007

[Journal of Geophysical Research: Solid Earth]

Supporting Information for

Reconciling high-resolution strain rate of continental China from GNSS data with the spherical spline interpolation

Zhengfeng Zhang[1], Huai Zhang[1,2,3] and Yaolin Shi[1]

[1]Key Laboratory of Computational Geodynamics of Chinese Academy of Sciences, College of Earth and Planetary Science, University of Chinese Academy of Sciences, Beijing 100049, China.

[2]Southern Marine Science and Engineering Guangdong Laboratory (Zhuhai), Zhuhai 519080, China

[3]Beijing Yanshan Earth Critical Zone National Research Station, University of Chinese Academy of Sciences, Beijing 101408, China

Corresponding author, E-mail: hzhang@ucas.ac.cn

Contents of this file

Figures S1 to S10

Additional Supporting Information (Files uploaded separately)

Table S1 to S4

Introduction

Supporting materials included in the file include the following:

1）Other strain rate results of rigid rotation detection with spherical spline (Figure S1-S2).
2）Longitude direction derivative of velocity ($\frac{dv_\theta}{d\varphi}, \frac{dv_\varphi}{d\varphi}$) of spherical harmonics and fitting results of spherical spline (Figure S3, S6).
3）Theoretical Strain rate of spherical harmonics detection model and fitting results of spherical spline (Figure S4 to S5, S7 to S8).
4）The rotation rate of continental China (Figure 9).
5）The strain rate of North China (Figure 10).
6）The GNSS velocity data of continental China (Table S1).
7）The data set of strain rate of continental China (table S2 to S4)

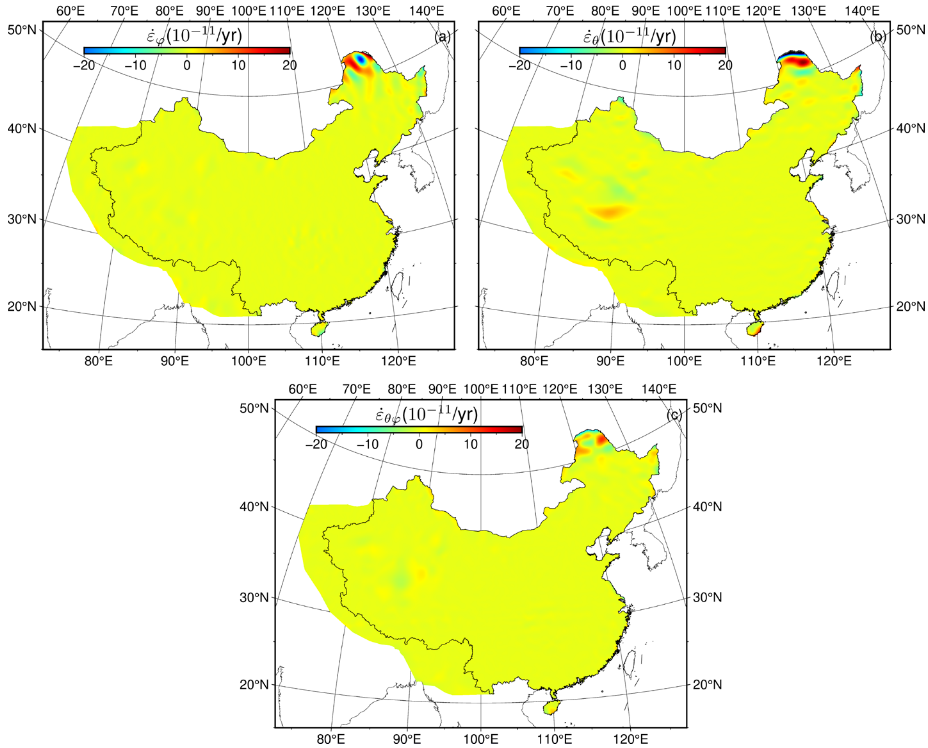

Figure S1. (a) $\dot{\boldsymbol{\varepsilon}}_{\boldsymbol{\varphi}}$ (spherical spline). (b) $\dot{\boldsymbol{\varepsilon}}_{\boldsymbol{\theta}}$ (spherical spline). (c) $\dot{\boldsymbol{\varepsilon}}_{\boldsymbol{\theta\varphi}}$ (spherical spline). The Euler polar is $\mathbf{35}°\ \boldsymbol{N}, \mathbf{105}°\ \boldsymbol{E}$.

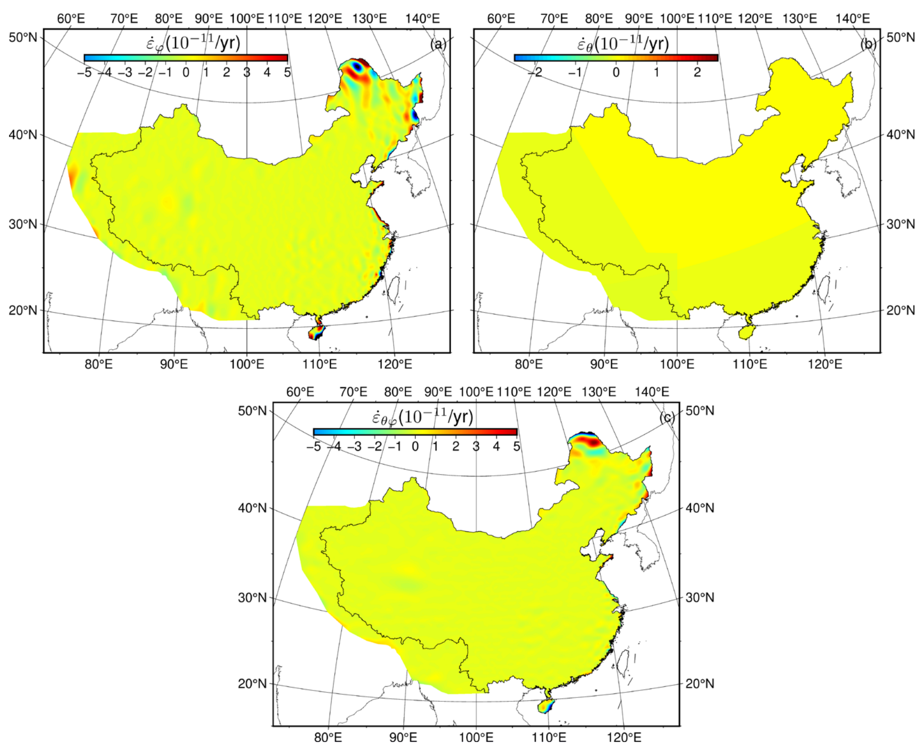

Figure S2. (a) $\dot{\boldsymbol{\varepsilon}}_{\boldsymbol{\varphi}}$ (spherical spline). (b) $\dot{\boldsymbol{\varepsilon}}_{\boldsymbol{\theta}}$ (spherical spline). (c) $\dot{\boldsymbol{\varepsilon}}_{\boldsymbol{\theta\varphi}}$ (spherical spline). The Euler polar is $\mathbf{90}°\ \boldsymbol{N}, \mathbf{105}°\ \boldsymbol{E}$.

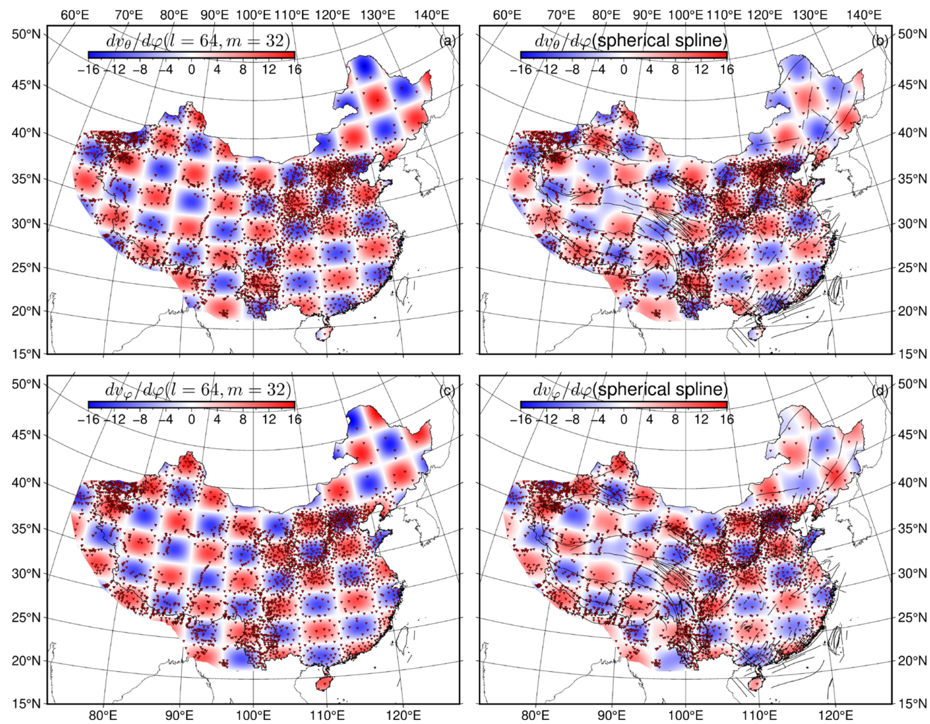

Figure S3. (a) $\frac{dv_\varphi}{d\varphi}$ calculated by spherical harmonics. (b) $\frac{dv_\varphi}{d\varphi}$ estimated by spherical spline. (c) $\frac{dv_\theta}{d\varphi}$ calculated by spherical harmonics. (d) $\frac{dv_\theta}{d\varphi}$ estimated by spherical spline.

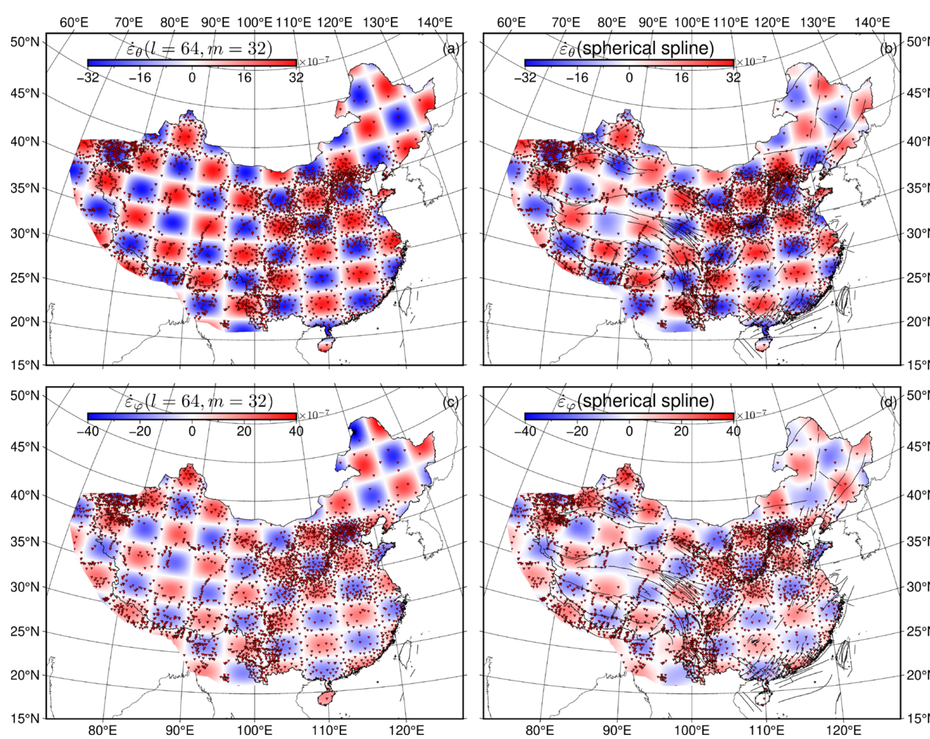

Figure S4. (a) $\dot{\varepsilon}_\theta$ calculated by spherical harmonics. (b) $\dot{\varepsilon}_\theta$ estimated by spherical spline. (c) $\dot{\varepsilon}_\varphi$calculated by spherical harmonics. (d) $\dot{\varepsilon}_\varphi$ estimated by spherical spline.

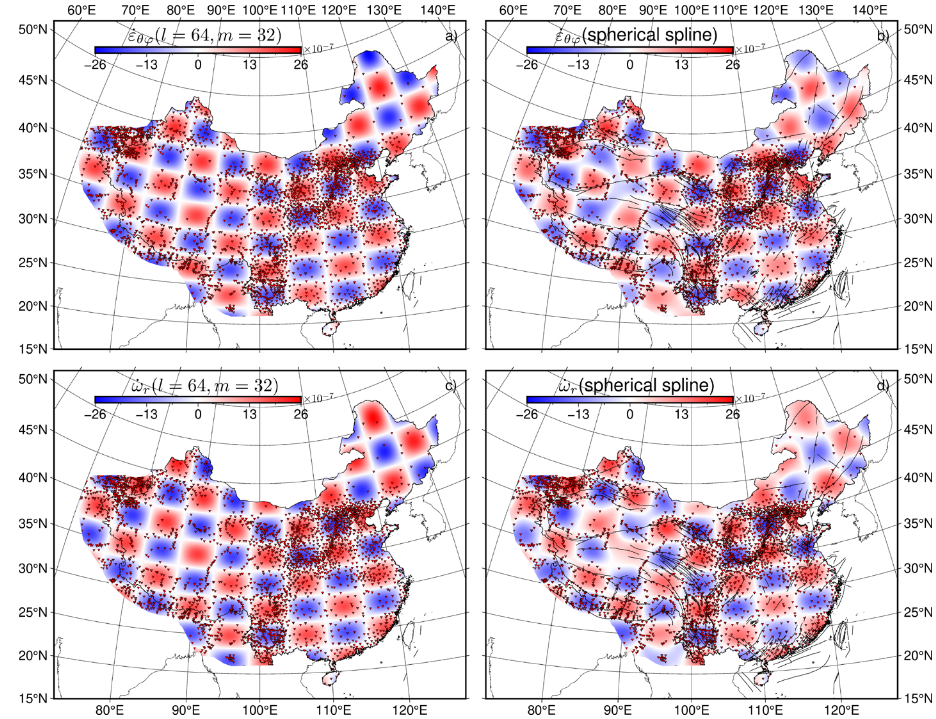

Figure S5. (a) $\dot{\varepsilon}_{\theta\varphi}$ calculated by spherical harmonics. (b) $\dot{\varepsilon}_{\theta\varphi}$ estimated by spherical spline. (c) $\dot{\omega}_r$ calculated by spherical harmonics. (d) $\dot{\omega}_r$ estimated by spherical spline.

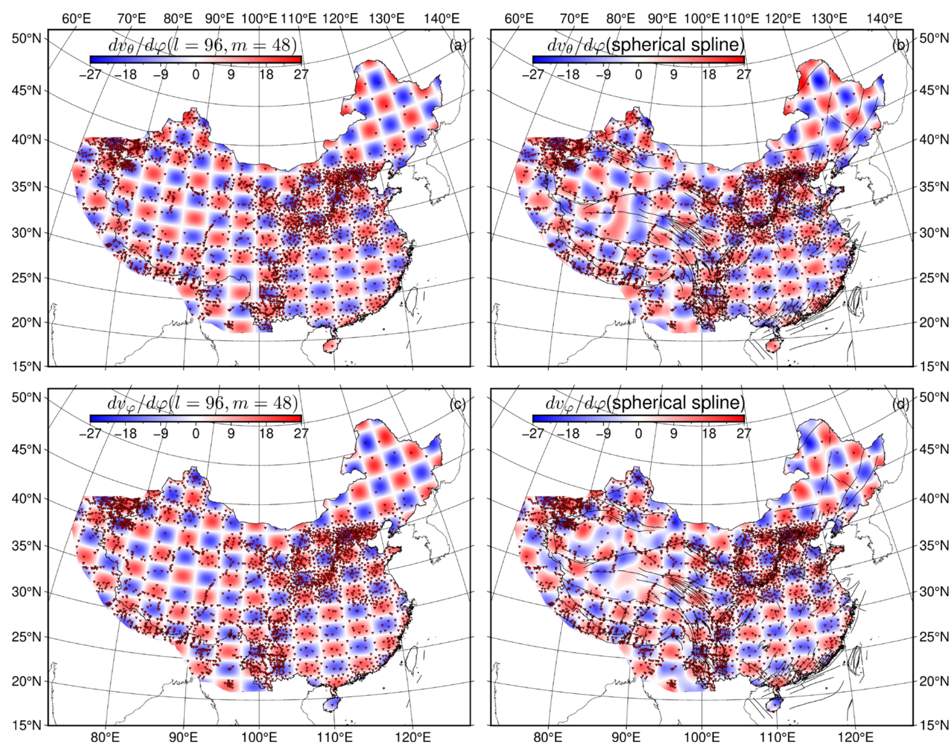

Figure S6. (a) $\frac{dv_\varphi}{d\varphi}$ calculated by spherical harmonics. (b) $\frac{dv_\varphi}{d\varphi}$ estimated by spherical spline. (c) $\frac{dv_\theta}{d\varphi}$ calculated by spherical harmonics. (d) $\frac{dv_\theta}{d\varphi}$ estimated by spherical spline.

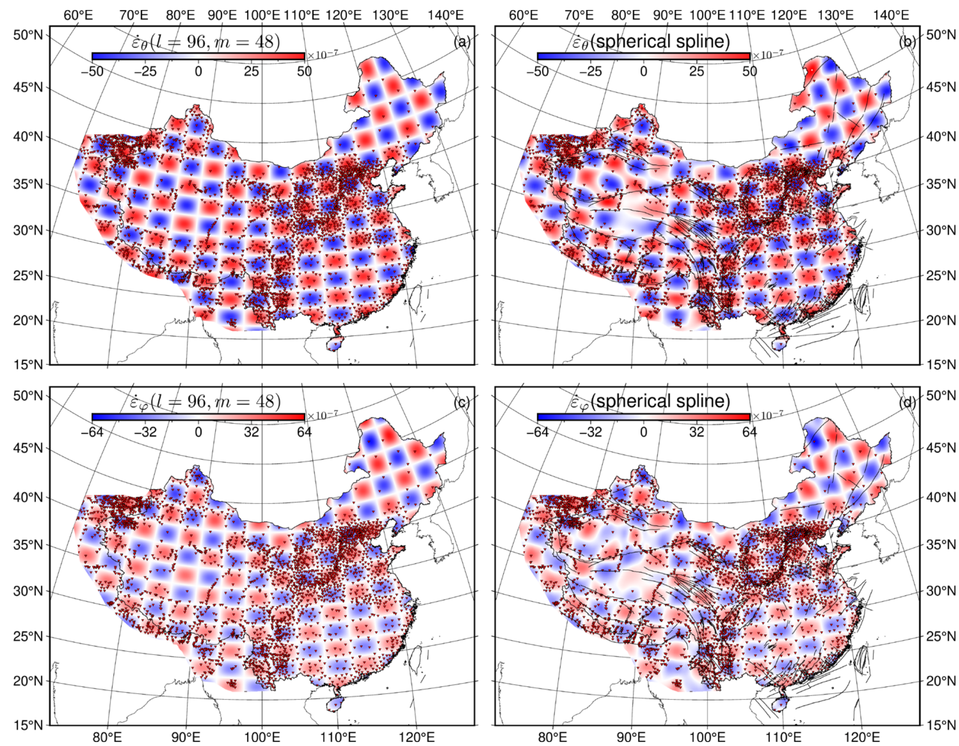

Figure S7. (a) $\dot{\varepsilon}_\theta$ calculated by spherical harmonics. (b) $\dot{\varepsilon}_\theta$ estimated by spherical spline. (c) $\dot{\varepsilon}_\varphi$ calculated by spherical harmonics. (d) $\dot{\varepsilon}_\varphi$ estimated by spherical spline.

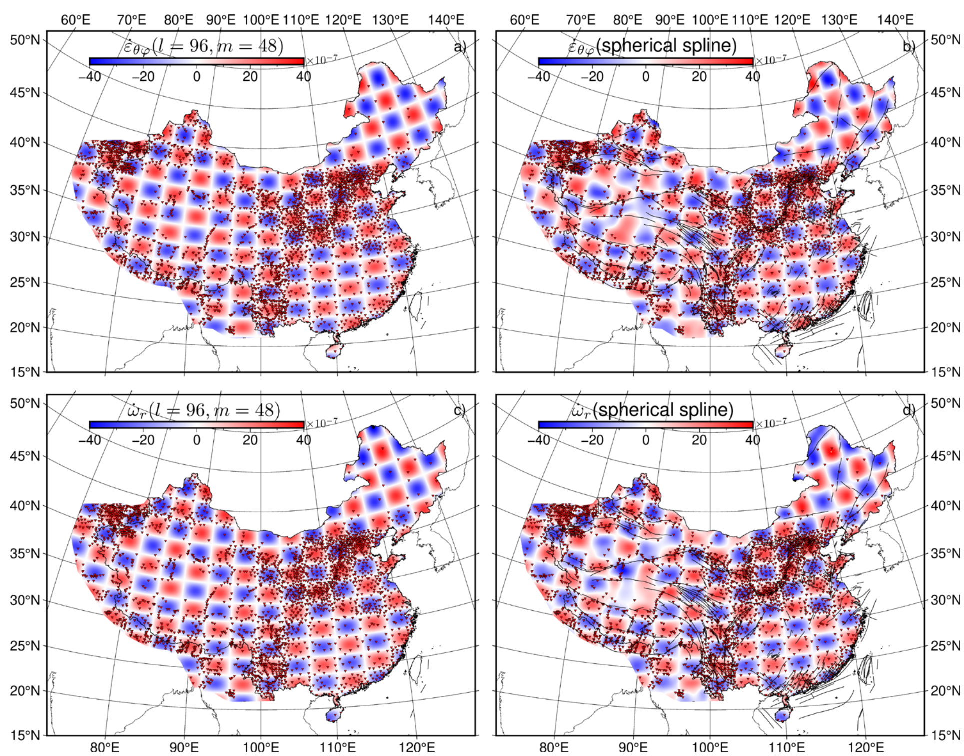

Figure S8. (a) $\dot{\varepsilon}_{\theta\varphi}$ calculated by spherical harmonics. (b) $\dot{\varepsilon}_{\theta\varphi}$ estimated by spherical spline. (c) $\dot{\omega}_r$ calculated by spherical harmonics. (d) $\dot{\omega}_r$ estimated by spherical spline.

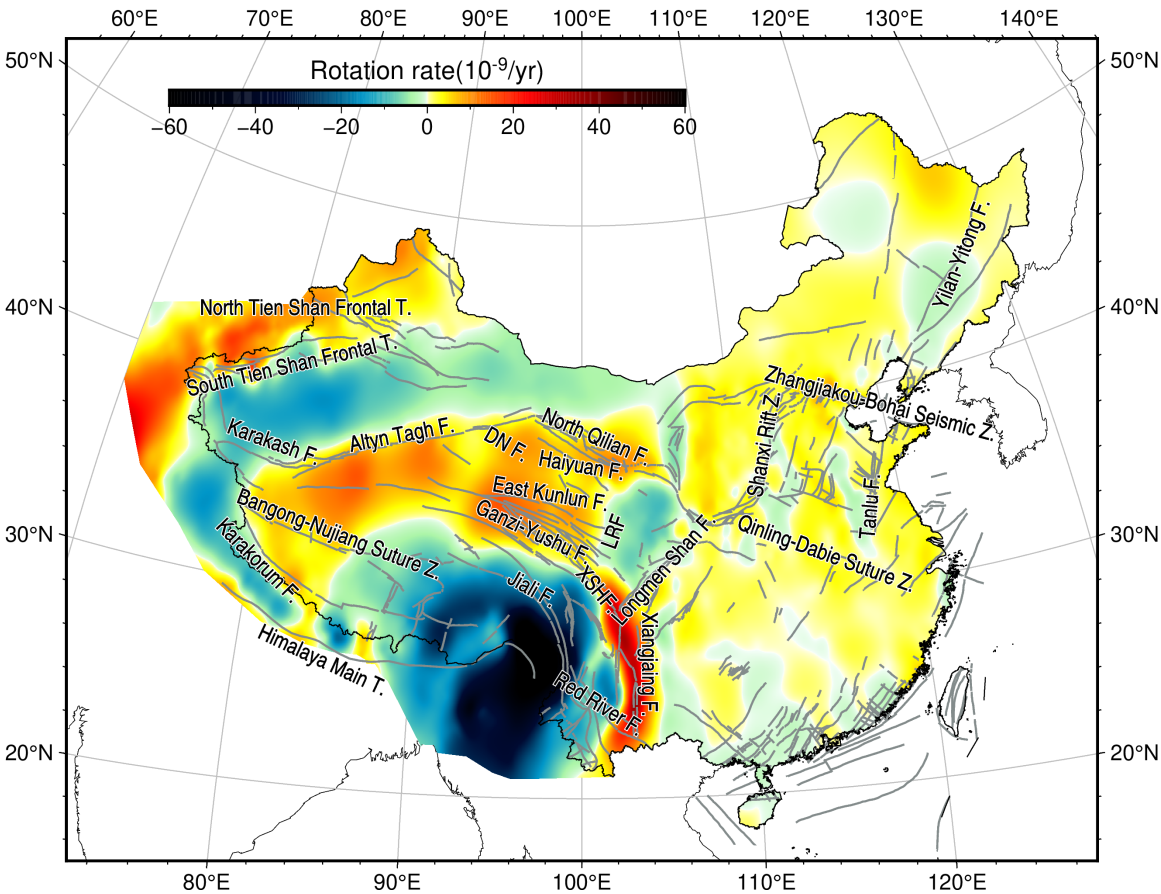

Figure S9. The rotation rate of continental China.

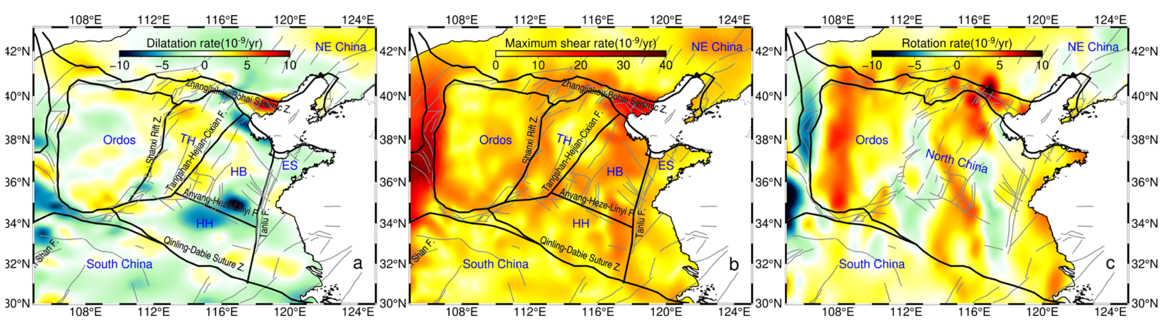

Figure S10. (a)Dilatation rate of North China. (b) maximum shear rate of North China. (c) Rotation rate of North China. The bold black lines indicate block boundaries; The thin gray lines indicate active faults; Block names: TH (Taihang Mountain), HB (Hebei), ES (East Shandong), HH (Hehuai).